Optical Micromachined Ultrasound Transducers (OMUT)– A New Approach for High Frequency Ultrasound Imaging

A Dissertation

SUBMITTED TO THE FACULTY OF GRADUATE SCHOOL OF

UNIVERSITY OF MINNESOTA

BY

Mohammad Amin Tadayon

IN PARTIAL FULFILLMENT OF THE REQUIREMENTS

FOR THE DEGREE OF

DOCTOR OF PHILOSOPHY

Shai Ashkenazi, Adviser

November 2014

Acknowledgements

First and foremost, I would like to thank my advisor, Dr. Shai Ashkenazi, for his advice and guidance throughout the years. Furthermore, I want to thank him for giving me an opportunity to study, learn, and do research on a totally new field to me. For the first couple of semesters, I am sure it was not very easy to work with somebody new in these fields. I deeply appreciate him for his patience, understanding, and great supports. I should thank him to teach me how to do and think about research.

I would like to thank all of my committee members Prof. James R. Leger, Dr. Taner Akkin, Dr. Hubert H. Lim, Dr. Mo Li, and Prof. Robert F. Wilson for taking time to review my works. I should specially thank Prof. Leger for all of his supports, guides and time for meaningful discussions. I should thank Dr. Martha-Elizabeth Baylor for her collaboration and sharing her photosensitive polymer with us. I want to also thank all of my older and current school course instructors (professors) at Iran University of Science and Technology, Sharif University of Technology, and University of Minnesota.

I am grateful to receive a Department of Biomedical Engineering first year PhD student fellowship and a University of Minnesota Doctoral Dissertation Fellowship and travel grant. I would like to thank Department of Biomedical Engineering, National Science Foundation (grant no. CMMI-1266270) and Institute of Engineering Medicine to support our research.

Thanks to all of the Photoacoustics and Ultrasound Lab members with whom I have had the privilege of crossing paths: Clay Sheaff, Ekaterina Morgounova, Qi Shao, and Vishnupriya Govindan. I specially thank Clay Sheaff to help me the first couple of semesters to teach me use of different hardware and acquisition systems in our lab and to familiarize me more with American culture. I would like to thank Chris Kaus for his help for dielectric mirror development. I should also acknowledge all of the helps and supports which I got from Minnesota Nano Center staffs and members. Among them I would like to specially thank Glenn Kuschke, Paul Kimani, Kevin Roberts, Mark Fisher, and Lage von Dissen.

I want to thank all of the people whom I shared lunch time discussions with them at 6-250 of Hasselmo Hall: Daisy Cross, Oscar Miranda-Dominguez, Xiao Zhong, Adam Black, Joseph Ippolito, Tina Yeh, Zaw Win, and Vivek Nagaraj. My special thanks to Iranian community of Minnesota for all of their supports. Particularly I want to thank my great friends, Mostafa Toloui, Taha Namazi, Mohammad Haji, Hamed Rahi, Hamid Safizadeh, Mohammad Rashidian, Mehdi Behrouzi, Vahab Zarei, and Abbas Sohrabpour for their supports, and enjoying time together during my time outside of the university.

Lastly, but not for importance, I would have never have reached this goal if there were not my parents, Zahra (Zari) and Heydar, and brothers, Arash and Ali supports, helps, and love before and after starting my PhD. During all of these years not only they gave me unconditional love, support and encouragement but they shared with me my joys and my sorrows, my successes and my defeats, as if they were theirs. There are simply no words for me to express how much I owe them.

Dedication

To my Parents, brothers and the memory of my high school president and teacher Saad (Ahmad) Hajjarian.

Abstract

Piezoelectric technology is the backbone of most medical ultrasound imaging arrays, however, in scaling the technology to sizes required for high frequency operation (> 20 MHz), it encounters substantial difficulties in fabrication and signal transduction efficiency. These limitations particularly affect the design of intravascular ultrasound (IVUS) imaging probes whose operating frequency can approach 60 MHz. Optical technology has been proposed and investigated for several decades as an alternative approach for high frequency ultrasound transducers. However, to apply this promising technology in guiding clinical operations such as in interventional cardiology, brain surgery, and laparoscopic surgery further raise in the sensitivity is required.

Here, in order to achieve the required sensitivity for an intravascular ultrasound imaging probe, we introduce design changes making use of alternative receiver mechanisms. First, we present an air cavity detector that makes use of a polymer membrane for increased mechanical deflection. We have also significantly raised the thin film detector sensitivity by improving its optical characteristics. This can be achieved by inducing a refractive index feature inside the Fabry-Perot resonator that simply creates a waveguide between the two mirrors. This approach eliminates the loss in energy due to diffraction in the cavity, and therefore the Q-factor is only limited by mirror loss and absorption. To demonstrate this optical improvements, a waveguide Fabry-Perot resonator has been fabricated consisting of two dielectric Bragg reflectors with a layer of photosensitive polymer between them. The measured finesse of the fabricated resonator was 692, and

the Q-factor was 55000. The fabrication process of this device has been modified to fabricate an ultrasonically testable waveguide Fabry-Perot resonator. By applying this method, we have achieved a noise equivalent pressure of 178 Pa over a bandwidth of 28 MHz or 0.03 $Pa/Hz^{1/2}$ which is approximately 20-fold better than a similar device without a waveguide. The finesse of the tested Fabry-Perot resonator was around 200. This result is 5 times higher than the finesse measured in the same device outside the waveguide region. In future, our developed technology can be integrated on the tip of an optical fiber bundle and applied for intravascular ultrasound imaging.

Table of Contents

List of Tables

List of Figures

Chapter 1. Introduction

1.1 Background

The application of optical imaging to turbid media such as human tissue is limited in penetration depth due to strong light absorption and scattering. In this case, ultrasound imaging is a reliable alternative when the target has different mechanical properties than its surrounding medium. This imaging modality has many applications such as pregnancy monitoring (sonography), submarine navigation systems (sonar), and structural crack detection (ultrasonic testing). In most cases, a high frequency sound pulse generated by a transmitter propagates through a medium, reflects off an object, and is detected by a receiver. The time delay between the generation of the pulse and reception of its reflection is measured, and the position of the object is estimated by multiplying this delay by the speed of sound in the medium. Typically, the applied transmitter and receiver are included in a single element, and this is referred to as a transducer. A 2D or 3D image of an object can be produced by using more than one transducer (an array of ultrasound transducers) and the application of various ultrasound imaging techniques.

The image resolution is directly proportional to the frequency of the transducer, therefore a transducer with a higher frequency can provide a higher resolution.

High-frequency ultrasound imaging is a valuable tool for ophthalmology, dermatology, and small animal research applications. Resolutions of up to 20 μm can be realized by spatially scanning single-element transducers or by using a large number of elements as an array. However, this technology has not been widely used in guiding clinical operations such as in interventional cardiology, brain surgery, and laparoscopic surgery. This is due to the major technical difficulties in forming compact ultrasound imaging arrays that can be inserted into various arteries or delivered through small bore-size tubing. The level of miniaturization (typically less than 1 mm for a probe holding tens of elements) that is required for such applications is beyond the abilities of current transducer technology. In present ultrasound systems, piezoelectric materials are utilized to convert ultrasound pulses to electrical signals in the receiving mode and vice versa in the transmitting mode. In scaling the current technology to sizes required for high frequency operation (> 20 MHz), piezoelectric transducers are difficult to fabricate and do not have adequate signal transduction efficiency. In order to overcome these problems, alternative technologies such as micro-electro-mechanical systems and optical micro-devices have been investigated for ultrasound generation and detection. The introduction of micromachining techniques in the design and fabrication of these devices has resulted in substantial improvements. However, the ultimate goal of miniaturizing probes to a size

of less than 1 mm, which is necessary for guiding coronary interventions is still beyond reach.

Table 1-1. Comparing commercial intravascular ultrasound transducers.

Feature	SVMI HD-IVUS	BSC iLab/ Atlantis	Volcano s5/ Revoltion	Lightlab/SJM/C7-XR/Dragonfly
Frequency/wavelength	40 & 60 MHz	40 MHz	45MHz	1300 nm
Energy	Ultrasound	Ultrasound	Ultrasound	NIR Light
Axial Resolution	<50µm	~150µm	~200µm	~15µm
Max Frame rate	100 fps	30 fps	30 fps	100 fps
Max. Pullback Speed	20 mm/sec	1.0 mm/sec	1mm/sec	20mm/sec
Frame Spacing	5-200µm	17µm	17µm	200µm
Elevational Resolution	~200µm	~400µm	~500µm	~40µm
Pullback Length	120mm	100mm	100mm	50mm
Tissue Penetration	>4mm	>5mm	>5mm	0.8-1.5mm
Imaging in Blood	Yes	Yes	Yes	No

High quality IVUS imaging poses highly demanding design requirements. First and foremost, the device has to be small enough to pass through narrowed coronary arteries, which typically translates to a maximal size of 1 mm. Good image resolution is also essential for precise diagnosis of pathologies, and it is widely acknowledged that a resolution higher than 0.1 mm is needed [1-5]. This can be obtained by operating at high center frequency and large bandwidth. Combining this requirement with the need for a penetration depth of up to 10 mm, sets a restriction on the maximal frequency. Typically, the range of 40 – 80 MHz is considered optimal. Finally, an adequate spatial sampling needs to be chosen in order to avoid grating lobes. This leads to a half-wavelength condition on the spacing between elements evaluated at the highest usable frequency [6]. Assuming a maximal frequency of 80 MHz, the element spacing should be approximately 10 µm. Table 1-1 compares different commercial intravascular ultrasound transducers.

The sensitivity of an ultrasound detector is characterized by its noise equivalent pressure (NEP) defined as a lowest detectable signal over usable bandwidth of the detector. The required NEP for an IVUS imaging system is a function of the transmitted acoustic pressure, acoustic attenuation, the scattering power of the imaged objects, and their distance. Typically a transmitted wave of about 1 MPa will be launched and echoes in the range of 2 to 4 orders of magnitude smaller will be detected. The required NEP of the detectors should therefore be on the order of 100 Pa to drive an acceptable signal to noise ratio without averaging. None of the current ultrasound technologies can be used to fully implement size, frequency, and sensitivity requirements.

1.2 Current Technologies

The challenge of finding the best compromise, given the known technological limitations, is currently addressed by several research laboratories and medical device developers. These approaches include improving piezoelectric technology and developing alternative technologies such as capacitive transducers and optical transducers (Figure 1.1 (a)). In a capacitive micromachined ultrasonic transducer (CMUT), applying a voltage pulse to an air-gap capacitor having an elastic top plate, results in a transient force between the plates and generates an ultrasound pulse. Ultrasound echoes are detected by sensing modulations in capacitance resulting from the displacement of the elastic membrane [7, 8]. This approach is based on the capabilities of advanced micro- and nano-fabrication techniques. Recently, a 24-element CMUT probe housed in a 9F catheter with a bandwidth of more than 8 MHz has been developed and used in forward-looking *in vivo*

applications [9]. In addition to its limited bandwidth, a significant drawback of this device is its limited ability to be mechanically steered. Because the bend radius is roughly 3 cm - considerably larger than typical bends in coronary arteries - its clinical use is limited. This is due to a stiff circuit board which is used to connect the CMUT array to the wiring system and front-end electronics.

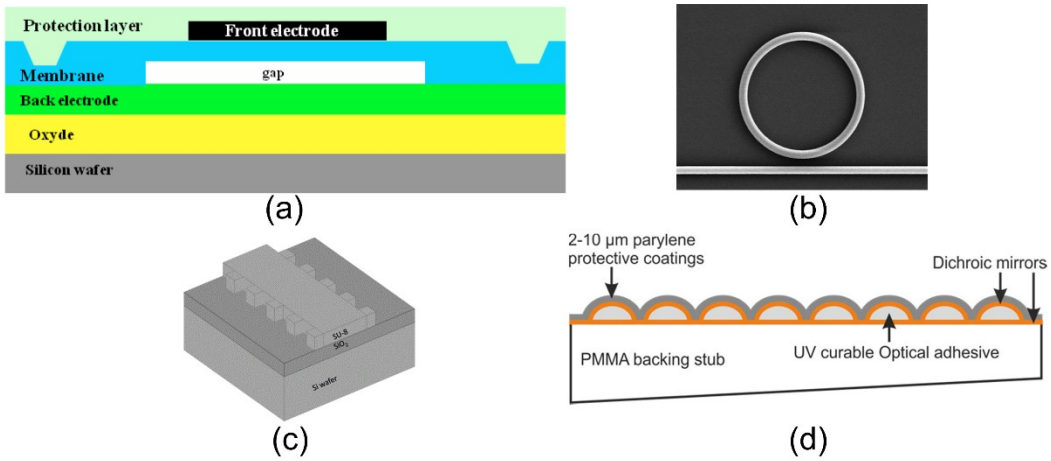

Figure 1.1. Schematic of (a) capacitive micromachined ultrasound transducer [10], (b) microring resonator [11], (c) Bragg grating waveguide reflector [12], and (d) concave cavity [13] .

Optical technology has been proposed and investigated for several decades as an alternative approach for high frequency ultrasound transducers. Optical resonators of different configurations have been designed for ultrasound detection and pulsed lasers have been used to generate ultrasound via the thermoelastic effect. An optical resonator is an arrangement of optical components that allows a beam of light to circulate in a closed path [14]. When operating close to their resonance frequency, optical resonators are extremely sensitive to optical path length variations caused by the application of pressure. Fabry–Pérot resonators made of a transparent plate with two reflecting surfaces were one of the first optical resonators [15] to be used for this purpose, either as a single element

detector on the tip of an optical fiber [16-18] or as a thin-film coating on a glass window[19, 20]. Of these devices, a noise equivalent pressure of 0.2 kPa over a bandwidth of 20 MHz ($0.04\,Pa/\sqrt{Hz}$) has been achieved [21]. Microring resonators (Figure 1.1 (b)) are another type of optical resonator which have been studied for high frequency ultrasound and photoacoustic imaging. The application of microring resonators for ultrasound detection is introduced in [22, 23]. These devices have been shown to have very high ultrasound sensitivity. A noise equivalent pressure of 88 Pa over a bandwidth of 75MHz ($0.01\,Pa/\sqrt{Hz}$) has been recently demonstrated by Ling et al. using a polymer microring ultrasound detector [24]. Another optical device which has been used for ultrasound detection is the Bragg Grating Waveguide reflector [25, 26] (Figure 1.1 (c)). Li et. al. have proposed a polymer structure having a curved top mirror (Figure 1.1 (d)) to provide a stable resonance condition [13]. Their approach has significantly improved the detection sensitivity in comparison to flat film etalon detectors

An all-optical transducer having both transmit and receive functionality can be built by adding a photoabsorptive film into an optical resonator detector [27, 28]. In order to optically generate an ultrasound pulse, a laser pulse hits a thin photo-absorptive layer. The absorption of light generates heat in the film thereby increasing the layer temperature. The temperature increase induces the generation of a pressure wave (ultrasound pulse).

1.3 Optical Micromachined Ultrasound Transducer Concept

We aim to develop Optical Micromachined Ultrasound Transducer (OMUT) technology for high-resolution ultrasound imaging probes that can be mounted on the tip of a needle or in small diameter tubing (less than 1 mm). The design relies on the generation of an ultrasound pulse using a laser pulse and detection of that pulse by application of a second light beam. As a result, all signal communications to and from the device are optical. This innovative ultrasound transducer technology surpasses the limits in miniaturization and resolution of conventional ultrasound devices. With this technology, ultrasound is generated by rapid absorption of short laser pulses in a thin film (less than 10 μm). Flexible Fabry-Perot resonators form high-sensitivity ultrasound detectors. More details about the working mechanism of OMUT are presented in the following section.

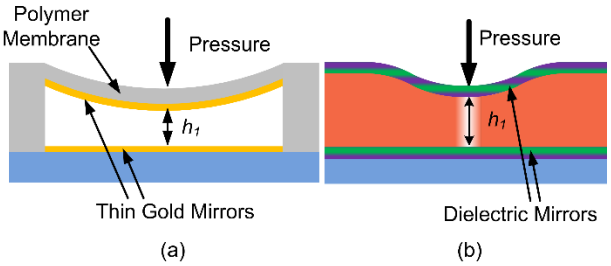

Figure 1.2 (a) air gap cavity, and (b) waveguide.

1.3.1 A basic receiver element

We developed two different technologies for the receiver element. The first ultrasound receiver design consists of two parallel mirrors (optical cavity resonator) in which the top gold mirror is deposited on a thin polymer membrane with a thickness of less than 8 μm (Figure 1.2 (a)). The diameter of the mirrors and membranes are in the range of 10 - 60 μm, and the gap between them is less than 20 μm (height of spacer).

Another technology developed based on a polymeric waveguide Fabry-Perot resonator utilizing a step-index polymer waveguide structure between two parallel dielectric mirrors [29] (Figure 1.2 (b)). The diameter of the waveguides are in the range of 10 – 50 μm, and the gap between them is about 25 μm (height of the polymer layer). The mirrors are highly reflective, but a small amount of incidental light can pass through them and create repeated reflections between the two mirrors. For both types of receivers, after the optimal wavelength is determined, a continuous wave laser beam is used to find the change in distance between the mirrors when the polymer layer is compressed by ultrasound. This change can be quantified by measuring the reflection from the first mirror.

The top membrane in the air gap and the waveguide layer in the other detector deflect under application of an ultrasound pressure wave, and the distance between the mirrors changes. This in turn modulates the amount of the reflection from the mirrors. Hence, the application of an ultrasound pulse (pressure pulse) changes the distance between the mirrors and the amplitude of this pulse can be determined by measuring the reflected light intensity. Microfabrication techniques are applied to develop the receiver with different sizes. With application of the waveguide technology, we achieved 20 times higher output signal in response to same ultrasound pulse comparing our previous devices. This improvement in ultrasound detection sensitivity which was the bottle neck for the clinical application of this technology would be a way to finally implement these devices for high resolution intravascular imaging.

1.3.2 OMUT fabrication on an optical fiber for IVUS imaging Probe

In order to optically generate an ultrasound pulse, a UV laser pulse (at a wavelength of 365 nm) hits a thin photo-absorptive layer which absorbs most of the incidental light. The absorption of light generates heat in the film thereby increasing the layer temperature. The temperature increase induces thermal expansion in the film which results in the generation of a pressure wave (ultrasound pulse). Transmitter arrays can be designed, and fabricated as a function of their thickness. The transmitter elements can be integrated with the receiver elements by adding a photo-absorptive layer underneath the receivers (Figure 1.3). Complete pulse-echo functionality of the full transmitter-receiver system can be applied for ultrasound and photoacoustic imaging.

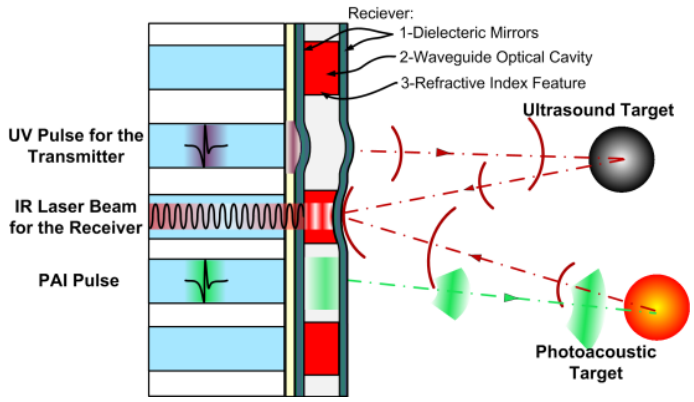

Figure 1.3. Schematic of OMUT dual modalities probe.

1.4 OMUT Dual Modality Probe Clinical Applications

The key feature of OMUTs – miniaturization – make it an ideal technology for medical applications such as real-time guidance of cardiovascular interventions, laparoscopic surgery, and deep brain electrode implantation. Another added value of this technology is the facilitation of pulse-echo ultrasound imaging and PAI in a single device.

1.4.1 Using OMUT for Interventional Heart Surgery

Treatment of totally occluded coronary arteries is considered to be one of the most difficult procedures in interventional cardiology. None of the current imaging technologies is able to provide real-time guidance for clearing the occlusion. We propose that an OMUT device of 1mm diameter coupled with a 1 mm fiber bundle could be used for 3D imaging of the occluded section and guidance of tools for plaque removal. The general idea of application of such a device is presented in Figure 1.4.

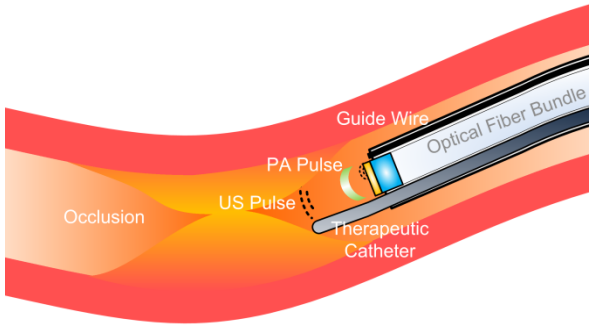

Figure 1.4 A conceptual device design based on OMUT technology. A forward-viewing 3D imaging catheter guides plaque removal from a totally occluded coronary artery.

The American College of Cardiology/American Heart Association defines chronic total occlusion (CTO) as a total occlusion with either known duration of more than 3 months or presence of bridging collaterals [30]. Percutaneous coronary intervention (PCI) is one way to treat the CTO. An alternative treatment for this purpose is coronary artery bypass grafting (CABG) in which stenotic (narrowed) arteries is bypassed by grafting vessels from elsewhere in the body. Coronary revascularization is an expensive technique and among the most frequent surgeries performed in the United States; 1204000 PCI procedures and 306000 CABG surgeries were performed in 2002 [31]. Stroupe et al. studied 445 patients with myocardial ischemia whom both PCI and CABG could be

applied for them. They randomly chose 218 patients for PCI and 227 patients for CABG [31]. According to their study, PCI had $20468 lower medical costs which is about 25% of total costs over 5 years. Furthermore, regarding this study, PCI-assigned patients had survival that was at least as good as patients assigned to CABG. However, another group found a 1.9% higher survival rate for CABG over PCI at five years, but no significant advantage at one, three, or eight years [32]. Regarding these studies, finding a way to enhance the PCI success rate can make the PCI more favorable than CABG. This can raise the survival rate and the cost efficiency of the CTO treatment.

The PCI goal is to penetrate total occlusion and place the wire in the distal vessel without causing the intimal dissection. In the current method, a guiding catheter is inserted from the femoral artery in the leg and led to the coronary artery using the x-ray visualization. X-ray cannot provide enough details about the plaque structure and sufficient information to prevent misleading of the catheter [33]. Therefore, the side looking IVUS is utilized to find the correct artery and lead back the catheter to the true lumen from the false lumen in case the catheter is misled to the false lumen [33]. Forward looking OMUT can assist the surgeon to guide the catheter to its correct place and avoid the misleading of the catheter to the false lumen which needs to use multiple stenting to fully cover the enlarged subintimal space. Furthermore, forward looking OMUT can be used for characterization and finding the total occlusion during the surgery that the side looking cannot be applied. Therefore, OMUT as a new forward looking IVUS probe can

significantly magnify the PCI survival rate which has a great economical superiority to CABG as well.

1.4.2 OMUT for Photoacoustic Imaging

The photoacoustic effect was discovered by Alexender Graham Bell in 1880 when he was looking for a mean to use it for a wireless communication. If the short light pulse is emitted to an object, part of it is absorbed and the other part is reflected or transmitted through the object. Absorbed light partially converts to heat causing expansion in the absorbed region. Expansion in the specific region of the material generates a strain/stress field. A nonequilibrium condition of the strain/stress field causes a propagation of the acoustical wave through the material until the whole material returns to its equilibrium state. The equilibrium condition is resulted from the wave transmission to another medium or dissipation of the mechanical energy. Two effective parameters to convert the temperature rise to the pressure are volume expansion coefficient and compressibility of the tissue [34]. The laser pulse duration usually is significantly shorter than thermal relaxation time which characterizes the thermal diffusion time and the stress relaxation time which characterizes the pressure propagation. Therefore, the heat conduction and stress propagation are negligible during the laser pulse and the laser pulse is called to be in thermal and stress confinement [35].

In Table 1-2, Photoacoustic imaging is compared with different biomedical imaging modalities respecting to different imaging characteristics [35]. Diffraction and diffusion are two main challenges which limit the spatial resolution and penetration depth of high

resolution optical imaging [34]. Ultrasonic imaging has a better resolution than optical imaging in the quasi-diffusive and diffusive regime because it has two to three orders of magnitude less scattering than optical imaging [34]. On the other hand, the ultrasonography can only detect changes in mechanical properties which has a less contrast in comparison with optical imaging [35]. However, the PAI can take advantage of both modalities. Its contrast is based on the optical absorption of optical excitation mode but the resolution is derived from ultrasonic resolution of detection mode [34]. The wider bandwidth and higher center frequency of the ultrasonic system can increase spatial resolution [36].

Table 1-2. Comparison between biomedical different imaging modalities [35].

Property	Optical Coherence Imaging	Diffusive Optical Imaging	Ultrasonic	Photoacoustic Imaging
Contrast	Good	Excellent	Poor for early cancer	Excellent
Imaging depth	Poor (~1mm)	Good(~50 mm)	Excellent	Good
Resolution	Excellent(~0.01mm)	Poor(~5mm)	Excellent and scalable (~.3mm)	Excellent and scalable
Speckle artifacts	Strong	None	Strong	None
Scattering coefficient	Strong (~10mm^{-1})	Strong (~10mm^{-1})	Weak (~0.03mm^{-1})	Mixed

A complete dual-modality imaging system (Figure 1.3) can be developed based on optical fibers and fast optical beam scanners. Combining ultrasound imaging and PAI provides a range of possibilities for the design of multi-modality, functional, and molecular imaging systems for higher specificity in medical diagnosis and therapy guidance. Developing OMUT technology as an all-optical, transparent ultrasound transducer will also enable a range of new tools in different fields of science and

technology due to its MRI compatibility, immunity to radio frequency interference, and potential for integrating with other imaging modalities.

1.5 Statement of Objectives

The receiver lack of sensitivity is one of the major problems of the optical ultrasound transducers to utilize for clinical applications. Here, we try to introduce different mechanisms to solve this problem. First in chapter 2, we introduce an air-cavity detector to increase the detector sensitivity by application of the polymer membrane which increases the device mechanical deflection. Since more improvement in sensitivity is required for the detector, in chapter 3 we introduce a waveguide Fabry-Perot resonator which significantly improves the optical characteristics of the current thin film technology. In chapter 4, we design and fabricate the waveguide Fabry-Perot resonator which can be applied for ultrasound detection. This device shows a promising results. Finally in chapter 5, different mechanisms to improve the waveguide Fabry-Perot resonator ultrasound detector performance and future direction for implication of such a device for all optical ultrasound transducer is presented.

Chapter 2. Air gap Fabry-Perot Ultrasound Detector

Taking a different approach, we introduce here a new type of polymer ultrasound detector for high frequency ultrasound detection using a Fabry–Pérot resonator consisting of an air-gap between two mirrors. The top mirror is deposited on a top polymer membrane which deflects under pressure. The bottom mirror is deposited on a glass substrate which also supports the polymer side walls of the air-cavity. This design allows optimizing the mechanical and optical properties of the device independently.

In this chapter, we first describe the device's design and principles of operation. The optical and mechanical characteristics of the device are then investigated, and a mechanical model is introduced, which takes into account the additive mass and damping due to water loading. The model is used to predict the sensitivity and frequency response of the design. We will then describe the methods we have used to fabricate the device. A modified SU-8 bonding technique has been specifically developed to allow the fabrication of smooth and wrinkle-free structures by curing the front mirror covered with

SU-8 before bonding. This results in a high quality optical resonance and high detection sensitivity. This modification is general enough to be applied in the fabrication of a wider class of devices such as microfluidic devices and opto-mechanical actuators and sensors. Next, we present the testing and characterization of the device. The experimental results are compared with the theoretical calculations. Finally, we discuss the plans to improve the quality of the optical resonance cavity for higher ultrasound sensitivity.

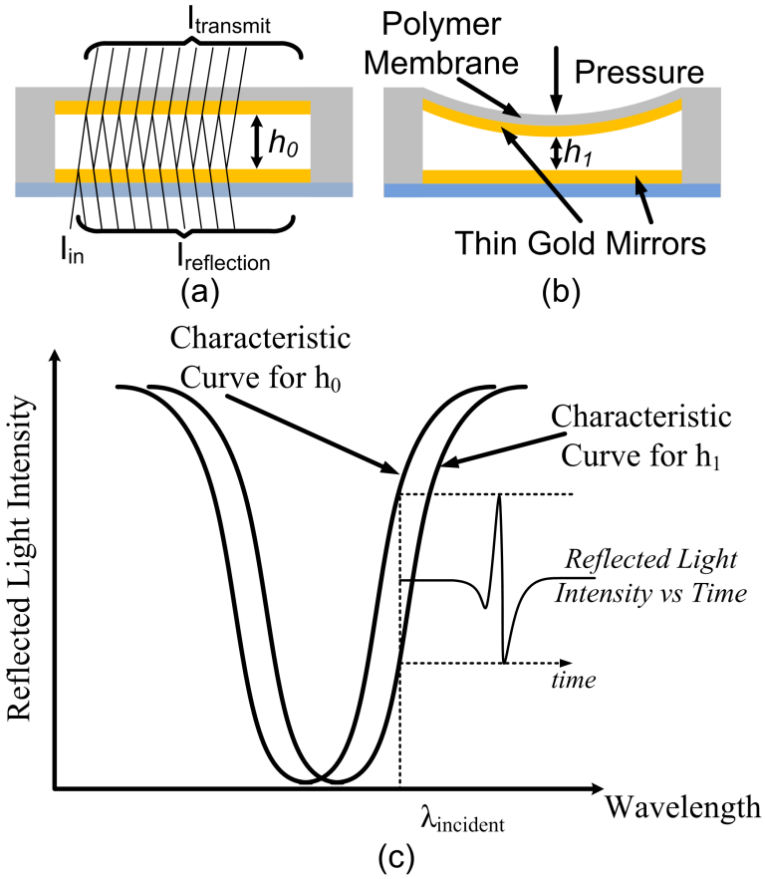

Figure 2.1. (a) optics of the cavity detector, (b) mechanics of cavity detector, and (c) working mechanism of the cavity detector.

2.1 Device Principles

The new device design consists of two parallel mirrors in which the top gold mirror is deposited on a thin polymer membrane (Figure 2.1 (a)). A laser beam with narrow linewidth is used to probe the distance between the mirrors. The characteristic curve of an optical cavity (reflected light intensity versus wavelength) varies due to variation of the gap between the mirrors. The top membrane deflects under application of pressure, and the distance between the mirrors changes (Figure 2.1 (b)). Consequently, as it can be seen in Figure 2.1 (c), if the wavelength of coupled light is locked to a specific wavelength, the reflected light intensity changes under the variation of the distance between the mirrors. Therefore, changes in the cavity gap due to an applied acoustic pressure modulate the reflected light intensity.

2.1.1 Optical Cavity Resonator

The ratio of the reflected light intensity (I^r) to the incident light intensity can be related to optical cavity parameters using,

$$\frac{I^r}{I^i} = \frac{4}{\pi^2}\mathcal{F}^2 \sin^2\frac{\delta}{2} \Big/ \left(1 + 4/\pi^2\mathcal{F}^2 \sin^2\frac{\delta}{2}\right) \qquad \text{Eq. 2-1}$$

where $\mathcal{F}$ is the finesse and δ is the phase difference due to single back-and-forth propagation of light between the mirrors [39]. The finesse is related to the reflectivity of mirrors (R) by, $\mathcal{F}$ $/(1-\mathrm{R})$ .The phase difference is $\delta = 4\pi \mathrm{nh}\cos\theta/\lambda$ where λ, n, θ, and h is the wavelength in vacuum, the refractive index of the material between the mirrors, the angle of the traveling wave between two mirrors, and the cavity length,

respectively. The optical sensitivity of the device is defined as the amount of change in I^r / I^i per change in *h*. This can be determined by taking the derivative of the Eq.2-1 with respect to *h*, yielding

$$\frac{d(I^r/I^i)}{dh} = \frac{8}{\pi\lambda} n\mathcal{F}^2 \cos\theta \ \sin\frac{\pi}{\mathcal{F}} \Big/ \left(1 + \frac{4\mathcal{F}^2}{\pi^2 \sin^2(\pi/2\mathcal{F})}\right)^2 \qquad \text{Eq. 2-2}$$

In this equation, the derivative is calculated at the half maximum which is offset by $2\pi / \mathcal{F}$ radians from the peak location. For large $\mathcal{F}$, the right hand side of Eq. 2-2 is simplified to $2n\cos\theta\mathcal{F}$. The main source of noise in our system is the electronic thermal noise of the photodetector module (see the experimental results). Therefore, the increase in sensitivity of the device directly increases the signal to noise ratio as well.

The characteristic curve of the cavity can be found experimentally by recording the reflected or transmitted power for different wavelengths. From the resonance profile, the finesse can be calculated by dividing the distance between two peaks (free spectral range) in the characteristic curve and the full width at half maximum of each peak. The optical sensitivity of the device can be calculated by substituting the experimental value of $\mathcal{F}$ into Eq. 2-2. The result can be used to verify the experimental value for the mechanical sensitivity.

2.1.2 Mechanics of the Front Membrane

Here we consider the top membrane as a **mechanical** resonator and calculate its properties. We follow the conventional treatment of flexural oscillation of a clamped membrane reducing its 2-d dynamics to a single damped harmonic oscillator equivalent.

The two major mechanical design features of the cavity detector are the first mechanical resonance frequency and the deformation of the top membrane. These design features depend on the thickness, size and material properties of the membrane. An ultrasonic detector which has a higher first resonance frequency and larger deformability can operate in larger bandwidth with higher sensitivity. There is a tradeoff between high resonance frequency and high sensitivity. Reducing the top membrane thickness decreases the bandwidth while it increases the sensitivity. One of the advantages of the cavity detector over the solid etalon design is that the mechanical properties of the device are independent of the distance between the mirrors. Therefore, this distance can be optimized for high quality optical resonance.

In order to use the device for high quality imaging, the following design parameters should be considered. The distance between two neighboring elements of an array should be less than half of the operating wavelength to eliminate grating lobes in the directivity profile. In practice, however, element spacing of up to one lambda is considered sufficient because of the limited directivity of a finite size element. In requiring a maximal frequency of 30 MHz, for example, the sensor size should be less than 50 μm, and the interelement spacing should be less than 50 μm. Assuming that the desirable bandwidth is 30 MHz, the first resonance frequency should be close to 30 MHz (or just higher). We have modeled our device as a clamped circular plate which has a resonance frequency $f_n = {10.21}/{2\pi}\sqrt{D/\rho h_p a^4}$ [40]. The displacement of the membrane center (W_{center}) under uniformly-distributed static pressure (p) is $W_{center0} = pa^4/64D$ [41] where,

E, μ, ρ, and h_p are the modulus of elasticity, Poisson's ratio, density, thickness, and radius, respectively, and $D=Eh_p^3/12\left(1-\mu^2\right)$. The front loading due to water has two major effects on the vibration of the system. First, it lowers the frequency on account of increased inertia. Secondly, damping is induced by the energy carried off from the surface in the form of sound waves [42, 43].

Regarding the additive mass of water to the membrane, Lamb has applied an analytical approach by introducing a term $\beta = 0.6689\rho_{water}a/(\rho h_p)$ for frequency correction [40]. The resonance frequency of the system in the water can be calculated using $f_{water} = \sqrt{1+\beta}^{-1} f_n$ [41]. The other parameter which can affect the bandwidth of the system is the damping ratio. Following the same approach as in [42], the damping ratio of the membrane in the cavity detector due to the solid-fluid interaction can be calculated using $\zeta = c/4\pi f h_p$, where c is the speed of sound in water and f is the excitation frequency. Therefore, the damping is a frequency-dependent parameter. The center displacement at varying frequencies $W_{center}(r)$ can be related to the static center displacement $W_{center0}$ by using a simple harmonic oscillator model,

$$W_{center}(r) = ((1-r^2)^2 + (2\zeta_{res})^2)^{-1/2} W_{center0} \qquad \text{Eq. 2-3}$$

where r is the frequency ratio (f/f_n) and ζ_{res} is the membrane damping-ratio at its resonance frequency. Furthermore, the bandwidth of the system is dependent on the damping-ratio. The mechanical sensitivity can be calculated by dividing W_{center} by the

acoustic pressure. Using Eq. 2-3, the -3 dB bandwidth of the system around the center frequency (considering the frequency dependency of the damping ratio) for the damping-ratios of 0.4 and 2.0 are approximately $0.5f_c$ and $1.85f_c$, respectively (Figure 2.2 (a)). Similar calculations are applied to the case of a solid polymer etalon in order to compare its sensitivity to that of an air-cavity sensor. The typical damping-ratio of a solid etalon, calculated from the damping equation, is 0.4 at its center frequency.

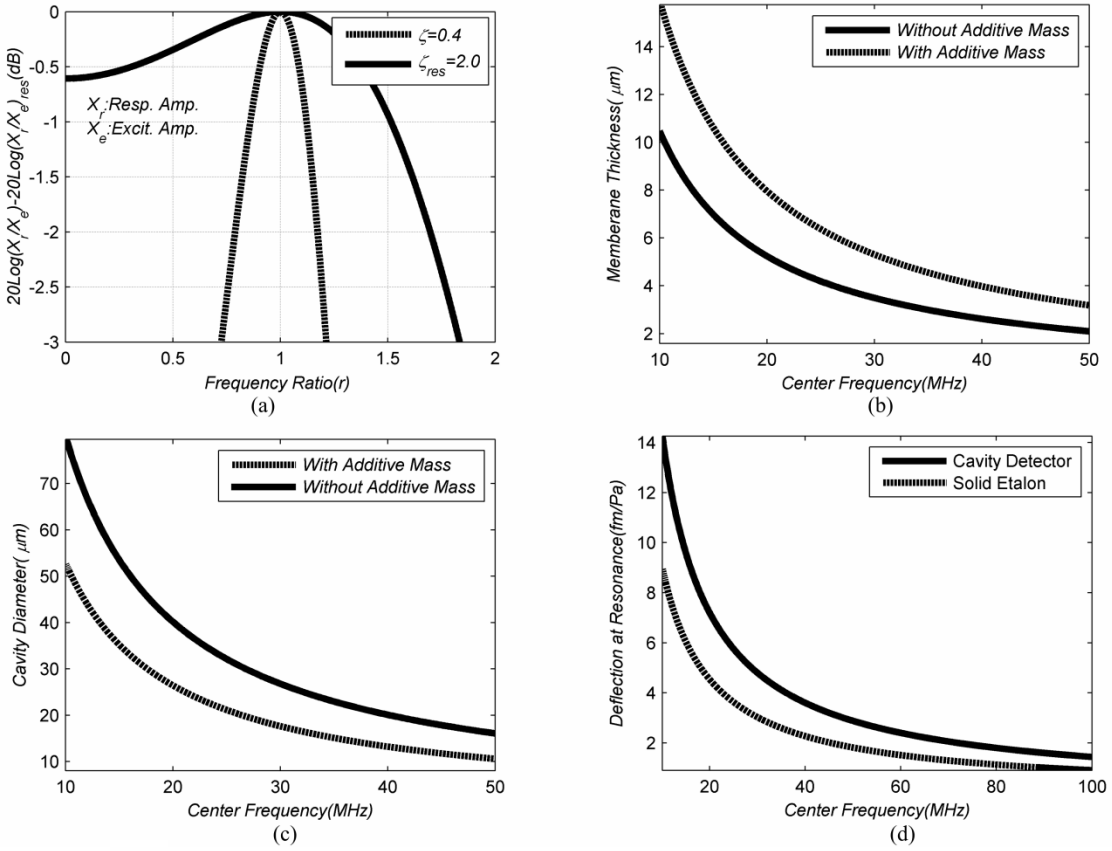

Figure 2.2. (a) The membrane thickness for different cavity center frequency (*BW (Bandwidth) = 1.5f_c*), (b) the membrane diameter for different cavity center frequency ($BW_{Cavity}=1.5f_c$) (c) transfer function of two different $\zeta_{@fc}$ (for our system which is a frequency dependent damping system) (d) the deflection for different center frequency ($BW_{Cavity}=1.5f_c$ and $BW_{Solid}=0.5f_c$).

The membrane thickness and diameter for different center frequencies are presented in Figure 2.2 (b) and (c). In these figures, the membrane specifications are presented with

and without considering the additive mass from water. The thickness of the membrane is defined for a damping-ratio of around 1.0 (bandwidth of $1.5f_c$). With a proper design, the mechanical sensitivity of the cavity detector can be 60% higher than that of a solid etalon (Figure 2.2 (d)). To have a cavity detector with a bandwidth of 45 MHz (center frequency at 30 MHz), the membrane should be 18 μm in diameter and 4 μm in thickness.

2.2 Fabrication

Figure 2.3 summarizes the fabrication process of the cavity detector. The process starts with deposition and patterning of a 180 nm chromium layer on a 4" Borofloat wafer (step 1). This chromium film is used as a mask for the patterning of the gold layer and later preventing the exposure of bonding areas to UV light. A thin film (3 μm) of SU-8 2002 is then spun and exposed to UV light (step 2). This layer will function as a protective layer for the gold mirror during the release of the top membrane from the Borofloat wafer, and it will increase the mechanical stiffness of the top membrane. A trilayer of 3 nm titanium, 30 nm gold, and 3 nm titanium is sputtered on the SU-8 layer and patterned (step 3). The gold layer forms the cavity's top mirror and the titanium layer is an adhesive layer between the gold and SU-8 layers. The front mirror is patterned using the chromium film as a mask and an image reversal technique. Then, a 5 μm layer of SU-8 2005 is spun and exposed to UV from the back side (step 5). The SU-8 in front of the mirrors is exposed to avoid wrinkling in the optical cavity during the bonding process. Wrinkles can tremendously decrease finesse of the optical cavity thereby degrading the ultrasound

sensitivity of the device. The unexposed portion is used for bonding the two wafers and encapsulation of the optical cavity to prevent water leakage which can drastically degrade the optical and mechanical characteristics of the device.

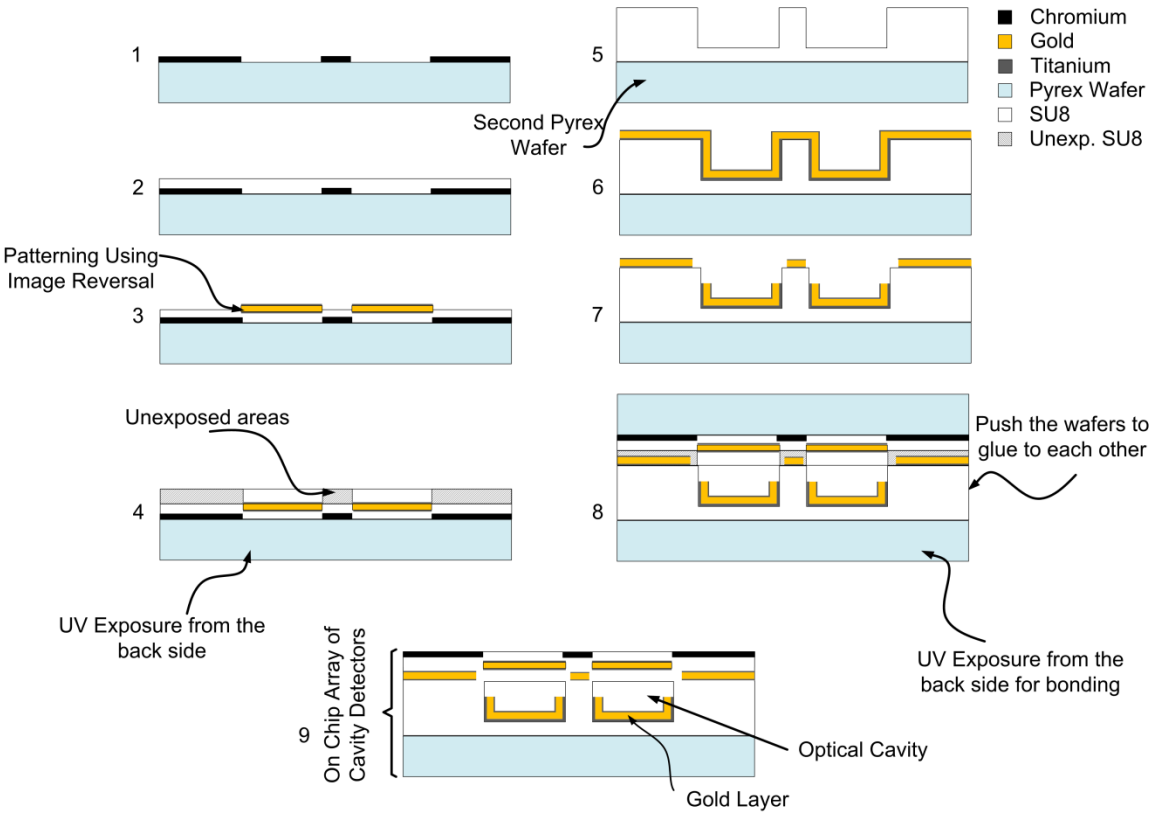

Figure 2.3. The steps to fabricate the cavity detector: 1. Deposition and patterning of chromium film. 2. Spincoating of SU-8 2005 (part of membrane and protective layer). 3. Deposition and patterning of the mirrors. 4. Spinncoating the bonding layer and exposure of the front mirror areas. 5. Fabrication of the main structure on the second wafer. 6. Deposition of the second mirror. 7. Patterning of the gold. 8. Bonding of the top and bottom wafer. 9. Releasing the membrane and removing of the top Pyrex wafer.

The fabrication of the second wafer which has the bottom optical mirrors and spacer between the two mirrors is performed by first spin-coating 13 μm of SU-8 2010 on the wafer. This layer is used to provide better adhesion between the bottom structure and the Borofloat wafer. The spacer between the two mirrors is fabricated by patterning a 21 μm layer of SU-8 2010 (step 6). Next, 3 nm titanium, 30 nm gold, and 3 nm titanium is

sputtered on the SU-8 layer. Because gold is opaque to visible light, this layer should be patterned for alignment of the first and second wafers during bonding. This can also be done by simply spincoating and developing S1813 photoresist and etching of the titanium and the gold layers (step 7).

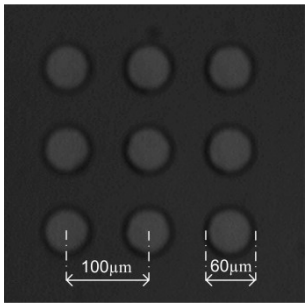

Figure 2.4. An optical picture of a two-dimensional array element from the top. The diameter of each element is 60 μm and the distance between two elements is 100 μm.

In the next step the two wafers are aligned and pressed together using the Karl Suss MJB-3 mask aligner. Using a heat gun, the temperature of the wafers is increased and kept between 80℃ to 90℃ (the optimal temperature to obtain the highest SU-8 bonding strength [44]) before and during UV exposure of the wafers from the back side of the second wafer (step 8). To have a better bond, step 4 was done just before bonding. Finally, the top wafer can be removed by covering the bottom wafer (in order to avoid etching) and soaking the wafer in the HF solvent (step 9). Both chemical compatibility and biocompatibility [45, 46] make SU-8 a material of choice for BioMEMS devices and was therefore included in the device design. The chemical and adhesion properties of SU-8 allow sealing of the air cavity against water penetration. The device was tested by immersing it in water for 24 hours, and no changes in optical or mechanical properties were found. The front view of the fabricated device is presented in Figure 2.4.

The conventional SU-8 bonding method is introduced in [47]. We have applied a simple modification to this procedure by adding UV exposure of the nonbonding area of the SU-8 bonding layer (in front of the top mirror) in order to fabricate a clean and flat surface on the bonding side. This is necessary for fabrication of high quality polymer optical cavities. Wang et al. [48] have investigated the profile of the bonding layer with respect to different applied pressures during standard SU-8 bonding. This modified SU-8 bonding procedure might also be beneficial to the fabrication of other types of devices such as micro/nanochannels [49] or any other devices which require completely transparent surfaces on top and bottom sides.

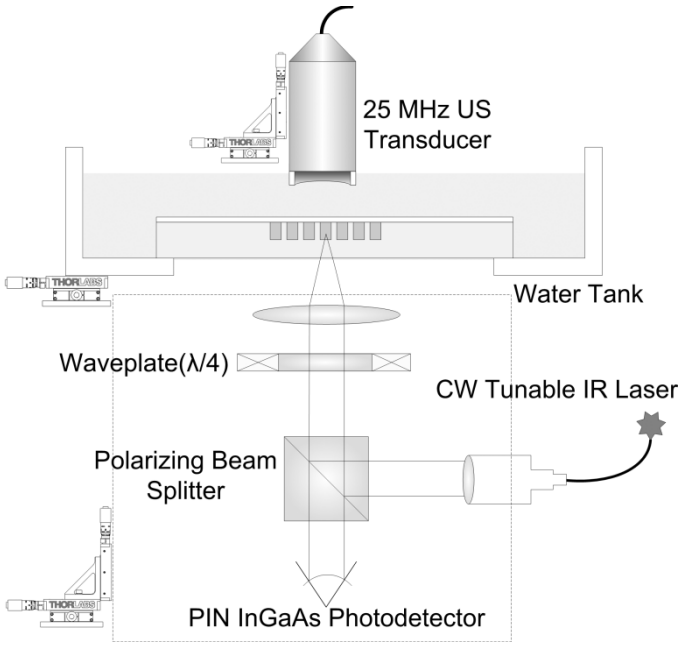

Figure 2.5. The experimental set-up which is used to find the optical and ultrasound characteristics of the device.

2.3 Experimental Results

In order to test a cavity with 60 μm diameter and a membrane thickness of 8 μm, the experimental set-up shown in Figure 2.5 has been used. The wafer is attached to a tank and immersed in water. Light from an infrared laser source is coupled to the cavity using a collimator, polarized beam splitter, λ/4 waveplate, and a lens. Linearly polarized light from a continuous near infrared (NIR) tunable laser source (8168F, Agilent HP) is transmitted to the collimator through a polarization-maintaining single mode fiber with mode field diameter of 10.5 μm. The linearly polarized collimated beam is reflected by 90° by the polarizing beam splitter. A quarter waveplate is used to change the linear polarization to circular polarization. The circularly polarized light is coupled to the cavity using a lens. Before filling the tank with water, an IR camera (1/2" CCD, Cat#56-567, Edmund Optics) is used to visualize the cavity from the top in order to align and couple the probing beam to a specific cavity element in the wafer that typically holds a large number of elements of different sizes and shapes. During the coupling process, the lens is kept off-focal to see the cavity and find its center using the IR camera. Afterward, the beam is focused to the center of the cavity to test the device.

With our arrangement of the lens and collimator, the spot size of the focused beam is approximately 36 μm. The polarization of the light changes handedness upon reflection, resulting in a perpendicular linear polarization at the beamsplitter. The beam passes through the beamsplitter and is detected by a fast-response photodetector or a power meter. To find the resonance wavelength of the optical cavity, the NIR wavelength is

scanned from 1510 nm to 1640 nm. The relative reflected light intensity is recorded using an optical power meter (PM100 optical power meter with S122B Germanium Sensor, Thorlabs) and the results are presented in Figure 2.6. The finesse of the optical cavity is between 13 and 23.

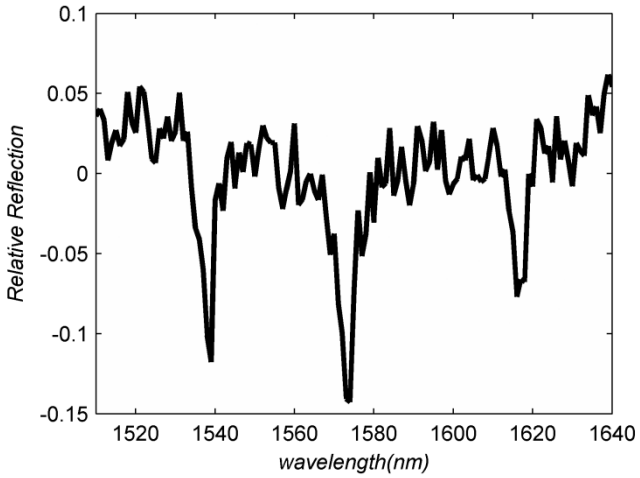

Figure 2.6. The variation of reflected light intensity versus the wavelength for 60 μm tested device.

After finding the optical resonance, the laser is tuned to a wavelength corresponding to the region of highest slope on the resonance curve. The optical power meter is replaced with a PIN InGaAs amplified photodetector (818-BB-30A, Newport) which has a short response time for high frequency optical signal recording. The IR-camera is replaced with a focused ultrasound transducer (25 MHz, f = 1", active area = 0.5", V324, Panametrics-NDT) and the tank is filled with water. The ultrasound transducer is adjusted so that the cavity is positioned at its focal point.

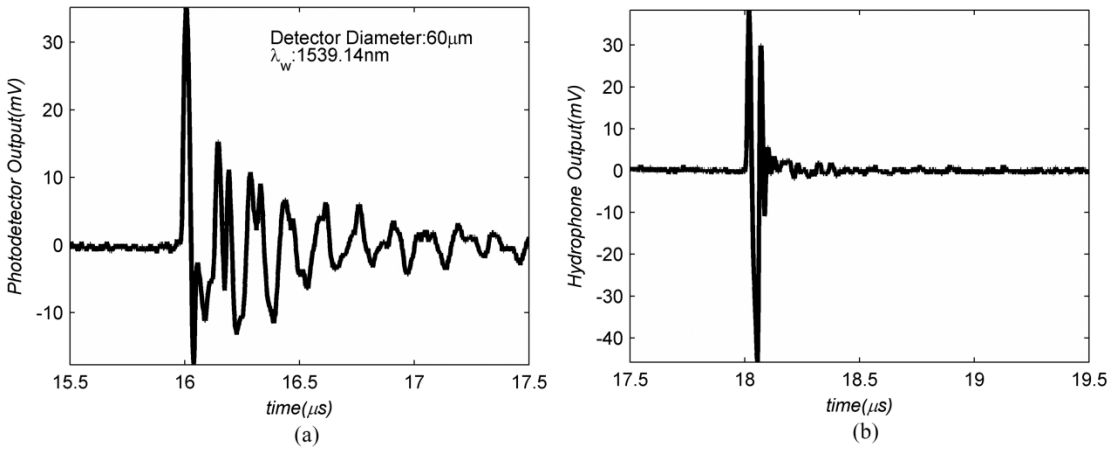

Figure 2.7. (a) The variation of reflected light intensity from the cavity detector in response to the ultrasound pulse. (b) The ultrasound pulse recorded by calibrated hydrophone.

The photodector signal is presented in Figure 2.7(a). The generated pulse from the ultrasound transducer was also recorded using a calibrated hydrophone with 60 MHz bandwidth (model HGL-0085, ONDA) and the signal is presented in Figure 2.7(b). Various sources contribute to noise in our system. Fluctuation in the intensity and phase of the laser are induced by the laser source. However, these noise sources are negligible because they have a narrow bandwidth (100 kHz) and because of the high signal-to-source spontaneous emission ratio (45 dB/nm) of the applied laser source. Shot noise, Johnson noise, and the built-in noise of the amplified photodetector are the primary sources found in the optical signal [50]. Considering all noise mechanisms of the photodetector and its built-in amplifier, the noise equivalent power of the detector is 30 pW/$\sqrt{Hz}$, that is the dominant noise source in our system. This value is specified for dark conditions, therefore the true noise is even higher because of shot noise. The other source of noise in the system is the osiloscope quantization noise which can be neglected in comparison to the photodetector-built-in amplifier noise. The noise equivalent pressure

(NEP) is defined as the acoustic pressure which provides a signal-to-noise ratio of 1. Based on the hydrophone calibration, the NEP of the device at a bandwidth of 28 MHz was calculated to be 9.25 kPa or $1.34 Pa/\sqrt{Hz}$. The noise level used in estimating the NEP was calculated as the mean square root of the noise signal (extracted before main signal arrival time at 15 μs) after lowpass filtering at 28 MHz.

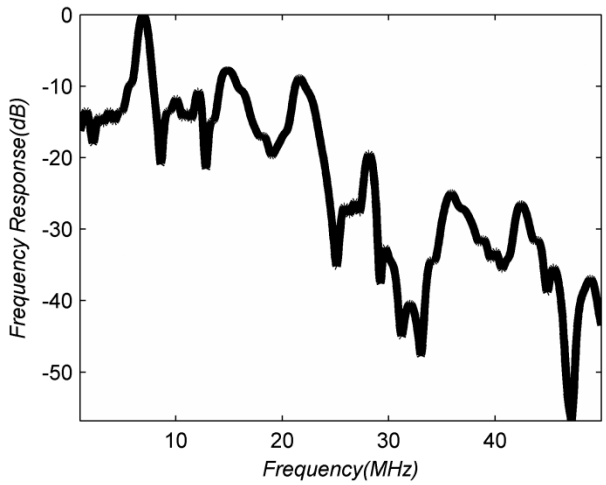

Figure 2.8. The frequency spectrum of the cavity detector reflected light intensity and calibrated hydrophone in response to the ultrasound pulse.

The response of the device (Figure 2.7 (a)) clearly shows an initial oscillation that is of high-amplitude with short-period, followed by a series of lower frequency oscillations. The former can be attributed to the direct arrival of a pressure pulse from the transducer. The subsequent oscillations are likely due to the internal acoustic reflections in the Pyrex substrate. They can also be due to mode-conversion and lateral oscillations of shear waves. The frequency spectrum of the recorded signal from the photodetector is presented in Figure 2.8. The oscillations following the main peak in the received signal is due to the back reflection from the bottom side of 400 μm Borofloat wafer (reflection

traveling time = 142 ns, corresponding frequency = 7 MHz). Therefore we conclude that the 7 MHz peak and its harmonics up to 42 MHz are due to the reflection from the bottom of the Borofloat wafer . There is an additional reflection (small peak) from the top surface of the Borofloat wafer which is 25 μm away from the top membrane (reflection traveling time = 27 ns, corresponding frequency = 37 MHz).

Since the optical properties of the device are known, the mechanical deflection (sensitivity) of the membrane can be calculated from the measured signal. This calculation facilitates the comparison of the experimental results with the prediction of the mechanical model that was presented earlier. This helps in calculating the membrane mechanical parameters for future designs. In order to estimate the mechanical sensitivity of the device (the membrane deflection per unit pressure), the percentage of change in the reflective light intensity (I^r) due to an applied pressure (p) should be calculated using the recorded signal. Furthermore, the percentage of the reflected light variation due to the change in the distance between the two mirrors (h) should be found utilizing the information from the optical characteristic curve (Figure 2.6). The reflected light intensity variation due to the change in pressure is,

$$\frac{d(I^r/I^i)}{dp} = \frac{dV/dp}{dV/d(I^iA)}\frac{1}{I^iA} \qquad \text{Eq. 2-4}$$

where, I^i , V, and A are the incident power intensity, photodetector voltage output, and area of the cavity, respectively. By measuring the photodetector readout (35 mV) under the application of a known acoustic pressure (841 kPa; recorded by the hydrophone),

dV/dp is about $4.18\times10^{-8} V/Pa$. $dV/d\left(I^i A\right)$ is the photodetector responsivity which is about 1058 V/W at 1550 nm for the photodetector used in the measurements. $I^i A$ is the coupled light power which is 477 μW. The amount of incident light is higher than this but only about 12% of it is coupled to the optical cavity. Therefore, $d\left(I^r/I^i\right)/dp$ is 23×10^{-2} MPa^{-1}. The variation of reflected light intensity is related to the variation of distance between two mirrors using Eq.(2). From Figure 2.6, it can be seen that the slope of the right side of the dip is 2.5 times sharper than the left side. Therefore, for calculation of the relation between the I^r/I^i and h, the finesse is considered 23 instead of 13. $d\left(I^r/I^i\right)/dh$ is then determined to be $3.0\times10^{-5} 1/pm$. Now, the mechanical sensitivity can easily be calculated using,

$$\frac{dh}{dp} = \frac{d(I^r/I^i)}{dp} \Big/ \frac{d(I^r/I^i)}{dh} \qquad \text{Eq. 2-5}$$

which is 7.8 fm/Pa. This is close to our mechanical calculation considering both water additive mass and damping (β = 2.1, f_n = 4.5 MHz, f = 11.7 MHz, r = 2.6) which is 9.7 fm/Pa. The device was tested for several hours and the results were repeatable.

2.4 Optical Cavity Modeling Using Ray Optics

The wall effect becomes more significant when the beam spot size becomes in the order of the cavity width and the cavities with higher finesse (will be discussed in the next chapter). In these cases, when photons reflects back and forth between mirrors, they can hit the side walls. Therefore, the side walls reflectivity can affect the cavity resonance

frequency, transmittance, reflectance, and more important its finesse. Thus, developing a model for wall effect consideration can lead us to understand different aspects of this effect.

To model a Gaussian beam propagation inside the cavity, the beam can be divided into rays with different intensity and angles. Therefore, the rays can have different incident angle and point. Here, we develop a geometrical optic model to calculate rays propagation. The local coordinate systems are assigned such as Figure 2.9. The coordinate system orientation (x_i and y_i direction) on each side keeps the same for any incident beam on that side but the origin of the coordinate system is on incident point. θ_i , incident angle, is the incident ray angle with the normal axis (y_i -axis of the coordinate system) and a_i is the distance between origin of the local coordinate system and the corner of the rectangle which is located on the left side of the origin (all parameters are presented in Figure 2.9). Depending on θ_i and a_i, there are four different ways for the beam to reflect back to the other sides which all possible conditions are presented in Figure 2.10.

The ray which is incident on the ith mirror can reflect to i+1, i+2, or i+3 mirror (actual mirror number is reminder of division of these numbers by four). If the length of ith side is w_i, the new reflection side can be calculated as following providing the incident angle is nonzero,

$$h_{i+1} = H(\theta_i)H\left(\theta_i - \text{atan}\frac{w_i - a_i}{w_{i+1}}\right),\ h_{i+2} = H(\theta_i)H\left(-\left(\theta_i - \text{atan}\frac{w_i - a_i}{w_{i+1}}\right)\right) +$$

$$H(-\theta_i)H\left(\theta_i + \operatorname{atan}\frac{a_i}{w_{i+1}}\right),\ h_{i+3} = H(-\theta_i)H\left(-\left(\theta_i + \operatorname{atan}\frac{a_i}{w_{i+1}}\right)\right); \qquad \text{Eq. 2-6}$$

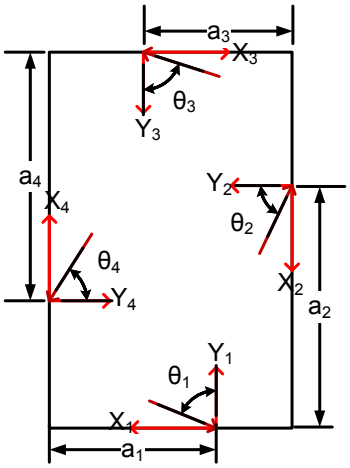

Figure 2.9. Local coordinate systems for beams calculations.

where H is a Heaviside function. If any of h_{i+1}, h_{i+2}, and h_{i+3} has a nonzero value, the reflected beam will be incident on that side. In most cases, only one of these parameters is not zero but there is a very rare case where the reflected light hits the corner of the cavity then the beam divides in two parts and each one travels in different direction. In this case, there is a bifurcation of light inside the cavity. The new incident angles and incident points are,

$$\theta_{i+1} = h_{i+1}\left(\frac{\pi}{2} - \theta_i\right), \qquad \theta_{i+2} = -h_{i+2}\theta_i\ , \qquad \theta_{i+3} = -h_{i+3}\left(\frac{\pi}{2} + \theta_i\right);$$

$$a_{i+1} = h_{i+1}a_i\cot\theta_i, \qquad a_{i+2} = h_{i+2}(w_i - a_i - w_{i+1}\tan\theta_i\ ),$$

$$a_{i+3} = h_{i+3}(w_{i+1} + a_i\cot\theta_i)\ . \qquad \text{Eq. 2-7}$$

Traveling of the beam inside the cavity cause a phase delay, which are defined as,

$$\delta_{i+1} = h_{i+1}ka_{i+1}\sec\theta_i, \delta_{i+2} = h_{i+2}kw_{i+1}\sec\theta_i,\ \delta_{i+3} = -h_{i+3}ka_i\csc\theta_i, \qquad \text{Eq. 2-8}$$

where k is the magnitude of the wave vector ($2\pi/\lambda$). The magnitude of reflected wave amplitude decays each time reflecting back from the mirror and its phase retards when it travels inside the cavity. The amplitude can be calculated as,

$$A_{i+1} = h_{i+1}A_i r_i e^{-j\delta_{i+1}}, A_{i+2} = h_{i+2}A_i r_i e^{-j\delta_{i+2}}, A_{i+3} = h_{i+3}A_i r_i e^{-j\delta_{i+3}}. \quad \text{Eq. 2-9}$$

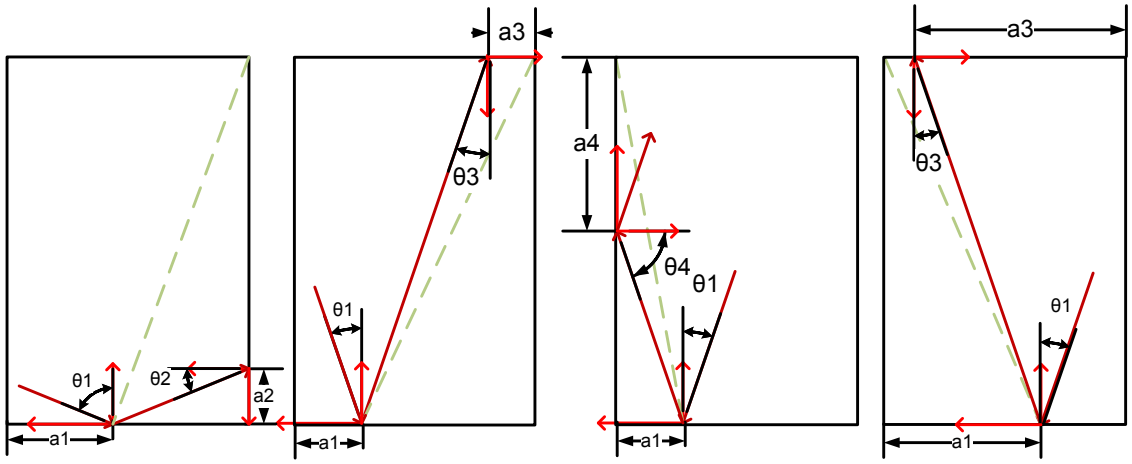

Figure 2.10. Different way which light can reflect back to the other sides.

where r_i is the reflectivity of the i[th] mirror. Each step the incident side, point, angle, and amplitude should be found from the current value of these parameters. Thereafter, each parameter should be updated in cavity matrix. The cavity matrix for iteration number p can be defined as,

$$ATA_p = \begin{bmatrix} A_1 & A_2 & A_3 & A_4 \\ \theta_1 & \theta_2 & \theta_3 & \theta_4 \\ a_1 & a_2 & a_3 & a_4 \end{bmatrix} \quad \text{Eq. 2-10}$$

If the output side is q[th] mirror then transmitted light amplitude can be found as,

$$A_t = t_q \sum_{p=1}^{\infty} ATA_p(1,q) \quad \text{Eq. 2-11}$$

and the transmitted light intensity is, $I_t = A_t^* A_t$.

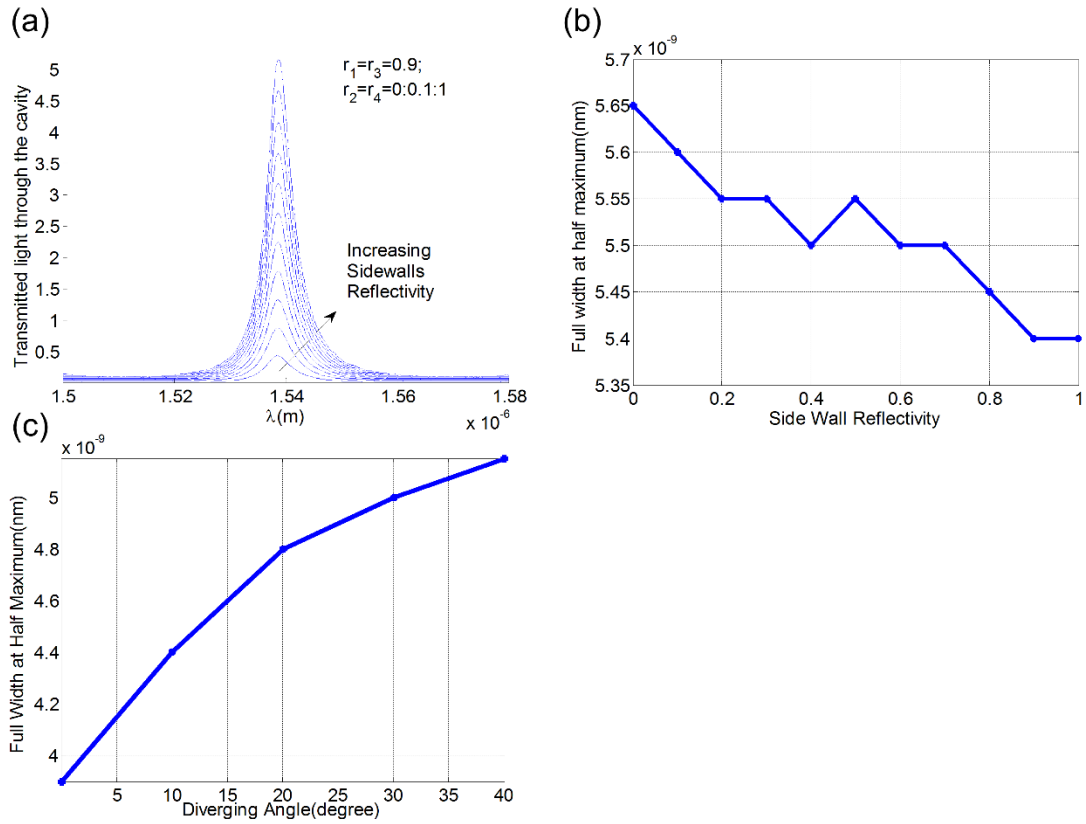

Figure 2.11. Wall reflectivity effect on (a) the frequency response and (b) finesse of system (c) variation of FWHM with increase of the beam diverging angle.

Considering $20\mu m \times 20\mu m$ cavity which consists of four mirrors the developed model has been used to model the propagation of Gaussian beam with same waist size as the cavity. The beam angle is varied between $-10°$ to $10°$. r_1 and r_3 are considered 0.9 and wall mirrors (r_2 and r_4) reflectivity varied between 0 to 1.

As we can see in Figure 2.11 (a), the transmitted intensity increases with increase of the mirror reflectivity. This is because part of reflected light from the side walls is in phase with the main part of emitted light and can increase the peak amplitude. However, the number which are presented in the Figure 2.11 (a) should be scaled properly. The full width at half maximum (FWHM) in Figure 2.11 (b) does not significantly change with

the side wall reflectivity. Therefore, the FWHM of the cavity is not highly dependent on the side walls reflectivity for low reflectivity mirrors. We completely discuss this effect in the next chapter and show that for the higher finesse cavity (higher reflectivity) the FWHM significantly varies in respect to the side wall reflectivity. The resonance wavelength does not vary with respect to the reflectivities of side walls. Therefore, for the lower finesse cavities, the free spectral range of the cavity remains constant, and the finesse of the etalon does not significantly vary with the side walls reflectivities. Figure 2.11 (c) presents the variation of the FWHM with respect to the diverging angle. As it can be seen in it, the FWHM increases with increase of the beam diverging angle.

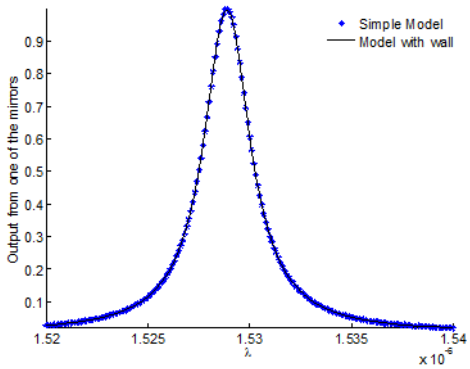

Figure 2.12. Comparing the infinite width model and the model which is considered wall effect in the special case.

The model has been verified for the case where side walls reflectivities are 100% and the incident angle is 45°. In this case, the modeled resonator behaves same as the Fabry-Peroty resonator with $\sqrt{2}$ times larger thickness. As we can see in the Figure 2.12, both models provide same result.

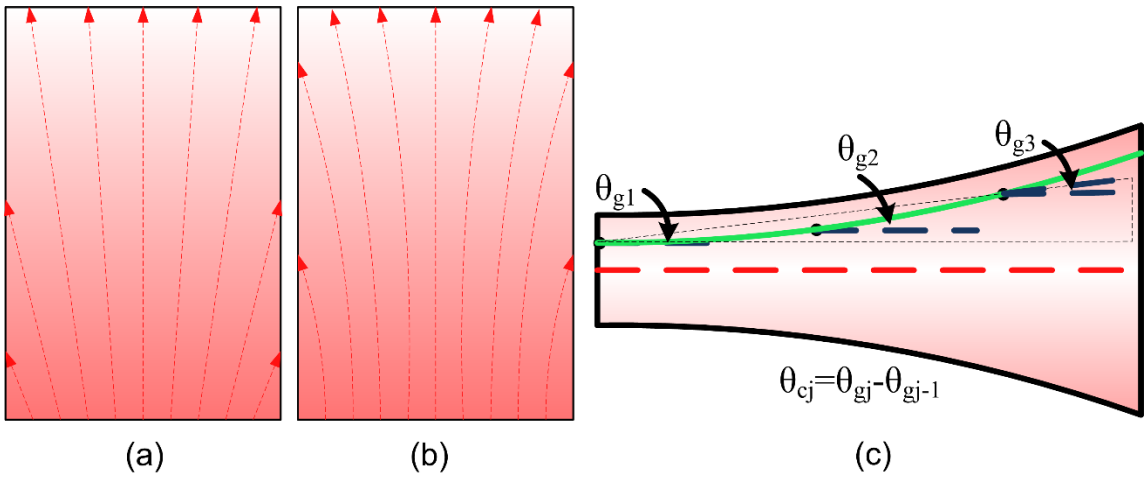

Figure 2.13. (a) The model without angular modification (b) the real model (c) the modified ray model.

2.4.1 Angular Modification

The current method becomes more accurate in consideration of the ray diffraction if the ray curvature is considered. In the previous section, the diverging angle of the beam was calculated at the Rayleigh range of the beam (Figure 2.13 (a)). Based on the beam diverging angle and Gaussian distribution of it, the specific angle was attributed to each ray as its initial angle. In the mentioned method, the propagation direction of the ray changes only if it strikes a mirror. However, in this section we consider the diffraction along the path of the ray (Figure 2.13 (b) and (c)). Here, the ray angle is updated among its path by the small correction angle determined by the beam free path diffraction. We assume there is no transfer of energy between two rays. Thus each ray preserves its energy and only its propagation angle varies due to its diffraction and interaction with the mirrors. The correction angle can be calculated as following (Figure 2.13 (c)),

$$\theta_{c_{j+1}} = \theta_{g_{j+1}} - \theta_{g_j} \qquad \text{Eq. 2-12}$$

where θ_{g_j} is the diverging angle of the ray at its j^{th} step.

To avoid the energy transfer between two rays during their propagation among the z-axis, each ray is considered as an expanding strip. It will be shown that the energy is conserved in each strip during the propagation. We need to find the strip which its carrying energy remains constant during its propagation. Now we need to find these strips and the centroid of them. The correction angle is determined by tracking the centroid of these strips. The electric field of the Gaussian beam is defined as,

$$\mathrm{E(r,z)} = \mathrm{E_0}\frac{\mathrm{w_0}}{\mathrm{w(z)}}\exp\left(-\frac{\mathrm{r^2}}{\mathrm{w^2(z)}}\right)\exp\left(-\mathrm{ikz}-\mathrm{ik}\frac{\mathrm{r^2}}{\mathrm{2R(z)}}+\mathrm{i\zeta(z)}\right) \qquad \text{Eq. 2-13}$$

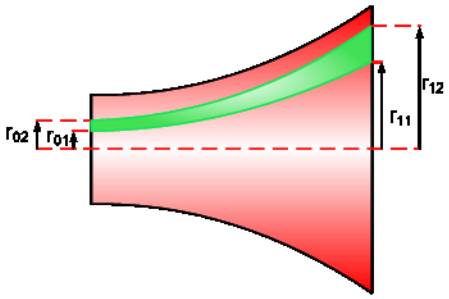

Figure 2.14. Expansion of the ray during its propagation.

where r is the radial distance from the beam propagation axis, z is the axial distance from the beam's waist, E_0 is the initial electric field, $w(z)$ is the radius at which the field amplitude drop by $1/e$, w_0 is the waist size, $R(z)$ is the radius of curvature of the beam wavefront, $\zeta(z)$ is the Gouy phase shift. $w(z)$ can be related to the w_0 by $\mathrm{w(z)} = \mathrm{w_0}\sqrt{1+(\mathrm{z/z_R})^2}$ and $z_R = \pi w_0/\lambda$. To find the energy conserved region, first we assume the amount of energy in $[r_{01}, r_{02}]$ at the waist of the beam is same as amount of energy in $[r_1, r_2]$ at distance z from the waist (Figure 2.14) and the relationship between r_1, r_2 and r_{01}, r_{02} is found. This assumption provides,

$$2\pi \int_{r_{01}}^{r_{02}} E(r_0,0)E^*(r_0,0)r_0 dr_0 = 2\pi \int_{r_1}^{r_2} E(r,z)E^*(r,z)rdr \qquad \text{Eq. 2-14}$$

Using the Gaussian beam general equation, the above equation is simplified to,

$$\int_{r_{01}}^{r_{02}} \exp\left(-\frac{2r_0^2}{w_0^2}\right) r_0 dr_0 = \frac{w_0^2}{w(z)^2} \int_{r_1}^{r_2} \exp\left(-\frac{2r^2}{w^2(z)}\right) rdr \qquad \text{Eq. 2-15}$$

Replacing r and r_0 in this integral with the $x_0 = \frac{r_0}{w_0}$ and $x = \frac{r}{w}$, the following integral can be derived,

$$\int_{\frac{r_{01}}{w_0}}^{\frac{r_{02}}{w_0}} \exp(-x_0^2)\, x_0 dx_0 = \int_{\frac{r_1}{w}}^{\frac{r_2}{w}} \exp(-x^2)\, x dx \qquad \text{Eq. 2-16}$$

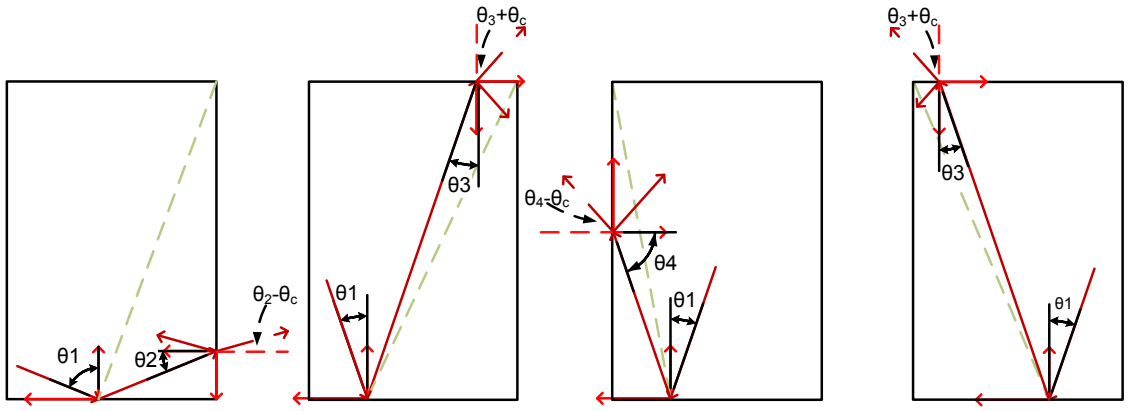

Figure 2.15. Application of the correction angle.

The above integral is satisfied if $r_{01}/w_0 = r_1/w$ and $r_{02}/w_0 = r_2/w$. Therefore, the electric field energy remains the same on each strip. In order to satisfy these conditions, $r_1 = \sqrt{1 + z^2/z_R^2}\, r_{01}$ and $r_2 = \sqrt{1 + z^2/z_R^2}\, r_{02}$. Hence the center of the ray diverging angle at $(j+1)^{st}$ step is,

$$\theta_{g_{j+1}}(r, z_j) = \tan^{-1}\left(\left(\sqrt{1 + \left(\frac{z_j}{z_R}\right)^2} - 1\right)\frac{r}{z_j}\right) \qquad \text{Eq. 2-17}$$

where, $z_j = z_{j-1} + \delta_j / k \cos\theta_{g_j}$. z_0 is the distance of the mirror from the waist at the first step. The correction angle for each step can be related to its previous conditions as,

$$\theta_{c_{j+1}} = \theta_{g_{j+1}} - \theta_{g_j} = \tan^{-1}\left(\left(\sqrt{1+\frac{z_j}{z_R}} - 1\right)\frac{r}{z_j}\right) - \tan^{-1}\left(\left(\sqrt{1+\frac{z_{j-1}}{z_R}} - 1\right)\frac{r}{z_{j-1}}\right)$$

Eq. 2-18

The new angles after applying the correction angle can be written as (Figure 2.15),

$$\theta_{i+1} = \left(\frac{\pi}{2} - \theta_i - \theta_{c_{j+1}}\right) h_{i+1}, \qquad \theta_{i+2} = -\left(\theta_i + \theta_{c_{j+1}}\right) h_{i+2},$$

$$\theta_{i+3} = -\left(\frac{\pi}{2} + \theta_i - \theta_{c_{j+1}}\right) h_{i+3}$$ Eq. 2-19

2.5 Conclusion

Air cavity optical resonators with a top polymer membrane were demonstrated for detection of high frequency ultrasound signals. In order to design the top membrane, a mechanical model that includes additive mass and damping of front water loading on the membrane was applied. For verification of the mechanical model with the experimental data, simple expressions for optical and mechanical sensitivity of the cavity detector were derived. Subsequently, the experimental test results were compared with the predictions of the theoretical model. A good agreement was found between the measured sensitivity and the model prediction. A device of 60 μm diameter and 8 μm membrane thickness was tested using a 25 MHz ultrasonic transducer. Although the device dimensions were not optimized for this frequency (regarding its sensitivity) the primary peak in the signal was

in good agreement with measurement of the same signal with a calibrated hydrophone. However, series of undesired low-frequency oscillations following the main signal is observed. These are probably caused by internal acoustic reflections in the Pyrex substrate. This effect can be removed using a thicker substrate or utilizing a wedge substrate which does not reflect back the ultrasound pulse. It can also be significantly reduced by employing a dense array of elements, thus preventing acoustic radiation from penetrating into the substrate. The noise equivalent pressure of the device is 9.25 kPa over the bandwidth of 28 MHz.

The main advantage of air-cavity etalon devices for ultrasound detection over solid polymer etalons is in the near-independent optimization of optical and mechanical properties. This stems from the fact that the mechanical active element (the top membrane) is separated from the optical resonator cavity (the air gap). The current design, however, does not fully exploit this advantage, and as a result the sensitivity of the devices tested is lower than results reported for solid polymer etalon detectors. We believe that a significantly higher optical sensitivity can be achieved by redesigning the optical cavity. This can be done by optimizing the fabrication process such as using a higher quality alignment system during the device bonding in step 8 of the fabrication process, or not etching the gold layer inside the cavity in step 6. A promising future direction is the idea of adding lateral light confinement by gold sputtering on the side-walls and removal of the bonding layer between the mirrors. This would result in 3-D

light confinement in a cylindrical volume similar to vertical microcavities used in vertical-cavity surface-emitting laser applications.

We expect a 6-fold increase in the device sensitivity by application of the optical design improvements mentioned above. Furthermore, optimization of the mechanical parameters of the device can further increase the sensitivity of the device. However, the optimal values for the mechanical design parameters were not achievable due to fabrication difficulties. In addition to these design modifications, higher SNR can be achieved by improving the photodetector system.

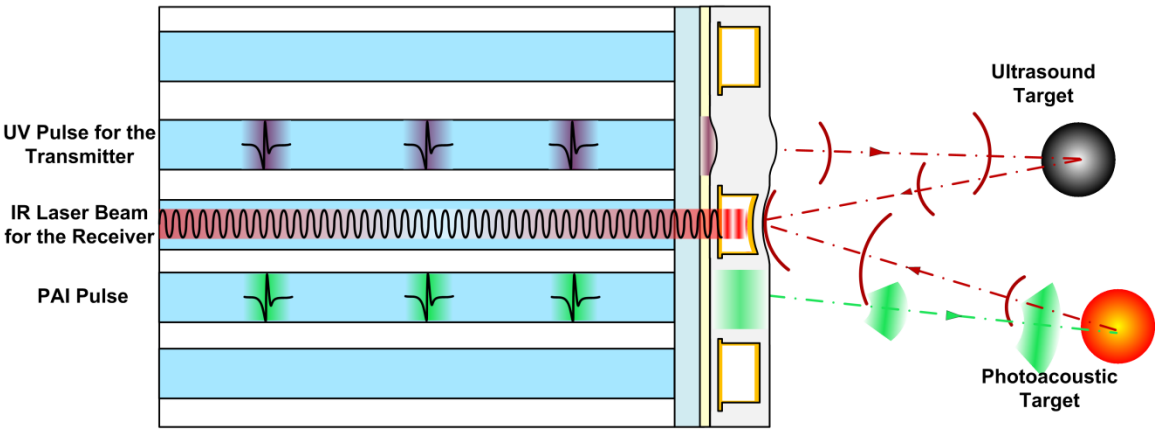

Figure 2.16. Schematic of dual modalities probe based on air-gap optical cavity.

To make the device more commercially attractive in comparison with alternative ultrasound transducer technologies, it is essential to integrate ultrasound transmission functionality to the design. The transmitter elements can be integrated with the receiver elements by adding a photo-absorptive layer underneath the receivers (Figure 2.16). A coherent multimode optical fiber bundle, similar in construction to imaging bundles used in endoscopic applications, can be used for this application. The distance between the

transmitter and receiver can be 10-20 μm and the distance between two neighboring receivers can be 20-40 μm. The proposed all-optical transmitter/receiver device can be utilized for ultrasound and photoacoustic imaging. The photoacoustic excitation pulse can pass through the area between the receivers because the transmitter layer is transparent to the wavelengths used for photoacoustic imaging. Obviously, the optical receiver can be employed to detect the generated ultrasound. Lastly, there is a need for simplifying the fabrication process in order to reduce manufacturing cost.

Chapter 3. Waveguide Fabry-Perot resonators

Although the application of air-gap ultrasound detector by mechanical flexibility improvement has shown promising results, the demonstrated sensitivity is not high enough for real-time clinical imaging applications such as intravascular ultrasound (IVUS) imaging. Clearly, there is a need to increase the optical quality (Q) factor without sacrificing the small volume confinement of the optical field. Therefore, we need to find a new mechanism to fulfill these requirements.

An optical resonator is an arrangement of optical components that allows a beam of light to circulate in a closed path [14]. Fabry-Perot interferometers, whispering gallery resonators and photonic crystal microcavities are the most common light confinement mechanisms for this circulation on the micrometer scale [51]. Fabry-Perot resonators are utilized in semiconductor quantum boxes as micropillar resonators to enhance the spontaneous emission rate [52]. Using an ultrahigh Q Fabry-Perot resonator, Hood et al. have demonstrated detection of single atom trajectories [53]. Pruessner et al. have applied

the high Q Fabry-Perot resonator to characterize their waveguide microcavity optomechanical system [54]. Adding a Gaussian-shaped defect in a vertical Fabry-Perot microcavity, Ding et al. have predicted higher Q factor and mode confinement using 3D finite difference time domain calculations [55]. Whispering gallery modes, another approach to closed-loop light circulation, are applied in microdisks [56, 57], microspheres [58] and microtoroids [59]. Finally, photonic crystals having a defect are another class of optical microresonators that are designed [60] and fabricated [61] in many different ways to achieve the highest Q-factor.

In this chapter, we introduce a simple method to increase the Q-factor of polymeric Fabry-Perot resonators and show that this method can improve the Q-factor by one or more orders of magnitude depending on the reflectivity of the mirrors and the cavity length. This has been done by inducing a small refractive index change in the layer between the mirrors creating a waveguide. To model this structure, we have developed a simple theoretical model for resonators with and without the waveguide. We show that adding a waveguide can significantly improve the device Q-factor in the case of highly reflective mirrors and long cavities. After presenting the modeling results, we describe the fabrication and testing of a device fabricated using a UV-writeable, diffusive photopolymer. Finally, we discuss future directions in developing this technology for miniaturized, fiber optic-based ultrasound imaging devices.

3.1 Device Principles

The finesse of an optical resonator can be defined as the number of light oscillations between two mirrors at the free space wavelength (λ) before its energy decays by a factor of e^{-} [62]. Thus the optical path required to achieve this finesse is $2nL\mathcal{F}$ where *n, L,* $\mathcal{F}$ are the refractive index inside the cavity, the length of the cavity, and the finesse respectively. Diffraction, the spreading of light during propagation, causes energy to leak out of the resonator. The farther the light propagates, the greater the amount of energy that is lost from the cavity.

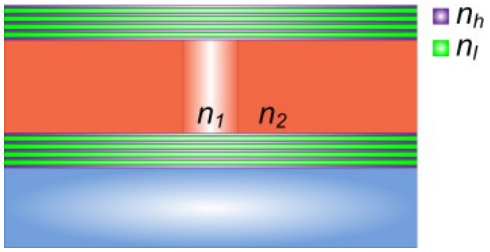

Figure 3.1. Schematic of the Fabry-Perot Resonator with a waveguide having a core refractive index of n_1 and a cladding refractive index of n_2. The layers of dielecteric mirrors are presented by high (n_h) and low n_l refractive index.

Therefore as one tries to create cavities with higher finesse and Q-factors, the required optical pathlength increases causing a more significant diffraction effect. The effects of diffraction can be eliminated, however, if the light passes through a waveguide between the two mirrors (Figure 3.1). This can be done by inducing a small refractive index modulation to create a waveguide in the cavity. In Sections 3.1.1 and 3.1.2, we model propagation of the Gaussian beam inside the cavity without and with the waveguide structure, respectively. We compare the results for both cavities and

demonstrate that the waveguide can improve the finesse and Q-factor of the cavity by over an order of magnitude depending on the cavity length and reflectivity of the mirrors.

3.1.1 Modeling of the cavity without waveguide

The unfolded equivalent model of wave propagation inside both cavities can be seen in Figure 3.2 (a) and (b). To model the propagation of the wave inside the cavity without the waveguide, we assume that the cavity does not affect the propagation parameters of the beam and only decreases the beam amplitude by a factor of $\sqrt{R_1 R_2}$ during each oscillation where R_1 and R_2 are the mirrors reflectivities. We consider the incident light as a Gaussian wave with the electric field phasor [63]

$$E_0(r,z) = A_0 \frac{w_0}{w(z)} \exp\left[-i\left(kz - \eta(z)\right) - r^2\left(\frac{1}{w(z)^2} + i\frac{k}{2R(z)}\right)\right] \qquad \text{Eq. 3-1}$$

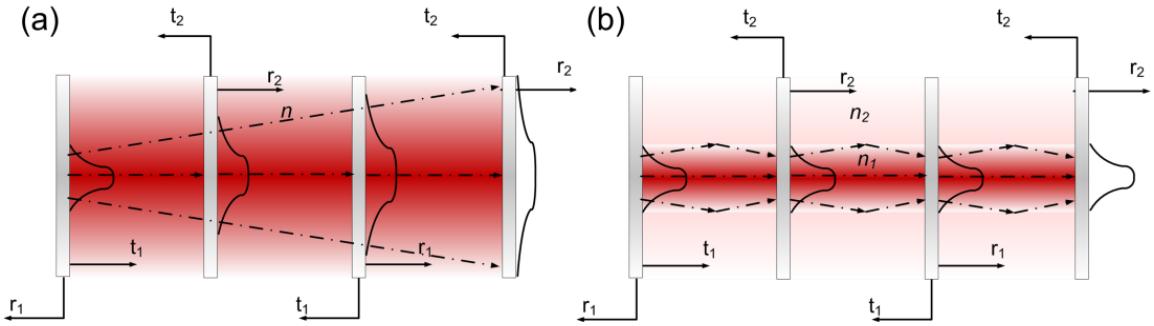

Figure 3.2. Gaussian beam propagation in the cavity (a) without and (b) with waveguide embedded in the Fabry-Perot etalon layer (t:transmission, r:reflection).

where r is the radial distance from the center of the beam, z is the axial distance from the beam waist, k is the wavenumber ($2\pi n/\lambda$), A_0 is the electric field amplitude at its waist, w_0 is the waist size, $w(z) = z_0\sqrt{1 + z^2/z_0^2}$, $R(z) = z(1 + z^2/z_0^2)$, $\eta(z) = \tan^{-1} z/z_0$

and z_0 is the Rayleigh range determined by $\pi n w_0^2/\lambda$. The electric field amplitude of the s-th reflection (B_s) can be calculated:

$$B_0(r) = -\sqrt{R_1}\,E_0(r,0),\ B_s(r) = T_1\sqrt{R_2}\left(\sqrt{R_1R_2}\right)^{j-1}E_0(r,2sL),\ \text{for } s > 0 \quad \text{Eq. 3-2}$$

where T_1 is the transmittance through the first mirror. The total reflected field at each point is

$$B_t(r) = \sum_{s=0}^{\infty} B_s(r) = -\sqrt{R_1}E_0(r,0) + T_1\sqrt{R_2}\sum_{s=1}^{\infty} B_s(r)\left(\sqrt{R_1R_2}\right)^{s-1}E_0(r,2sL) \quad \text{Eq. 3-3}$$

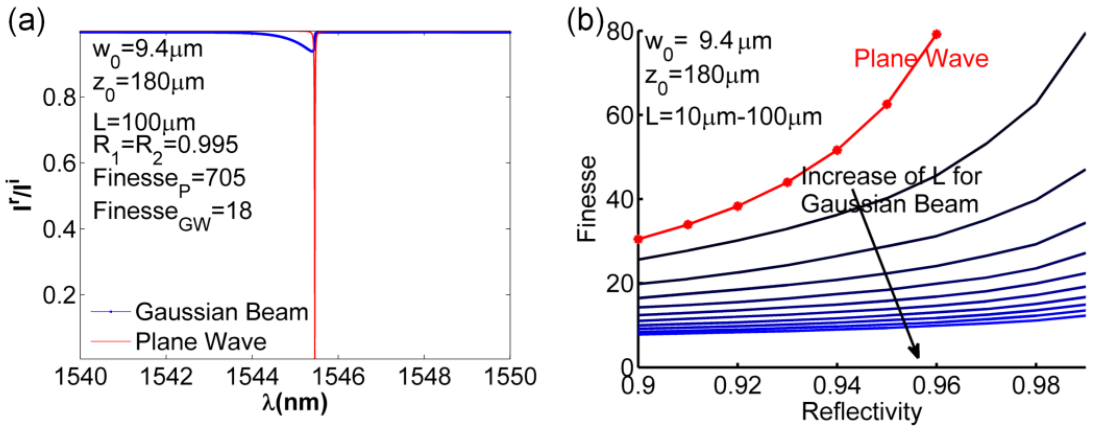

Figure 3.3. (a) Resonance reflection spectrum of a 100 μm Fabry-Perot optical resonator excited with a Gaussian wave and a plane wave. (b) Finesse variation versus reflectivity for different cavity length with 10 μm steps.

and the total intensity is $I_t(r) = B_t(r)B_t^*(r)$. Then, the total power of the reflected light (P_t) is,

$$P_t = 2\pi\int_0^{r_{domain}} I_t(r)rdr \quad \text{Eq. 3-4}$$

the value of r_{domain}, which indicates the domain of integration. This value varies depending on the method which is used to the reflected light. Figure 3.3 (a) shows the reflected light intensity as a function of the incident wavelength for a plane wave and a

Gaussian wave. The graph corresponds to a beam waist radius of 9.4 μm, which is the approximate value for our actual beam size; the reflectivity of the mirrors was set to be 0.995 and the cavity length is 100 μm. As we can see, the case of plane wave illumination has a much sharper dip than that of Gaussian wave and a 39 times larger finesse.

In Figure 3.3 (b) we show finesse versus reflectivity for different cavity lengths for the case of $n=1$. For the Gaussian beam resonator, increasing both the cavity length and mirror reflectivity causes the cavity finesse to drastically deviate from the plane wave predicted value. The main reason for the lower finesse for the Gaussian wave in this case is the variation of the wave-front amplitude and phase profile during propagation resulting in a phase mismatch of successive reflections.

3.1.2 Modeling of the cavity with waveguide

In this section, we show that the waveguide optical cavity can behave as a plane wave cavity. Therefore, it is possible to design a very high Q-factor and finesse Fabry-Perot resonator, limited only by absorption in the mirrors and bulk polymer layer. To model wave propagation inside the cavity with the waveguide for photon confinement, we assume that the light travels inside the cavity with the propagation parameters and profile of a circular dielectric waveguide. The beam amplitude is assumed to decrease by a factor of $\sqrt{R_1 R_2}$ during each oscillation.

The optical cavity consists of a core with a refractive index of n_1 and a radius of a surrounded by the cladding with a refractive index of n_2. The Cartesian components of an

electric field for approximately y-polarized light with a small z-component in cylindrical coordinates are [63]:

$$E_{x_{lm}}(r,\phi,z) = 0; E_{y_{lm}}(r < a,\phi,z) = A_{lm}J_l(h_{lm}r)e^{il\phi}e^{-i\beta z},$$

$$E_{y_{lm}}(r > a,\phi) = B_{lm}K_l(q_{lm}r)e^{il\phi}e^{-i\beta_{lm}z};$$

$$E_{z_{lm}}(r < a,\phi,z) = \frac{h_{lm}}{\beta_{lm}}\frac{A_{lm}}{2}\left[J_{l+1}(h_{lm}r)e^{i(l+1)\phi} + J_{l-1}(h_{lm}r)e^{i(l-1)\phi}\right]e^{-i\beta_{lm}z},$$

$$E_{z_{lm}}(r > a,\phi,z) = \frac{q_{lm}}{\beta_{lm}}\frac{B_{lm}}{2}\left[K_{l+1}(q_{lm}r)e^{i(l+1)\phi} - K_{l-1}(q_{lm}r)e^{i(l-1)\phi}\right]e^{-i\beta_{lm}z}; \quad \text{Eq. 3-5}$$

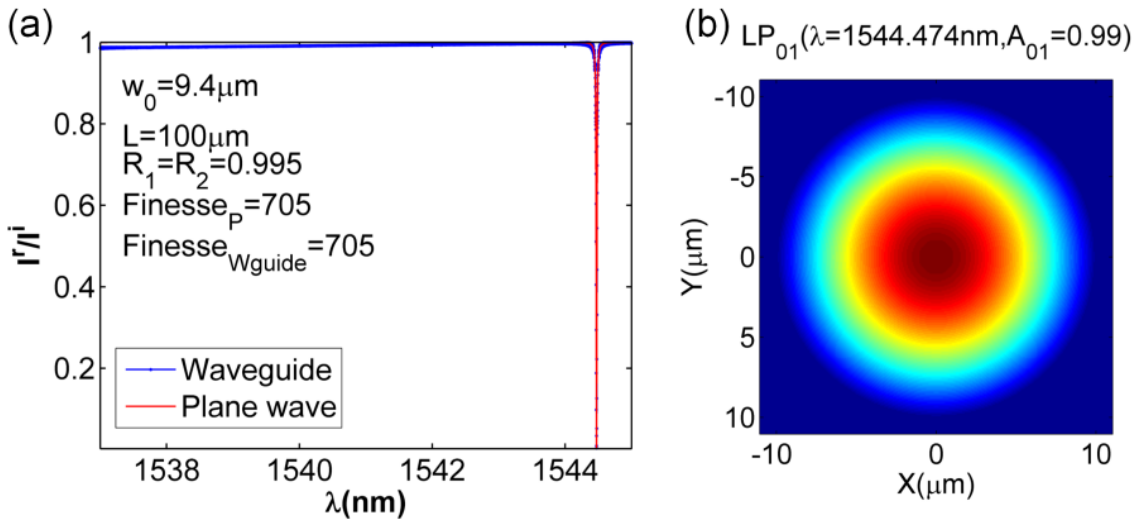

Figure 3.4. (a) Comparison of plane-wave resonance in an un-guided cavity with multi-mode resonance in the waveguide cavity, (b) cross-sectional plot of the modes inside the waveguide cavity.

where lm indicates the mode number for different modes (LP_{lm}) , A_{lm} is the mode factor and $B_{lm} = A_{lm}J_l(h_{lm}a)/K_l(q_{lm}a)$. The mode factor is dependent on the mode shape and the incident light profile. β_{lm} is the propagation constant, $q_{lm} = \sqrt{\beta_{lm}^2 - n_2^2k_0^2}$, $h_{lm} = \sqrt{n_1^2k_0^2 - \beta_{lm}^2}$. For LP_{lm} mode, the propagation parameter can be calculated using

$h_{lm}aJ_{l+1}(h_{lm}a)/J_{l+1}(h_{lm}a) = q_{lm}aK_{l+1}(q_{lm}a)/K_l(q_{lm}a)$, where m is defined as the m-th root of this equation. The electric field for the specific mode can be written as $\mathbf{E}_{lmz}(r,\phi,z) = E_{x_{lm}}\mathbf{e_x} + E_{y_{lm}}\mathbf{e_y} + E_{z_{lm}}\mathbf{e_z} = E_{lm}(r,\phi)e^{-i\beta_{lm}z}$. Following the same method for the derivation of Eq. 3-3, the reflected electric field for the *lm* mode can be calculated:

$$\mathbf{B}_{t_{lm}}(r,\phi) = \mathbf{E}_{lm}(r,\phi)\left[-\sqrt{R_1} + T_1\sqrt{R_2}\sum_{s=1}^{\infty}\left(\sqrt{R_1R_2}\right)^{s-1}e^{-i\beta_{lm}2sL}\right] \quad \text{Eq. 3-6}$$

assuming $\beta_{lm} = n_{eff_{lm}}k_0$. The effective index, $n_{eff_{lm}}$, can be considered a constant close to the resonance frequency. For each mode in Eq. 3-6, the electric field distribution ($\mathbf{E}_{lm}(r,\phi)$) and its integral are slowly varying with respect to variation of the wavelength and can be treated as a constant. Therefore, for each mode, $\mathbf{E}_{lm}(r,\phi)$ does not affect the characteristic curve. The total reflected electric field is, $\mathbf{B}_t = \sum_{l=0}^{\infty}\sum_{m=1}^{\infty}\mathbf{B}_{t_{lm}}$. Using the same parameters as the cavity without the waveguide, we used a 100 μm cavity length with mirror reflectivities of 0.995 and a Gaussian beam of radius 9.4 μm. n_1 and n_2 are 1.53 and 1.50 respectively. The core radius is 10 μm. In the first fourteen modes of the waveguide, only four of them have nonzero contributions in response to the Gaussian beam. Among these four modes 99% of the light is coupled to the L_{01}. Therefore, as we see in Figure 3.4 (a) with Gaussian beam illumination, the finesse of the waveguide optical cavity will be exactly the same as the plane wave cavity with approximately the same effective refractive index. This shows that the only limitation for the waveguide cavity to achieve a very high Q-factor or finesse is the material absorption.

Material absorption in the cavity medium or in the mirror material would reduce the quality of the resonance. We have not explicitly considered the diffraction of light inside the layers of the dielectric Bragg reflector. However, this diffraction might slightly decrease the finesse of the cavity and might shift its resonance frequency as well [64]. From Figure 3.4 (a), we can identify the excitation of some other modes, however, these modes are not as significant as the first mode. The normalized amplitude of the first mode shown in Figure 3.4 (b) is about 0.99. Although the higher modes do not affect the finesse of the system they can be removed by having the normalized frequency ($V = ak_0\sqrt{n_1^2 - n_2^2}$) below 2.4. In this case, the cavity only supports the LP_{01} mode which is known as the fundamental mode. Therefore, with a refractive index change of about 0.003 in a 4 μm radius cavity the higher modes will vanish. The other way to remove the higher modes in the cavity without a waveguide is to use an aperture to create an effective Fresnel number (e.g., $a^2/2L\lambda$) below 3 [65]. However, in this case it is unlikely that high finesse can be achieved since there is a change in the phase profile of the propagating light.

3.2 Fabrication

The fabricated device consists of two dielectric Bragg reflectors with a 100 μm thick polymer layer between them. A 4 μm dielectric Brag reflector is designed to have high UV transmittance and with more than 99% C-Band NIR reflectance (Evaporated Coatings, Inc., Willow Grove, PA). The holographic photopolymer utilized to fabricate this device is a thiol-ene/methacrylate photopolymer whose optical index can be modified

utilizing standard photo-lithography processes [66]. Holographic photopolymers, also known as diffusive photopolymers, are a class of polymers that self-develop refractive index structures in response to optical exposure. In these materials, optical exposure locally consumes monomer, driving in-diffusion of replacement monomer which increases the index of refraction [66]. Figure 3.5 (a) shows the steps required to make the device. The chromium mask is built on one of these mirror-coated wafers (step 1). The mask has been made on the uncoated side of the borofloat wafer, 500 μm away from the miror surface, to avoid any interference between the chromium film and the optical cavity. Then the mirrors are separated with a 100 μm spacer and the gap between them is filled with the photopolymer (step 2).

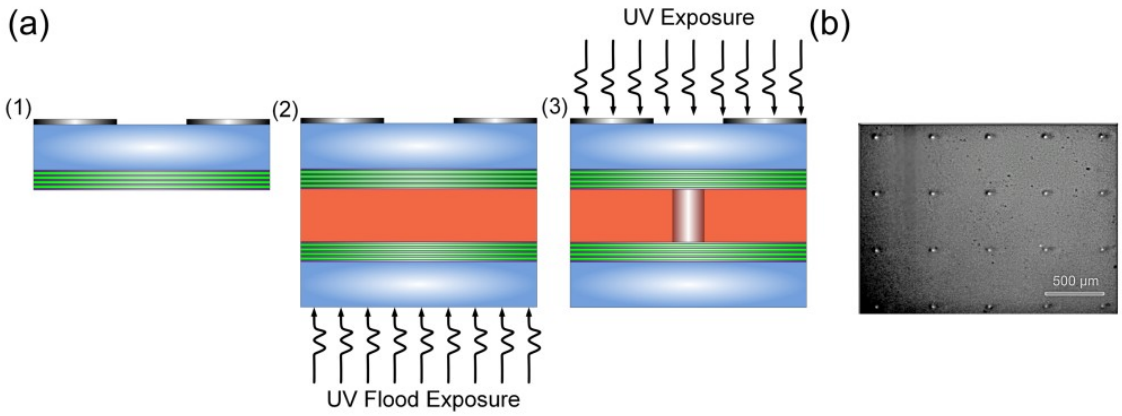

Figure 3.5. (a) Fabrication steps of waveguide-Fabry-Perot device by permanent refractive index modification in a photopolymer, (b) microscope image of the fabricated array of the devices.

The polymer is exposed from the backside for 54 s using the 13.5 mW/cm^2 UV mercury arc lamp to bring the polymer to its gel point [66]. An optical filter has been applied to 365 nm with the narrow line-width lamp. Then the fabricated mask, consisting of circle sizes of 5-15 μm, is exposed for 110 s from the mask side to expose the cavity area (step 3). In this step, the refractive index of the exposed area is around 1.521 which is 0.03

higher than the unexposed area [66]. Since the mask is 500 μm away from the polymer, using the Fresnel diffraction theorem, the radius of the generated cavities is calculated to be 5-20 μm (Figure 3.6). Finally the device is placed in the dark for two days for the monomer to diffuse to the center of the waveguide region creating a roughly uniform index across the center of the waveguide. Figure 3.5 (b) shows an array of resonators. The distance between them is about 500 μm.

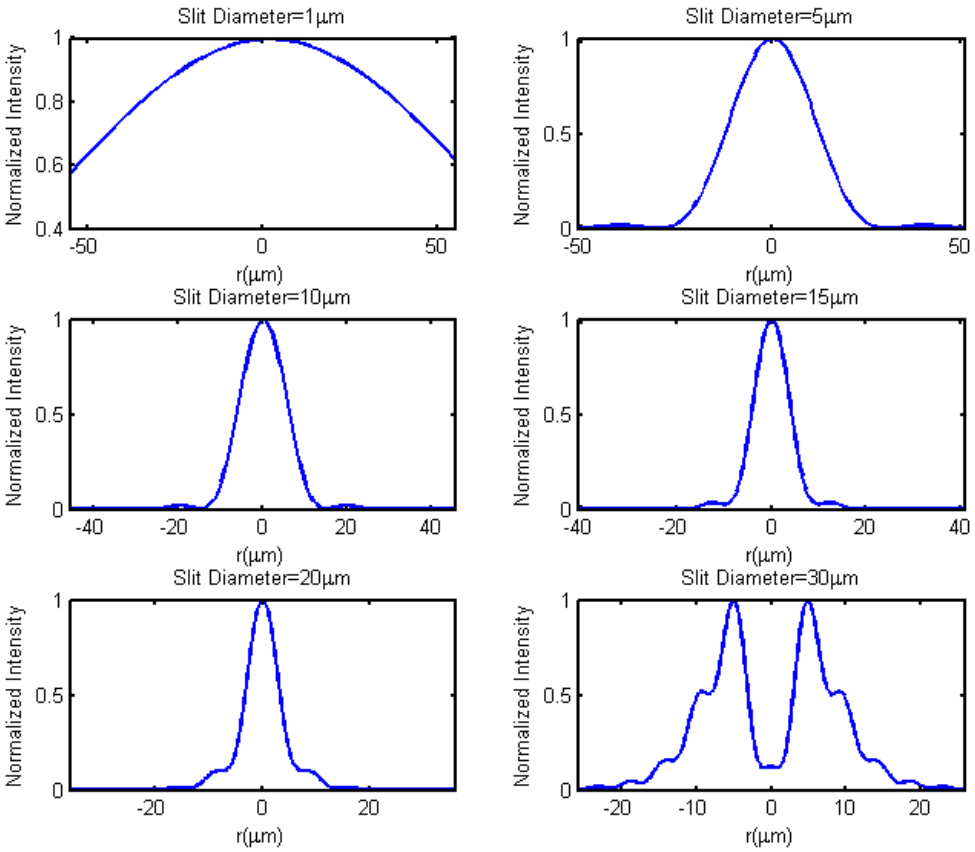

Figure 3.6. Fresnel diffraction pattern in different distance from the center (r) at 500 μm away from the slits with different diameter.

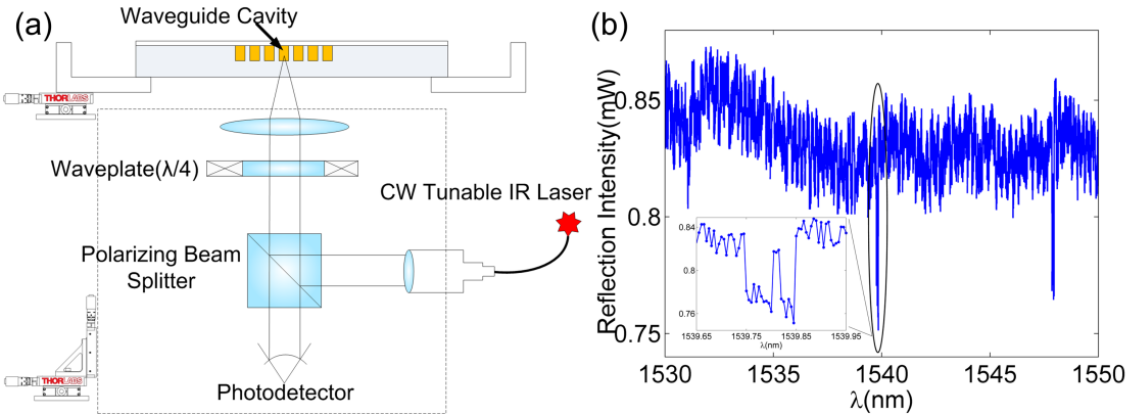

Figure 3.7. (a) The experimental set-up for testing reflection spectrum of the device (b) characteristic reflection spectrum curve of the tested device.

3.3 Experimental Testing of the Resonator

To test an optical cavity with a 20 μm diameter, we use the experimental set-up shown in Figure 3.7 (a). Light from an infrared laser source is coupled to the cavity using a collimator, polarized beam splitter, a λ/4 waveplate, and a lens. Linearly polarized light from a continuous near infrared (NIR) tunable laser source (8168F, Agilent HP) is transmitted to the collimator through a polarization-maintaining single-mode fiber with mode field diameter of 10.5 μm. The linearly polarized collimated beam is reflected by 90° by the polarizing beam splitter. The λ/4 waveplate changes the linear polarization to circular polarization. An IR camera (1/2" CCD, Cat#56-567, Edmund Optics) is used to visualize the cavity from the top to align and couple the beam to a specific cavity element in the wafer that typically holds a large number of elements of different cavity radii. The circularly polarized light is coupled to the cavity using a lens. With our arrangement of lens and collimator, the spot size of the focused beam is approximately 18.8 μm. Upon reflecting from the device and passing through the λ/4 waveplate a second time, the

resulting polarization is linear and perpendicular to the incident polarization. Because of the rotated polarization, the beam passes through the beamsplitter and is detected by a power meter.

To find the resonance wavelength of the optical cavity, the NIR wavelength is scanned from 1530 nm to 1550 nm. The reflected light intensity is recorded using an optical power meter (PM100 optical power meter with S122B Germanium Sensor, Thorlabs) and the results are presented in Figure 3.7 (b). The finesse of the optical cavity is about 682 and the Q-factor is about 55000 with a full width half maximum (FWHM) of about 0.031 nm and an average free spectral range of 8.45 nm. The noise in the characteristic curve shown in Figure 3.7 (b) is mainly due to laser and photodetector noise. As we can see in Figure 3.7 (b), there are two different modes involved in the characteristic curve. One of them is the first mode (LP_{01}) and since the device is not a single mode cavity the second dip can result from coupling of light to other modes. Based on our theoretical calculation, this second dip can be due to the LP_{61} mode that has a resonance wavelength of 0.086 nm smaller than the first mode. Although it appears that this mode participation amplitude should be zero with fully Gaussian beam imperfect illumination might result in enhancement of this mode. This additional mode can be eliminated either by decreasing the refractive index difference between the core and cladding or decreasing the size of the cavity. Due to the low tuning resolution of our laser and the noises from the photodetector, the dip does not have a completely Lorentzian shape. The measured characteristic curve was repeatable over different cavities in the

wafer and was independent of alignment accuracy. We measured the characteristic curve for cavities without a waveguide structure and did not find any resonance for these cavities. This is likely due to the fact that the signal was small and unresolved within our current signal to noise ratio limits.

3.4 Phase Sensitivity Multiplication in Optical Resonators

In most of sensors based on optical resonators, the variation of the optical phase/path (dδ) due to the change in the optical path, or refractive index are related to the variation of the light intensity (dI) to sense the sensing variable. The optical phase sensitivity can be defined as dI/dδ where $\delta=2k_zL$, and k_z is the z-component of the wave vector. Here to increase the phase sensitivity, we propose to use a two arms system for the detection systems that there are some limitations on amount of power coupled to the optical cavity (Figure 3.8). Adding a second arm with a proper phase delay, the optical phase sensitivity can be linearly magnified by magnitude of electric field.

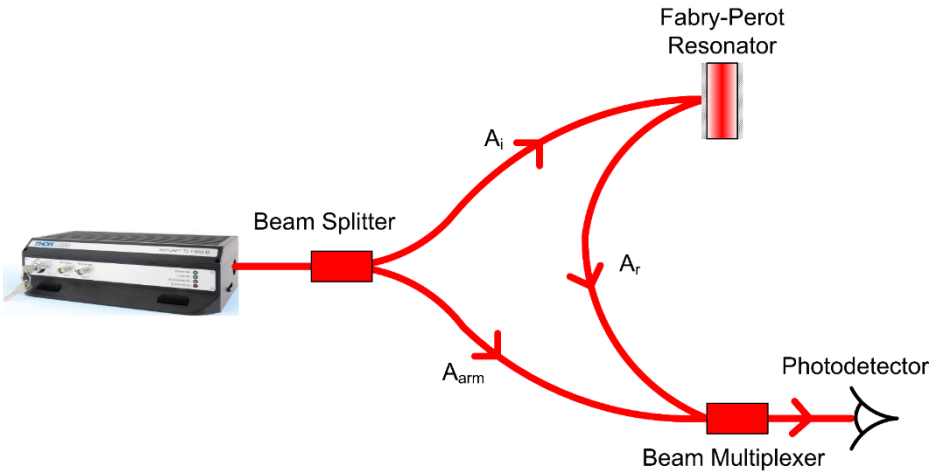

Figure 3.8. The two arms system for the phase sensitivity increase.

As we can see in Figure 3.8, light emitted from continuous wave coherence single wavelength laser source is divided in two arms. The first arm (A_i) is directed to the optical resonator and the second arm (A_{arm}) after application of the proper phase delay is directly guided to the beam multiplexer for adding two same wavelength beams. A_i after multiple reflection at the optical resonator (A_r) is redirected toward the multiplexer to add to the other delayed arm. Finally the combined light is conducted to the photodetector for detection of the favorite signal.

The combined light amplitude (A_t) and intensity (I_t) respectively are,

$$A_t = A_r + A_{arm}, I_t = (A_r + A_{arm})(A_r^* + A_{arm}^*) \quad \text{Eq. 3-7}$$

where the reflected light from the optical resonator (A_r) is,

$$A_r = A_i \frac{(1-e^{i\delta})}{1-Re^{i\delta}} \quad \text{Eq. 3-8}$$

where $R = \sqrt{R_1 R_2}$. The optical phase sensitivity can be calculated using,

$$\frac{d(I_t/I_i)}{d\delta} = \frac{2\sin\delta\, R(R-1)^2}{(R^2 - 2R\cos\delta + 1)^2} + i\sqrt{R}\left[\frac{A_{arm}^* \exp(i\delta)}{A_i^*(Rexp(-i\delta) - 1)} - \frac{A_{arm}\exp(-i\delta)}{A_i\ (Rexp(i\delta) - 1)} + \frac{RA_{arm}^*\exp(-i\delta)\,(\exp(i\delta) - 1)}{A_i^*(R\exp(-i\delta) - 1)^2} - \frac{RA_{arm}\exp(i\delta)\,(\exp(-i\delta) - 1)}{A_i\ (R\exp(i\delta) - 1)^2}\right] \quad \text{Eq. 3-9}$$

The first term in this equation is coming from the phase sensitivity without any arm. As we can see, this term is independent of the A_{arm} and only depends on the optical properties of the resonator. However, the other terms are proportional to the magnitude of the A_{arm}. Figure 3.9 (a &b) shows the variation of the optical phase sensitivity $(d(I_t/I_i)/d\delta)$ with respect to the phase variation (δ/π) and the phase delay between the arms $(\Delta\phi/\pi)$ when R=0.80 and $A_{arm}=A_i$. The maximum sensitivity is acheived when the phase delay between the arms is 0.64π rad.

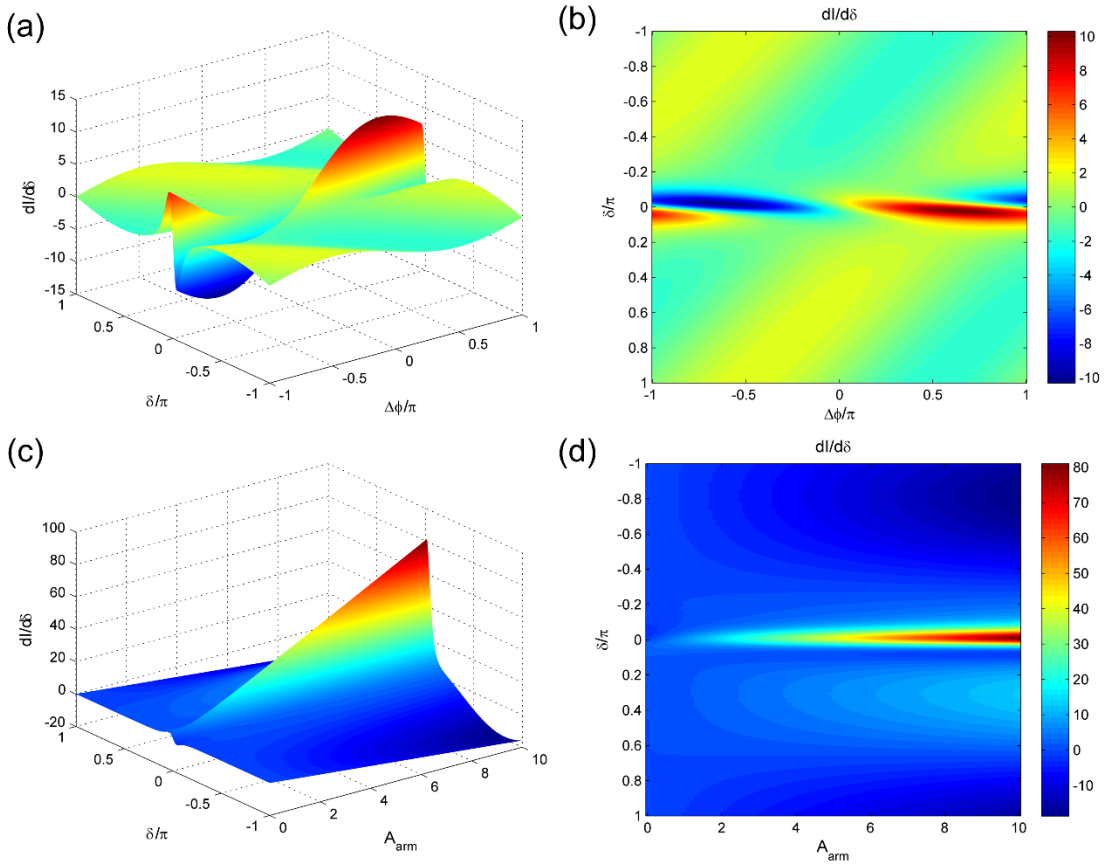

Figure 3.9. (a & b)The phase sensitivity variation with respect to phase and the arm phase delay; (c & d) phase sensitivity versus A_{arm} variation for $\Delta\phi = 0.64\,\pi$ rad.

Applying above optimum delay between the arms, the variation of the optical phase sensitivity versus the phase variation and A_{arm} is presented in Figure 3.9 (c & d). As we can see in Figure 3.9 (c), the phase sensitivity almost linearly increases and is about $3A_{arm}/A_i$. This equation can slightly vary depending on the mirrors reflectivities. Figure 3.10 compares the phase sensitivity of the systems with and without arm with reflectivity of 0.80 and 0.99. The phase sensitivity of the system with arm with R=0.80 and R=0.99 is respectively 29.94 and 30.26 times larger than the system without arm with the same reflectivity.

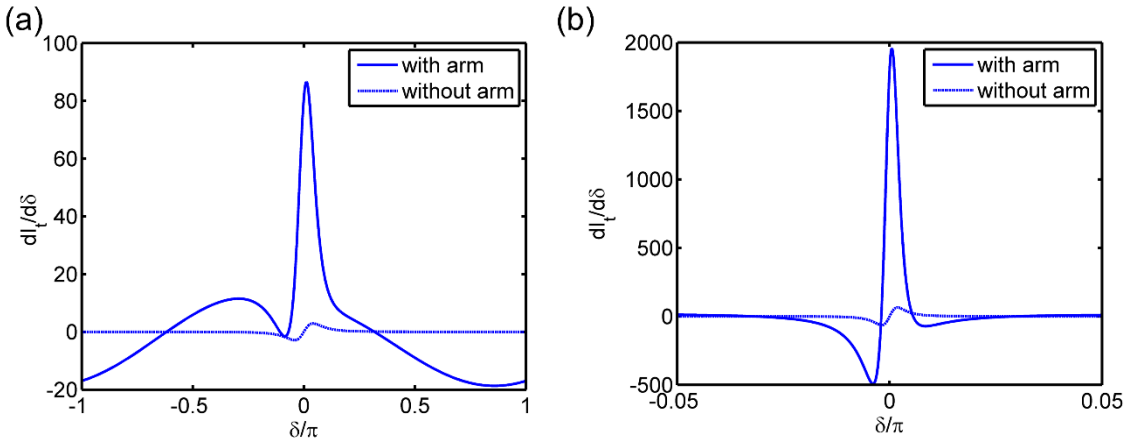

Figure 3.10. Comparing phase sensitivity for (a) R=0.80 and (b) R=0.99.

Since the measured phase sensitivity is $\frac{dI_t}{d\delta} = \frac{d(I_t/I_i)}{d\delta} I_i$, *always the maximum allowable light intensity should be coupled to the optical resonator*. If there is any additional energy from the coherence light source that can be applied to the second arm which as we showed earlier can significantly increase the phase sensitivity of the sensor. This system can be used for light modulation if the phase change is applied to the optical

resonator. Furthermore, it can be used for optical phase imagining if the second arm uses as an imaging arm.

3.5 Conclusion

In this chapter, we present a method that significantly improves the Q-factor and finesse of polymeric Fabry-Perot resonators. By creating a waveguide inside the cavity, a confined mode propagates in the cavity having a phase-front perfectly matched to the flat mirror geometry. This improves the sharpness of the resonance peak by one or more orders of magnitude. This method also keeps the coupled light energy confined to a smaller volume, which is extremely important in applying the technology to miniaturized ultrasound imaging devices. Further improvement of the characteristic curve of the resonator is expected by integrating the cavity onto the tip of an optical fiber. In this way, we expect better coupling due to higher overlap between the fiber modes and the cavity modes. Additionally, higher modes can be eliminated by using a single-mode cavity design.

To achieve single-mode operation, we can either decrease the radius of the cavity or induce a smaller refractive index difference between the core and cladding of the waveguide. To decrease the refractive index difference between the core and cladding, the device is flood-cured under UV light for 270 s from the back-side to fully cure the polymer and use up any remaining monomer chemistry after the final diffusion step. In this case, the expected refractive index change is about 0.006 instead of the current value which is 0.03 [66].

One of the major advantages of this device is its compatibility with imaging fiber bundles. Large arrays of several thousands of high Q-factor resonators can be fabricated on the tip of a mirror-coated optical fiber bundle without any need for alignment or a complicated fabrication process. In next chapters, we apply this device to create high-resolution, miniaturized 3D ultrasound imaging probes in medical imaging applications.

Chapter 4. Waveguide Fabry-Perot resonator for ultrasound detection

In the previous chapter, we have proposed an approach to stabilize the resonance in a thin film by using a vertical waveguide. We have achieved high finesse (695) and quality factor (59000) in a waveguide, Fabry-Perot film resonator of 100 μm thickness. Here we describe the fabrication and implementation of this type of optical cavity for a thin-film ultrasound detector.

The organization of this chapter is as follows. In section 4.1 we introduce the principle of **w**aveguide **o**ptical **c**avity **u**ltrasound **d**etector (WOCUD) and discuss how the introduction of a vertical waveguide in the film results in a higher finesse and hence, a higher ultrasound sensitivity. In section 4.2 we describe the fabrication process of these devices. The experimental results of the fabricated device are discussed in section 4.3. We conclude by discussing different methods for further improvement of the device

sensitivity and bandwidth, and integration of WOCUD on the tip of a fiber bundle for dual modality imaging probe.

4.1 Device principles

The device design is based on a step-index polymer waveguide structure between two parallel dielectric mirrors (Figure 4-1 (a)). A narrow linewidth laser beam is used to probe the distance between the mirrors. The characteristic curve of a Fabry-Perot resonator (reflected light intensity versus wavelength) changes due to the variation of the distance between the mirrors. The polymer layer deflects under application of pressure causing the distance between the mirrors to change (Figure 4-1 (b)). Consequently if the wavelength of the interrogation beam is set to a point along the steep slope region of the spectrum, the reflected light intensity varies under the change of the distance between the mirrors (Figure 4-1 (c)). Therefore, variation of the gap between the mirrors due to an applied acoustic pressure modulates the reflected light intensity.

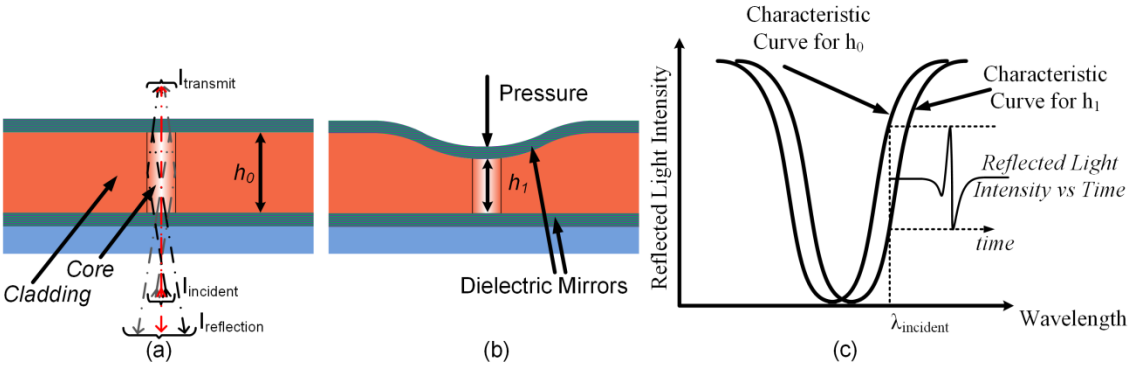

Figure 4-1. (a) Optics of the waveguide optical cavity ultrasound detector (WOCUD). (b) An external pressure wave changes the cavity length. (c) The variation of the cavity length causing a shift in the characteristic curve and modulates the reflected intensity.

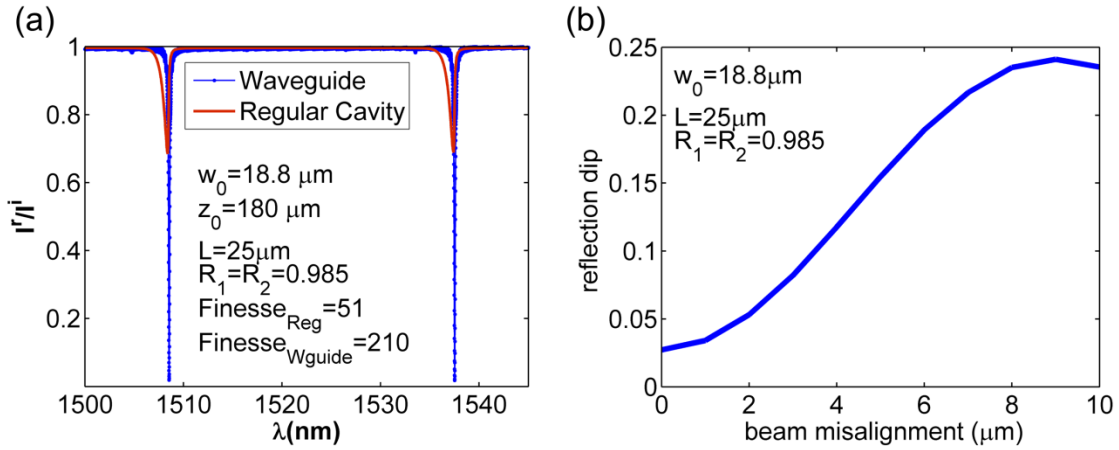

Figure 4-2. (a) Comparison of the characteristic curves in a non-waveguide and a waveguide Fabry-Perot resonator (b) effect of the misalignment of the beam and optical cavity.

The finesse of an optical resonator can be defined as the number of light oscillations between two mirrors at the free space wavelength (λ) before its energy decays by a factor of $e^{-2\pi}$ [62]. The optical path required to achieve this finesse is $2nL\mathcal{F}$ where n, L, $\mathcal{F}$ are the effective refractive index of the cavity, the length of the cavity, and the finesse respectively. The unfolded equivalent models of wave propagation inside cavities with and without waveguide are shown in Figure 3.2 (a) and (b). Diffraction causes energy to leak out of the resonator (Figure 3.2 (a)). The farther the light propagates, the greater the amount of energy that is lost from the cavity. Therefore, as one tries to create cavities with higher finesse and Q-factors, the required optical pathlength increases causing a more significant diffraction effect. Subsequently, for the Gaussian-beam Fabry-Perot resonator without a waveguide, increasing both the cavity length and mirror reflectivity causes the cavity finesse to drastically deviate from the plane wave predicted value. The reason to the deviation from the plane wave cavity can be traced to the variation of the wave-front amplitude and phase profile during propagation resulting in a phase mismatch

of successive reflections. The effects of diffraction can be eliminated, however, if the light passes through a waveguide between the two mirrors which preserves the wave-front amplitude and phase profile (Figure 3.2 (b)). A waveguide inside the cavity can be created in the cavity by inducing a small refractive index modulation to the cavity.

Using mode decomposition analysis, the characteristic curve of the resonator with and without waveguide can be calculated. Figure 4-2 (a) shows the reflected light intensity as a function of the incident wavelength for a Gaussian wave inside the waveguide and non-waveguide etalon. The graph corresponds to a beam waist radius (w_0) of 9.4 μm, which is the approximate value for our actual beam size; the reflectivities of the mirrors (R_1, and R_2) are set to be 0.985; the radius of the core (a) is 10 μm; and the cavity length (L) is 25 μm. Core (n_1) and cladding (n_2) refractive indices are 1.6 and 1.53 respectively. The Rayleigh range (z_0) of the beam is about 180 μm. The dip of the waveguide optical cavity (blue) is sharper than that of non-waveguide cavity (red) and has a four-fold higher finesse. The value of the finesse in the case of the waveguide is exactly the same as the regular Fabry-Perot resonator interrogated by a plane wave. In the case of a Gaussian beam only six out of the first 32 modes have nonzero contribution. Among these six modes 96% of the light is coupled to the first mode (LP_{01}). The effect of misaligning the beam to the center of the cavity is presented in **Error! Reference source not found.**Figure 4-2 (b). The dip amplitude is decreased as the beam moves away from the center of the cavity due to lower coupling of light to the principle mode. The beam

misalignment does not affect the finesse of the device. However, coupling of less light to the main optical mode decreases the signal to noise ratio of the detector.

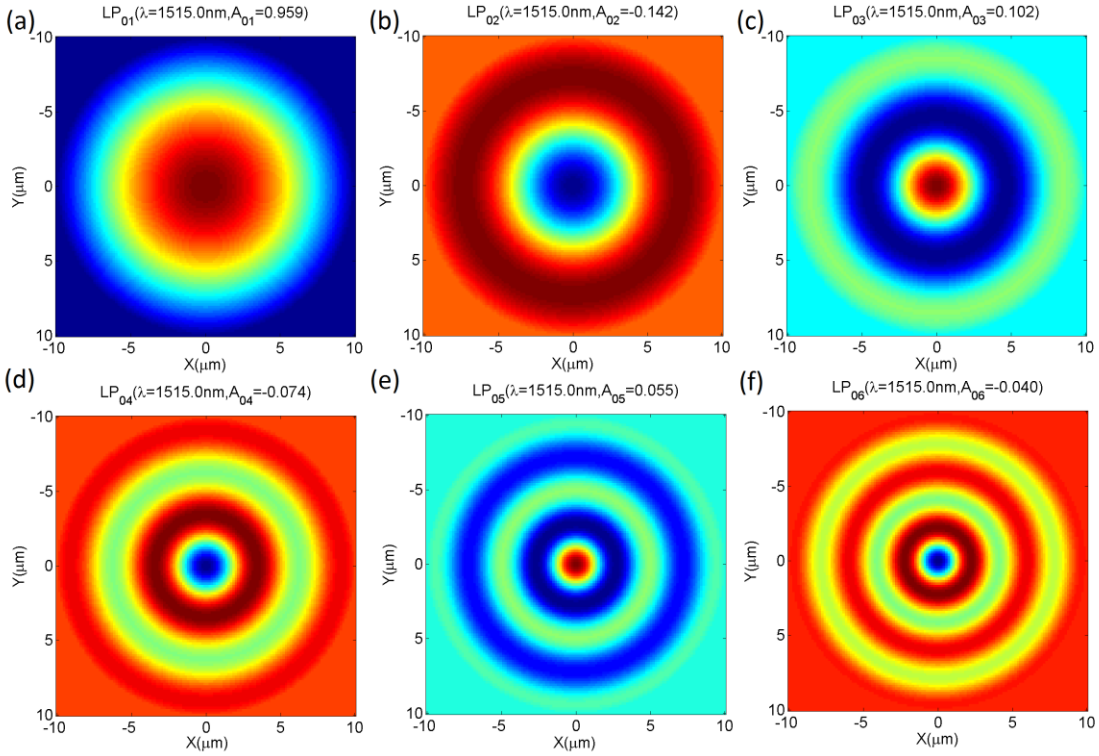

Figure 4-3. (a-f) first 6 non-zero modes and their participation factor.

By eliminating diffraction loss the resonator finesse and Q-factor are only limited by material absorption either in the cavity medium or in the mirror material. We have not explicitly considered the diffraction of light inside the layers of the dielectric Bragg reflector. However, for very high reflectivity mirrors this diffraction might slightly decrease the finesse of the cavity and might shift its resonance frequency as well [64]. From Figure 4-3 (a), we can identify the excitation of some other modes; however, these modes are not as significant as the first mode. Although the higher modes do not affect the finesse of the system they can be removed by having the normalized frequency

($V=2\pi a(n_1^2-n_2^2)^{1/2}/\lambda$) below 2.405 [63]. In this case, the cavity only supports the fundamental mode (LP_{01}). As an example, a waveguide with a refractive index change of 0.003 in a 4 μm radius cavity supports single-mode propagation of light for wavelengths longer than 1000 nm.

4.2 Fabrication

The fabricated device consists of two dielectric Bragg mirrors with a 25 μm polymer layer. The WOCUD fabrication procedure is presented in Figure 4-4. First, the bottom mirror is deposited on a Borofloat glass wafer (step 1). This mirror consists of eight quarter-wavelength layers of titanium dioxide (n= 2.19) and seven quarter-wavelength layers of silicon dioxide (n = 1.46). Both refractive indices were measured using an ellipsometer at the wavelength of 632.8 nm. The deviation of the refractive index of TiO_2 from its expected value (n=2.58) [67] is probably because of trapping of nanoscale voids in the film. However, these voids did not affect the quality of the mirror. For 1550 nm light, the refractive indexes of TiO_2 and SiO_2 are expected to be lower by about 5.9% [67] and 1.2% [68], respectively. Although the mirrors are designed to have their highest reflectivities at 1550 nm, actual peak reflectivity might shift due to the variations of the refractive indices. The layers were deposited using e-beam evaporation (Varian e-beam evaporator, model# 3118, CHA industeries). The oxygen pressure in the chamber during SiO_2 deposition is about 1.4×10^{-5} Torr. The Oxygen line is switched off during the TiO_2 deposition and the chamber pressure is kept below 6.5×10^{-6} Torr. *If the pressure inside the chamber during the deposition increases beyond 3.0×10^{-5} Torr there might be a*

variation from the film thickness expected value. The fabricated dielectric Brag reflector has more than 98% C-Band NIR reflectance. The recipes for deposition of TiO_2 and SiO_2 using Varian are presented in

Table 4-1and Table 4-2 respectively.

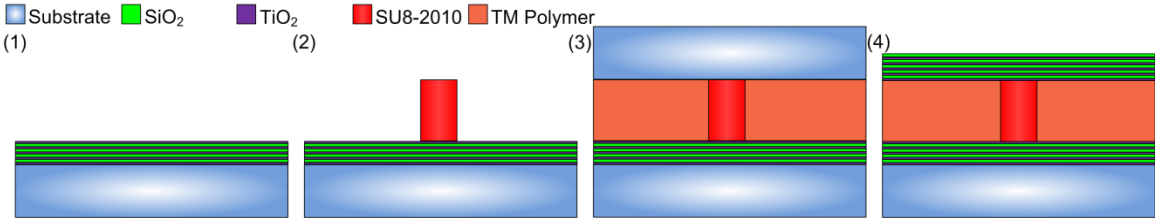

Figure 4-4. Fabrication process of WOCUD: (1) The Bragg reflector is deposited onto the substrate. (2) The SU-8 core of the waveguide is deposited on the mirror. (3) A glass slide is placed on top of the SU-8 pillar and the space between the glass and the reflector is filled with low-index polymer. (4) The second Bragg reflector is deposited.

Next, 25 µm of SU-8 2010 is spun and patterned on the deposited mirror (step 2). The patterning was designed to create an array of circular pillars having different diameters in a range between 10 to 35 µm. These SU-8 (n = 1.57) pillars will form the cores of the waveguides. In step 3, the SU-8 pillars are capped by a glass slide to create the resonator cladding layer. Then, the gap between the glass slide and the bottom mirror is filled with a photopolymer with a refractive index of 1.53. To prevent adhesion of the cladding photopolymer layer to the glass slide, which will be removed later, the glass slide is coated with the hydrophobic surfactant Rain-x®. After filling of the gap using a thiol-ene/methacrylate photopolymer (TM Polymer) [66], the liquid resin is exposed with UV from the glass slide side. After curing the cladding photopolymer, the glass slide can be easily released because of the previous hydrophobic surface treatment. Finally, the front Bragg reflector, which consists of eight bilayers of TiO_2-SiO_2, is deposited on the

polymer layer (step 4). The TiO_2-SiO_2 bilayers have the same thickness and optical properties as the bilayers of the bottom mirror. Figure 4-5 shows the microscope image of the array of the WOCUDs.

Table 4-1. TiO_2 deposition recipe for Varian e-beam evaporator.

Rise time:	0.5 min	Soak1 power:	2%	T1:	2.133 kÅ
Soak 1 time:	0.5 min	Soak2 power:	10%	T2:	0 kÅ
Soak 2 time:	1 min	Max power:	40%	Density:	4.26 g/cm^3
Rate:	1 Å/s	Idle power:	0	Z-ratio	0.4
Tooling:	250%	Gain:	5	Src/Snsr	1/1

Table 4-2. SiO_2 deposition recipe for Varian e-beam evaporator.

Rise time:	0.5 min	Soak1 power:	2%	T1:	3.842 kÅ
Soak 1 time:	0.5 min	Soak2 power:	2%	T2:	0 kÅ
Soak 2 time:	0.5 min	Max power:	12%	Density:	2.65 g/cm^3
Rate:	4 Å/s	Idle power:	0	Z-ratio	1.0
Tooling:	300%	Gain:	2	Src/Snsr	1/1

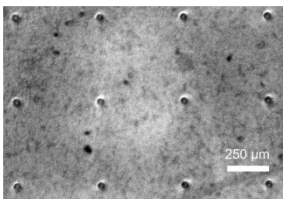

Figure 4-5. Microscope image of the fabricated array of the WOCUDs.

4.3 Experimental results

To test a cavity with a 20 µm diameter core size and a 25 µm thickness, we use the experimental set-up shown in Figure 4-6 (a). The wafer is attached to a tank and immersed in water. Light from an infrared laser source is coupled to the cavity using a collimator, a polarized beam splitter, a λ/4 waveplate, and a lens. Linearly polarized light

from a continuous near infrared (NIR) tunable laser source (8168F, Agilent HP) is transmitted to the collimator through a single-mode fiber with mode field diameter of 10.5 μm. The linearly polarized collimated beam is reflected by 90° by the polarizing beam splitter. The λ/4 waveplate is used to change the linear polarization into circular polarization. Using the lens, this circularly polarized IR probing beam is focused to a specific cavity element in the wafer (a single wafer typically holds a large number of elements of different sizes and shapes).

To locate and visualize the specific cavity from the top, the IR light source is replaced by a red light source and a CCD camera (1/2" CCD, XC-75, Sony) is used to image the device.. Before filling the tank with water, the light source is switched back to the IR laser and the IR camera (1/2" CCD, Cat#56-567, Edmund Optics) is used to finely align the IR probing beam with the center of the selected cavity. With our arrangement of the lens and collimator, the spot size of the focused beam is approximately 19 μm. The polarization of the light changes handedness upon reflection, resulting in a perpendicular linear polarization at the beamsplitter. The beam passes through the beamsplitter and is detected by a fast-response photodetector or a power meter. To find the resonance wavelength of the optical cavity, the NIR wavelength is scanned from 1518 nm to 1530 nm. The reflected light intensity is recorded using an optical power meter (PM100 optical power meter with S122B Germanium Sensor, Thorlabs) and the results are presented in Figure 4-6 (b). The finesse of the waveguide Fabry-Perot resonator is approximately 200

which is about 5 times higher than the measured non-waveguide area on the same wafer. The free spectral range of this device is about 31 nm.

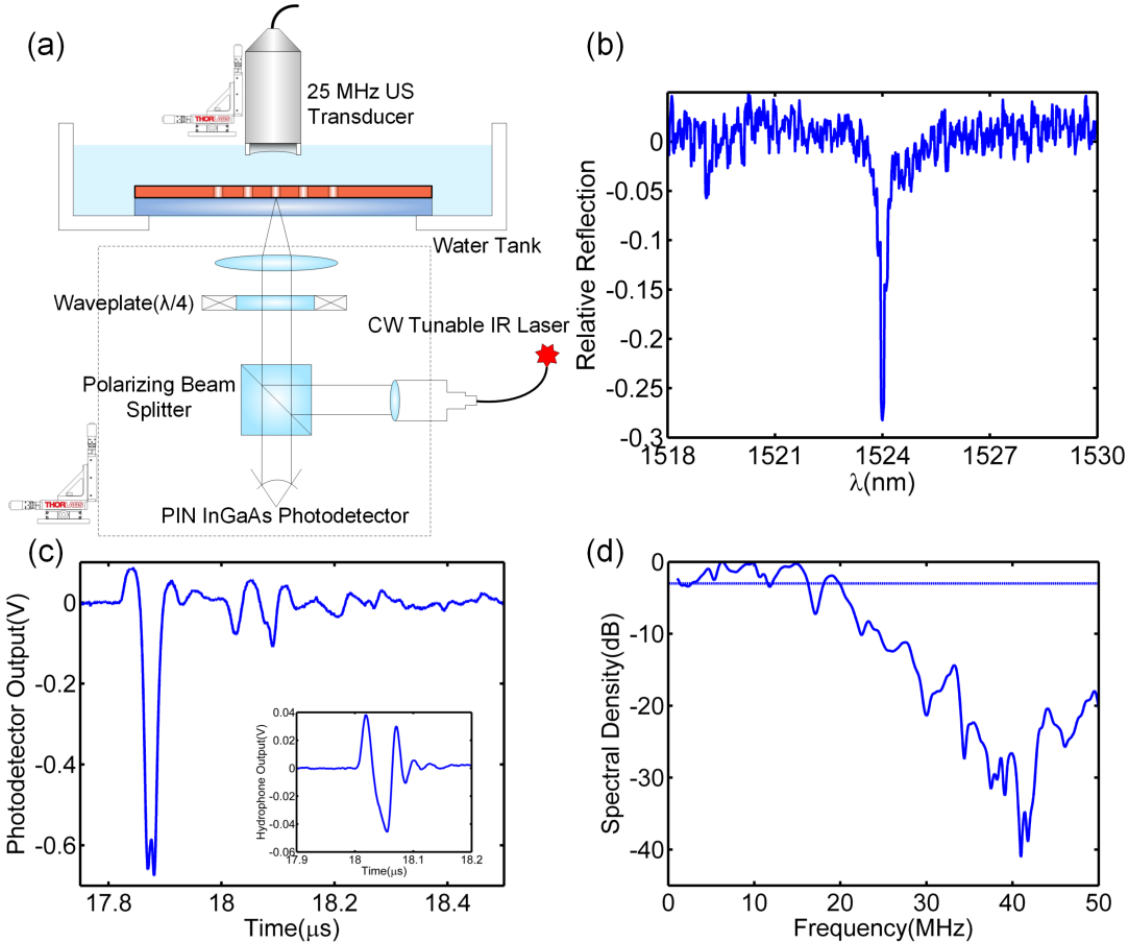

Figure 4-6. (a) The experimental setup used to find the optical and ultrasound characteristics of the device. (b) The characteristic reflection spectrum curve of the tested device. (c) The variation of reflected light intensity from the WOCUD in **response** to the ultrasound pulse. This inset shows the calibrated 60 MHz hydrophone output in response to the same pulse. (d) The frequency spectrum of the WOCUD reflected light intensity and the -3 dB line.

After finding the optical resonance, the laser is tuned to a wavelength corresponding to the region of highest slope on the resonance curve. The optical power meter is replaced with a PIN InGaAs amplified photodetector (818-BB-30A, Newport) which has a short response time for high-frequency optical signal recording. A focused ultrasound

transducer (25 MHz, f = 1", active area = 0.5", V324, Panametrics-NDT) is placed in the water tank above the device. The ultrasound transducer is adjusted so that the cavity is positioned at its focal point. The ultrasound transducer is driven by a short pulse using ultrasound pulser/receiver (DPR 300 pulser/receiver, JSR Ultrasonics). The photodector signal is recorded by a digital oscilloscope (LC584AL, LeCroy). The signal is presented in Figure 4-6 (c).

Various sources contribute to noise in our system. Fluctuation in the intensity and phase of the laser are induced by the laser source. However, in the current setup, these noise sources are negligible because the laser source has a narrow linewidth (100 kHz) and a relatively high signal-to-source spontaneous emission ratio (45 dB/nm). Shot noise, Johnson noise, and the built-in noise of the amplified photodetector are the primary sources found in the optical signal [63]. Considering all noise mechanisms of the photodetector and its built-in amplifier, the noise equivalent power of the detector is about 30 $pW/Hz^{1/2}$, which is the dominant noise source in our system. The other source of noise in the system is the oscilloscope quantization noise which can be neglected in comparison to the photodetector-built-in amplifier noise.

The noise equivalent pressure (NEP) is defined as the acoustic pressure which provides a signal-to-noise ratio of 1. In a preliminary measurement a calibrated hydrophone (model HGL-0085, ONDA Corp., Sunnyvale, CA) was used to measure the peak acoustic pressure at the focal point of the ultrasound transducer using the same pulser settings as later used to test the device. The peak pressure was found to be 852

kPa. Based on this measurement, the NEP of the device at a bandwidth of 28 MHz was calculated to be 178 Pa or 0.03 Pa/Hz$^{1/2}$. The noise level used in estimating the NEP was calculated as the mean square root of the noise signal (extracted before the main signal arrival time at 15 μs) after band-pass filtering from 2-30 MHz. The current device NEP is 20 folds higher than our previous device NEP which was 0.61 Pa/Hz$^{1/2}$ [69]. This improvement of the NEP is due to the application of the waveguide Fabry-Perot resonator and the increase of the thickness of the device.

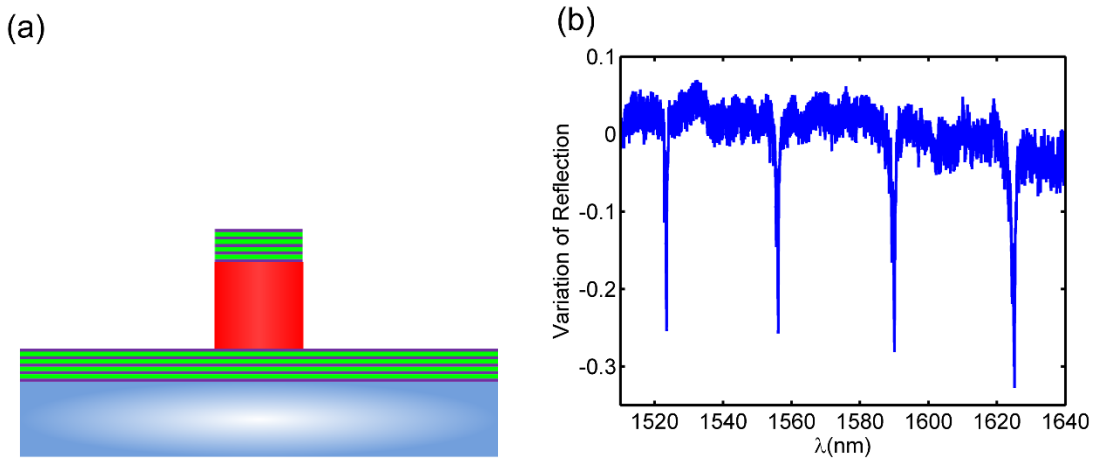

Figure 4-7. (a) Schematic of patterned WOCUD, (b) characteristic curve of the patterned WOCUD.

The response of the device (Figure 4-6 (c)) shows an initial peak that is of high-amplitude with short-period, followed by a smaller amplitude oscillation. The former can be attributed to the direct arrival of a pressure pulse from the transducer. The oscillation following the main dip in the received signal is due to the back reflection from the bottom side of 500 μm Borofloat wafer (reflection traveling time = 183 ns, corresponding frequency = 5.46 MHz). The dip of the main signal consists of two close dips which are 12 ns away from each other. This dual dip can be due to the internal reflection of the

ultrasound pulse in the cavity. The inset in Figure 4-6 (c) shows the calibrated 60 MHz hydrophone output in response to the same pulse. The frequency spectrum of the recorded signal from the photodetector is presented in Figure 4-6 (d).

4.4 Patterned WOCUD with conformal mirrors

In case the refractive index of the immersion medium of the WOCUD is higher than the core, the immersion medium can work as a cladding and the design similar to Figure 4-7 (a) can be applied. The fabricated device has been tested optically and the characteristic curve is presented in Figure 4-7 (b). The finesse of the same order as the all polymer core and cladding has been achieved (e.g. finesse of 146 for Figure 4-7 (b)). The front mirror can work as cladding in case the mirror deposition process has a good coverage on the core side-walls. Because the side wall coverage of the e-beam evaporation process is not reliable it might be better to cover the side walls with a low refractive index polymer in a process similar to the step 3 of Figure 4-4. Adding a cladding after deposition of the second mirror provides more options to choose for cladding layer since there is no need for stress compatibility of the cladding layer and the second mirror. Therefore, softer polymers (e.g. NOA 84) can be selected as a cladding layer. Using a free core or a softer material as a cladding improves the mechanical characteristics of the WOCUD.

ANSYS has been used to mechanically model the free core and compare its deflection with core embedded in large slab of a material with the same mechanical properties. The core diameter, thickness, module of elasticity, and Poisson ratio are considered as 20 μm, 10 μm, 4 GPa, 0.22 respectively. Figure 4-8 show the core

deflection in the thickness direction under pressure of 1 Pa on the core top surface, (a) for the free core, and (b) for the core embedded in the slab. As we can see in Figure 4-8 (c) the maximum, minimum, and the average displacement of the top surface for the free core are 2.51×10^{-9}, 2.17×10^{-9}, and 2.4×10^{-9} μm respectively. The maximum, minimum, and the average displacement of the top surface for the core embedded slab are 2.18×10^{-9}, 0.51×10^{-9}, and 1.81×10^{-9} μm respectively. As we can see the average displacement of the free core (patterned WOCUD) is about 30% higher than the core embedded in slab. Hence, the device sensitivity can be increased by 30% for the patterned WOCUD.

If a thinner top mirror is required a gold mirror with reflectivity of more than 98% can be utilized as the front mirror to avoid any acoustical impedence mismatch between the device and the imaging medium. The gold layer thickness can be increased to 200 nm. This design can be applied for the patterned WOCUD as well since there is no need for the cladding utilizing the sputtering machine for gold conformal deposition. For the case of the WOCUD on wafer, there might be some issues for alignment of the focused light and the optical cavity. This problem can be solved by adding some markers to the gold layer. The first mirror cannot be replaced with the gold mirror since for thick gold mirror, none reflected light mostly is absorbed instead of transmitting through the mirror and coupling to the optical cavity.

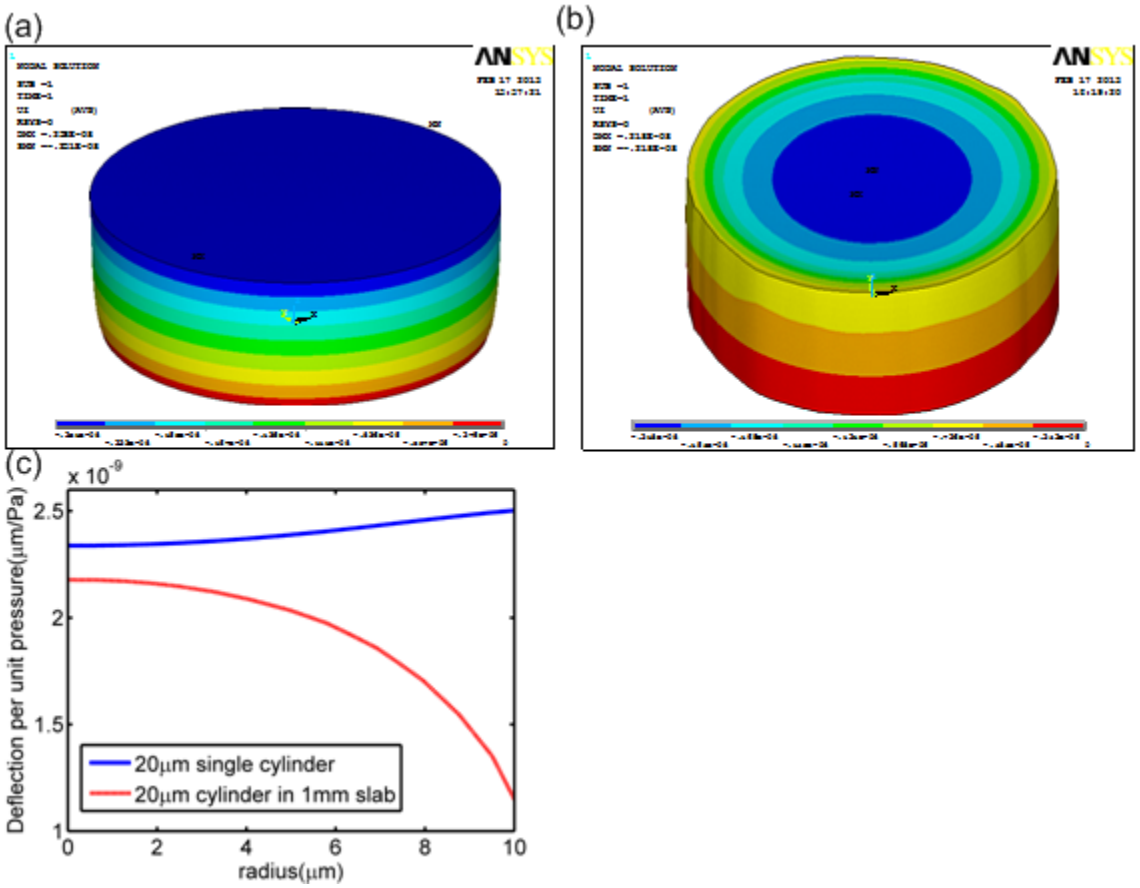

Figure 4-8. (a) Deflection in the thickness direction of the SU-8 cylinder with thickness of 10 μm and diameter of 20 μm under pressure of 1 Pa. (b) Deflection of the slab of SU-8 with thickness of 10 μm (only 20 μm of it under pressure). (c) Comparing the deflection of (a) and (b).

4.5 Measurement system noise analysis

As we discussed in previous section, there are different noise sources in our detection system. These noises include photodetector thermal (Johnson) and shot noises, laser linewidth and power noises, noises from built-in amplifier of the photodetector, oscilloscope quantization noise, and mechanical vibrations of the experimental set-up.

Shot noise (or generation-recombination noise in photoconductive detectors), is attributed to the random generation or emission of electrons in the interaction with a

radiation field. Even at zero temperature where thermal agitation or generation of carriers is negligible, the shot noise exists. In this case it results from the randomness of the carriers generations by the very signal that is measured [50]. The shot noise variance ($\sigma_s(\nu)$) or equivalent noise generator ($\overline{i\,^2_N}(\nu)$) at frequency of ν can be calculated using [63, 70],

$$\sigma_s^2(\nu) = \overline{i\,^2_N}(\nu) = 2q\bar{I}\Delta\nu \qquad \text{Eq. 4-1}$$

Table 4-3. The Newport 818-BB-30A photodetector [71].

Model	818-BB-30A
Detector Material	InGaAs
Wavelength Range	1000-1600 nm
NEP	<30 pW/√Hz
Detector Type	Semiconductor, biased
Rise Time	<400ps
Fall Time	<400 ps
Output Connector	BNC
Impedance, Load	50 Ω
Cut Off Frequency	>1.5 GHz
Saturation Current of the Sensor	5.0 mA
Saturation Current with Amplifier	1.3 mA
Bias Voltage	24 V
Acceptance Angle	20°
Amplified	Yes
Active Diameter	100 µm
Responsivity of the Sensor	0.8 A/W @ 1300 nm
Responsivity with Amplifier	900 V/W @ 1300 nm
Dark Current	<1 nA
Junction Capacitance	<0.75 pF
Reverse Breakdown	25 V
Maximum Linear Rating	1.3 V peak

where q, $\bar{I}$, and $\Delta\nu$ are carrier charge, average current, and effective noise bandwidth respectively. The responsivity of the applied photodetector is 0.8 A/W at 1300 nm and about 0.95 at 1550 nm and the maximum power of the utilized laser is about 4 mW.

Therefore, the average current and the shot noise over 28 MHz are 3.8 mA, and 34×10^{-15} A^2 respectively.

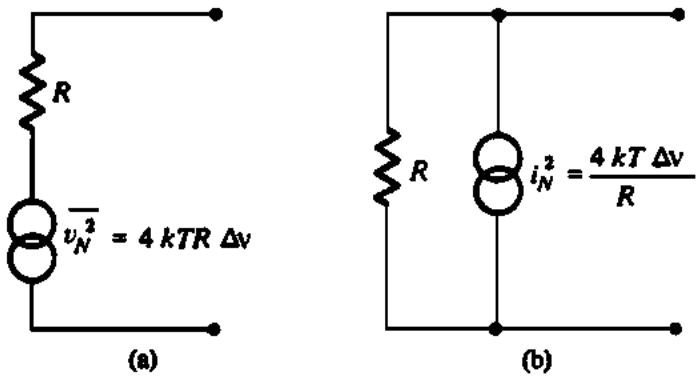

Figure 4-9. (a) Voltage and (b) current noise equivalent circuits [50].

Johnson noise, Nyquist noise, or thermal noise explains the variations in the voltage across a dissipative circuit element. These variations are due to the thermal motion of the charge carriers. The word carriers has been used instead of electrons to include cases of conduction by ions or holes in semiconductors. The charge neutrality of an electrical resistance is satisfied considering the whole volume, but locally the random thermal motion of the carriers sets up fluctuating charge gradients and, therefore, a fluctuating (ac) voltage. A noise generator in series with resistance (R) with mean square voltage amplitude [50]

$$\overline{v_N^2}(\nu) = \frac{4h\nu R\Delta\nu}{e^{h\nu/k_BT}-1} \underset{k_BT \gg h\nu}{\approx} 4k_BTR\Delta\nu \qquad \text{Eq. 4-2}$$

or a noise current generator of mean square value [50]

$$\overline{i_N^2}(\nu) = \frac{4h\nu\Delta\nu}{e^{h\nu/k_BT}-1} \underset{k_BT \gg h\nu}{\approx} \frac{4k_BT\Delta\nu}{R} \qquad \text{Eq. 4-3}$$

in parallel with R can be considered as to build a model for the shot noise. The noise representation of the resistor are presented in Figure 4-9. Where in the above equations, h is Planck constant, k_B is Boltzmann constant, and T is the absolute temperature. Considering working temperature of 296 K, and load resistance of 50 Ω, the Johnson noise of our system is about 9.15×10^{-15} A^2 over the bandwidth of 28 MHz. The **electrical amplifier** enhances the **thermal noise** generated in the photodetector. A simple approach accounts for amplifier noise by introducing the total amplifier noise figure (F_{total}), and the thermal noise equation can be modified to [70],

$$\overline{i_N^2}(\nu) = \frac{4k_B T F_{total} \Delta\nu}{R} \qquad \text{Eq. 4-4}$$

Physically, F_{total} represents the factor by which thermal noise is enhanced by various resistors used in pre- and main amplifier and can be calculated as [72],

$$F_{tot} = F_1 + \sum_{i=1}^{n} \frac{F_i - 1}{G_{i-1}} \qquad \text{Eq. 4-5}$$

Table 4-4. The Agilent HP 8168F continuous wave tunable laser specifications [73].

Model	8168F
Wavelength range	1508-1640 nm
Absolute wavelength accuracy, typical	±0.1 nm
Relative wavelength accuracy	±0.035 nm, typ. ± 0.001 nm
Wavelength resolution	0.001 nm
Wavelength stability	<±100 MHz
Wavelength repeatability	±0.035 nm, typ. ± 0.001 nm
Linewidth (typical) broadened (effective, typical)	100 kHz 50-500 MHz
Signal to source spontaneous emission ratio	>45 dB/1 nm
Signal suppression ratio	>50 dB
Maximum output power (peak, typical)	+7 dBm
Relative intensity noise (RIN)	<-145 dB/Hz
Built-in Amplifier Gain	~26 dB

where F_i and G_i are the noise figure and amplifier gain power of the ith amplifier. We do not have any information on the noise figure of the applied photodetector. The amplifier noise figure is assumed 2.08 [72] since we did not have any information about it. By this consideration, the thermal noise should be modified to 19×10^{-15} A^2.

The semiconductor laser output exhibits fluctuations in its intensity, phase, and frequency. The **two major noise mechanisms of the laser** are spontaneous emission and electron-hole recombination. Spontaneous emission is the fundamental noise source in semiconductor lasers. Each spontaneously emitted photon adds a small component to coherent field whose phase is random and thus perturbs both amplitude and phase in a random manner [70]. The intensity-autocorrelation function is defined as

$$C_{pp}(\tau) = \lim_{T\to\infty} \frac{1}{T} \frac{\int_{-T}^{+T} \delta P(t)\delta P(t+\tau)dt}{\bar{P}^2} \qquad \text{Eq. 4-6}$$

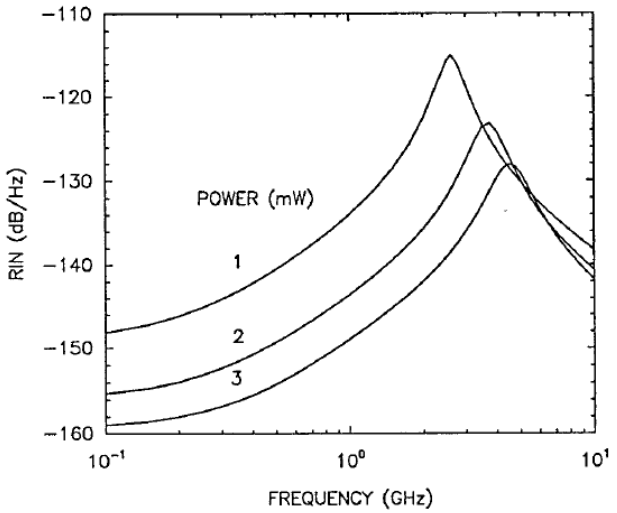

Figure 4-10. RIN spectra at several power levels for typical 1.55 μm semiconductor laser [70].

where $\bar{P} \equiv \lim_{T\to\infty} \frac{1}{T}\int_{-T}^{T} P(t)dt$ is the average value and $\delta P = P - \bar{P}$ represents a small fluctuation. The Fourier transform of $C_{pp}(\tau)$ is known as the relative-intensity-noise (RIN) spectrum and is given by

$$RIN\ (f) = \int_{-\infty}^{+\infty} C_{pp}(t)\, exp(-2\pi i f t)\, dt \qquad \text{Eq. 4-7}$$

There are more details on theoretical calculation of the RIN in Chapter 3 of [70]. Experimentally, the relative intensity noise (RIN) can be found by dividing square of the root mean square of optical power amplitude by the measurement bandwidth and square of the average power, expressed in dB/Hz. From Table 4-4, the maximum RIN of the utilized laser is -145 dB/Hz which is determined in the frequency range of 0.1-6 GHz [73]. Figure 4-10 shows the calculated RIN spectra at several power levels for a typical 1.55 μm InGaAsP. The RIN significantly increases near the relaxation frequency and decreases rapidly moving away from the relaxation frequency [70]. As we can see in Figure 4-10 RIN, decreases by more than -30 dB in 2-30 MHz which we measure the variation of the light intensity. Therefore, considering the maximum RIN presented in Table 4-4 the RIN in our device frequency range should be around -175 dB/Hz. Depending on the applied optical power, this RIN gives us the noise level of $8 \times 10^{-17} - 1.3 \times 10^{-15}$ A^2 in our device frequency range. This value is 3% of the noise from the combination of shot noise and Johnson noise (without amplifier consideration) of the photodetector. Since the utilized laser has a linewidth of 50-100 kHz which is exceedingly narrower than our best Fabry-Perot resonator with bandwidth of about 1.25

GHz (presented in the previous chapter) we can neglect the noises due to the device linewidth.

The other source of noise in the system is the **oscilloscope quantization noise** which can be neglected in comparison to the photodetector noise. Because of the frequency range which our device is working we can neglect the noises from the **experimental set-up mechanical vibrations**. Shot noise, Johnson noise, and the built-in noise of the amplified photodetector are the primary noise sources found in the optical signal.

4.6 Conclusion

The WOCUD, a modified Fabry-Perot thin-film etalon having a waveguide structure, has been developed for high-frequency ultrasound detection applications. The waveguide inside the cavity confines light propagation and creates a phase-front perfectly matched to the flat mirror geometry. This improves the sharpness of the resonance peak by one or more orders of magnitude thereby increasing the finesse. This method also keeps the coupled light energy confined to a smaller volume increasing the sensitivity. The measured finesse and detection sensitivity of the WOCUD device are as follows: finesse value of 200 and noise equivalent pressure of 178 Pa or 0.03 $Pa/Hz^{1/2}$ over a bandwidth of 28 MHz.

The thickness of the mirrors should be considered in the design of future devices with even higher sensitivity since the acoustic impedance mismatch between the interface of the ambient media and the device front surface becomes more significant as the mirror

thickness increases. This effect is negligible in our design since the front mirror thickness is only about 3.7 μm. However, for higher frequency applications it might become more significant. In these cases reducing the mirror thickness might be achieved by working at shorter optical wavelengths.

The new WOCUD design has higher sensitivity than other optical ultrasound detector designs that were studied in our lab such as the flat polymer etalon [28] and the air-cavity **o**ptical **m**icromachined **u**ltrasound **t**ransducer (OMUT) [74]. Moreover, it can be directly fabricated on the tip of a fiber for fiber-delivered imaging probes. The design also allows for integration of ultrasound transmission functionality making the device an all-optical ultrasound transmitter/receiver. The transmitter function can be integrated with the detectors by adding a photo-absorptive layer underneath the receivers similar to the design presented in Chapter 2. In this design a polyimide layer was used for high optical absorption in the UV range (355 nm) and high transmission in the visible and IR range. A coherent multimode optical fiber bundle, similar in construction to imaging bundles used in endoscopic applications, can be utilized for array of our optical transducer. By appropriately designing the dielectric mirrors, a region of high transmission (e.g between 650 to 1000 nm) could be formed for transmitting light through the device for other imaging modalities such as photoacoustic imaging.

The key feature of this design – miniaturization – makes it an ideal technology for medical applications such as real-time guidance of cardiovascular interventions, laparoscopic surgery, and deep-brain electrode implantation. Another added value of this

technology is the facilitation of pulse-echo ultrasound imaging and PAI in a single device. Combining ultrasound imaging and PAI provides a range of possibilities for the design of multi-modality, functional, and molecular imaging systems for medical diagnosis and therapy guidance. Developing OMUT technology as an all-optical, transparent, ultrasound transducer will also enable a range of new tools in different fields of science and technology due to its MRI compatibility, immunity to radio frequency interference, and potential for integrating with other imaging modalities.

Chapter 5. Conclusion and future directions

5.1 Summary of the works

First air cavity optical resonators with a top polymer membrane were demonstrated for detection of high frequency ultrasound signals. In order to design the top membrane, a mechanical model that includes additive mass and damping of front water loading on the membrane was applied. For verification of the mechanical model with the experimental data, simple expressions for optical and mechanical sensitivity of the cavity detector were derived. Subsequently, the experimental test results were compared with the predictions of the theoretical model. A good agreement was found between the measured sensitivity and the model prediction. A device of 60 μm diameter and 8 μm membrane thickness was tested using a 25 MHz ultrasonic transducer. Although the device dimensions were not optimized for this frequency (regarding its sensitivity) the primary peak in the signal was in good agreement with measurement of the same signal with a calibrated hydrophone. However, series of undesired low-frequency oscillations following the main signal is

observed. These are probably caused by internal acoustic reflections in the Pyrex substrate. This effect can be removed using a thicker substrate or utilizing a wedge substrate which does not reflect back the ultrasound pulse. It can also be significantly reduced by employing a dense array of elements, thus preventing acoustic radiation from penetrating into the substrate. The noise equivalent pressure of the device is 9.25 kPa over the bandwidth of 28 MHz.

After observing insufficient improvement in mechanical modification of the Fabry-Perot resonator ultrasound detector, a new method is presented to improve the detector optical properties. Utilizing this method the Q-factor and finesse of polymeric Fabry-Perot resonators is significantly improved. By creating a waveguide inside the cavity, a confined mode propagates in the cavity having a phase-front perfectly matched to the flat mirror geometry. This improves the sharpness of the resonance peak by one or more orders of magnitude. This method also keeps the coupled light energy confined to a smaller volume, which is extremely important in applying the technology to miniaturized ultrasound imaging devices.

One of the major advantages of this device is its compatibility with imaging fiber bundles. Large arrays of several thousands of high Q-factor resonators can be fabricated on the tip of a mirror-coated optical fiber bundle without any need for alignment or a complicated fabrication process. In next chapters, we apply this device to create high-resolution, miniaturized 3D ultrasound imaging probes in medical imaging applications.

Next, the WOCUD, based on a modified Fabry-Perot thin-film etalon having a waveguide structure, has been developed for high-frequency ultrasound detection applications. As we mentioned earlier, the waveguide inside the cavity confines light propagation and creates a phase-front perfectly matched to the flat mirror geometry. This improves the sharpness of the resonance peak by one or more orders of magnitude thereby increasing the finesse. This method also keeps the coupled light energy confined to a smaller volume increasing the sensitivity. The measured finesse and detection sensitivity of the WOCUD device are as follows: finesse value of 200 and noise equivalent pressure of 178 Pa or 0.03 $Pa/Hz^{1/2}$ over a bandwidth of 28 MHz.

The thickness of the mirrors should be considered in the design of future devices with even higher sensitivity since the acoustic impedance mismatch between the interface of the ambient media and the device front surface becomes more significant as the mirror thickness increases. This effect is negligible in our design since the front mirror thickness is only about 3.7 μm. However, for higher frequency applications it might become more significant. In these cases reducing the mirror thickness might be achieved by working at shorter optical wavelengths.

The new WOCUD design has higher sensitivity than other optical ultrasound detector designs that were studied in our lab such as the flat polymer etalon [28] and the air-cavity **o**ptical **m**icromachined **u**ltrasound **t**ransducer (OMUT) [74]. Moreover, it can be directly fabricated on the tip of a fiber for fiber-delivered imaging probes. Due to the advantage

of this new design over the previous design in the next sections we are just discussed about the improvements and the future works on the WOCUD.

5.2 Improvements in WOCUD

The **measurement system** can be optimized by reducing amount of noise in it and increasing amount of light power. As we mentioned in section 4.4, the photodetector is the major noise source in our system. The photodetector shot noise, Johnson noise, and the noise induced by its built-in amplifier are the noise sources with comparable noise level. Utilizing a photodetector (e.g. 818-BB-35, Newport) with a better noise equivalent power and the proper saturation current reduces the ultrasound detector noise equivalent pressure. The smaller amount of dark current reduces the measurement system noise level and therefore the ultrasound detector with the higher sensitivity can be achieved. Application of a photodetector without any amplifier might decrease the noise equivalent pressure of the ultrasound detector. However, the effects of the wiring noise and oscilloscope quantization error might become more significant in this case. Higher power laser source (e.g. TSL-710, SANTEC) can be utilized with application of a photodetector with a higher current saturation. This increases amount of the signal to noise ratio and therefore the ultrasound detector sensitivity.

The **waveguide optical cavity ultrasound detector** should be optimized optically and mechanically. One of the major advantages of the WOCUD is that the major mechanical and optical parameters are independent and can be optimized separately. The mechanical parameters should be optimized by proper design of the polymer thickness.

Considering material properties of the polymer layer, the thickness of the layer should be selected in a way that the ultrasound detector required bandwidth and highest possible mechanical flexibility are achieved. Since in WOCUD the optical properties of the Fabry-Perot resonator is independent of the polymer layer thickness, the thickness of the layer can be optimized to attain the highest mechanical performance without loss of the optical performance. The device mechanical sensitivity can be increased by application of the softer polymer layer as well. However, the softer material should have stress and thermal compatibility with the stress and temperature induced by the second mirror deposition.

Optical sensitivity, thus the sensitivity of WOCUD can be raised by increasing the reflectivities of mirrors. This can be done by increasing the number of bilayers in the mirror. Increasing the thickness of the mirrors might affect the ultrasound performance of the device but this effect is negligible due to the thin front mirror (second mirror). However, if a thinner front mirror is required a gold mirror with reflectivity of more than 98% can be utilized. This design can be applied for the patterned WOCUD as well since there is no need for the cladding by utilizing the sputtering machine for gold conformal deposition. This design might increase amount of the mechanical deflection by 30%.

The second mirror can be replaced by gold because there is no need for light transmission through it. The thickness of this gold layer can be increased to 200 nm. Because the gold mirror can be made even thinner than the dielectric mirror it might induce less stress on the polymer layer the softer layer can be applied for the cavity medium (e.g. core: NOA89, cladding: NOA84 both from Norland Adhesives). If even

higher reflective mirror is required, the dielectric and metal mirror can be combined. The amount of light coupled to the cavity main mode is determined by the dip amplitude in the reflection characteristic curve of the Fabry-Perot resonator. Therefore, the higher contrast between the dip and off-resonance reflection in the optical characteristics curve provides the higher signal to noise ratio in the ultrasound detector.

The amount of light coupled to the waveguide Fabry-Perot resonator can be optimized by proper design of the core and cladding and guiding of light to them. The highest signal to noise ratio is achievable if the numerical aperture of the waveguide Fabry-Perot resonator is matched with the numerical aperture of the optical element (either lens or optical fiber) utilized to couple the light to the optical resonator. Further improvement of the characteristic curve of the resonator is expected by integrating the cavity onto the tip of an optical fiber. In this way, we expect better coupling due to higher overlap between the fiber modes and the cavity modes. Additionally, higher modes can be eliminated by using a single-mode cavity design. The integration of the device onto the tip of an optical fiber can eliminate the acoustic reflection from the back side of the substrate. This effect can be also removed using a thicker substrate or utilizing a wedge substrate which does not reflect back the ultrasound pulse directly to the cavity.

5.3 Future Direction

To make the device more commercially attractive in comparison with alternative ultrasound transducer technologies, it is essential to integrate ultrasound transmission

functionality to the design. The transmitter elements can be integrated with the receiver elements by adding a photo-absorptive layer underneath the receivers. A coherent multimode optical fiber bundle, similar in construction to imaging bundles used in endoscopic applications, can be used for this application. The distance between the transmitter and receiver can be 10-20 μm and the distance between two neighboring receivers can be 20-40 μm. The proposed all-optical transmitter/receiver device can be utilized for ultrasound and photoacoustic imaging. By appropriately designing the dielectric mirrors, a region of high transmission (e.g between 650 to 1000 nm) could be formed for transmitting light through the device for other imaging modalities such as photoacoustic imaging.

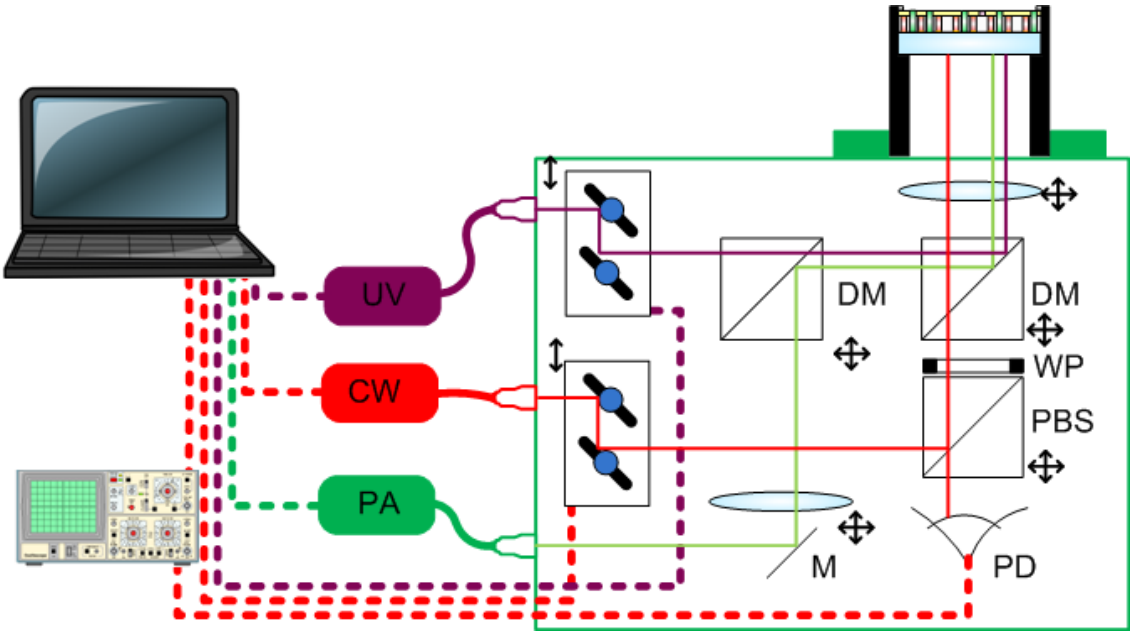

Figure 5-1. Schematic of OMUT based US / PA imaging system. A pulsed laser emitting at 800 nm (PA) delivers photoacoustic excitation pulses. US pulses are generated by a pulsed UV laser (UV) beam. The beam is scanned by a galvo scanner (GS) and focused on the surface of an optical fiber bundle. A CW probing beam is scanned by a second scanner (GS). The reflection signal is collected by a photodetector (PD) and acquired digitally. Dielectric mirrors (DM) combine the laser beams, waveplate (WP) changes the polarization state of IR laser light, and polarizing beam splitter (PBS) separate reflected and transmitted light.

The key feature of this design – miniaturization – makes it an ideal technology for medical applications such as real-time guidance of cardiovascular interventions, laparoscopic surgery, and deep-brain electrode implantation. Another added value of this technology is the facilitation of pulse-echo ultrasound imaging and PAI in a single device. Combining ultrasound imaging and PAI provides a range of possibilities for the design of multi-modality, functional, and molecular imaging systems for medical diagnosis and therapy guidance. Developing OMUT technology as an all-optical, transparent, ultrasound transducer will also enable a range of new tools in different fields of science and technology due to its MRI compatibility, immunity to radio frequency interference, and potential for integrating with other imaging modalities.

The transmitter/receiver array can be tested for its implementation in photoacoustic imaging configuration. The experimental setup is shown in Figure 8. The pulse energy will be set to 10 to 20 mJ and the beam will be expanded to illuminate a spot of 1-2 mm in size. This level of energy fluence is below the maximum permissible skin exposure to laser radiation according to laser safety standard (IEC 60825-1). The focused UV pulse coupled to an optical fiber for ultrasound generation is emitted on the polyimide layer. The UV pulse duration should be 5-10 ns and pulse energy of 8-12 μJ. The OMUT device should be transparent to the photoacoustic laser pulse in most regions to deliver enough light to an imaging target. Imaging experiments is conducted by addressing each receiver element in the array in a serial way (one element at a time) and recording the output signal following a photoacoustic laser pulse excitation. The recording length of

each signal should be about 10 μs to allow acquiring photoacoustic signals generated at a depth of up to 15 mm.

Following a complete array signal acquisition image reconstruction by beam forming algorithm will be performed. Images sliced at different 2D cross-sections of the full 3D field of view will be generated. The images will be studied and analyzed for characterizing the resolution as a function of depth, and the signal-to-noise and signal-to-background characteristics. Final characterization of the dual-modality imaging system should be carried out using tissue sample.

References

[1] S. Logani, H. E. Saltzman, P. Kurnik, H. J. Eisen and G. S. Ledley. Clinical utility of intravascular ultrasound in the assessment of coronary allograft vasculopathy: A review. *J. Interv. Cardiol. 24(1),* pp. 9-14. 2011.

[2] S. E. Nissen and P. Yock. Intravascular ultrasound: Novel pathophysiological insights and current clinical applications. *Circulation 103(4),* pp. 604-616. 2001.

[3] A. F. van der Steen, R. A. Baldewsing, F. Levent Degertekin, S. Emelianov, M. E. Frijlink, Y. Furukawa, D. Goertz, M. Karaman, P. T. Khuri-Yakub, K. Kim, F. Mastik, T. Moriya, O. Oralkan, Y. Saijo, J. A. Schaar, P. W. Serruys, S. Sethuraman, A. Tanaka, H. J. Vos, R. Witte and M. O'Donnell. IVUS beyond the horizon. *EuroIntervention 2(1),* pp. 132-142. 2006.

[4] M. E. Brezinski, G. J. Tearney, N. J. Weissman, S. A. Boppart, B. E. Bouma, M. R. Hee, A. E. Weyman, E. A. Swanson, J. F. Southern and J. G. Fujimoto. Assessing atherosclerotic plaque morphology: Comparison of optical coherence tomography and high frequency intravascular ultrasound. *Heart 77(5),* pp. 397-403. 1997.

[5] J. Li, X. Li, J. Jing, D. Mohar, A. Raney, S. Mahon, M. Brenner, Q. Zhou, P. Patel and K. K. Shung. Integrated intravascular optical coherence tomography (OCT)-ultrasound (US) catheter for characterization of atherosclerotic plaques in vivo. Presented at Engineering in Medicine and Biology Society (EMBC), 2012 Annual International Conference of the IEEE. 2012, .

[6] R. S. Cobbold. *Foundations of Biomedical Ultrasound* 2007.

[7] H. Soh, I. Ladabaum, A. Atalar, C. Quate and B. Khuri-Yakub. Silicon micromachined ultrasonic immersion transducers. *Appl. Phys. Lett. 69(24),* pp. 3674-3676. 1996.

[8] I. Ladabaum, B. Khuri-Yakub and D. Spoliansky. Micromachined ultrasonic transducers: 11.4 MHz transmission in air and more. *Appl. Phys. Lett. 68(1),* pp. 7-9. 1996.

[9] D. N. Stephens, U. T. Truong, A. Nikoozadeh, O. Oralkan, C. H. Seo, J. Cannata, A. Dentinger, K. Thomenius, A. de la Rama, T. Nguyen, F. Lin, P. Khuri-Yakub, A. Mahajan, K. Shivkumar, M. O'Donnell and D. J. Sahn. First in vivo use of a capacitive micromachined ultrasound transducer array-based imaging and ablation catheter. *J. Ultrasound Med. 31(2),* pp. 247-256. 2012.

[10] *http://greman.univ-tours.fr/axis-3/ (Piezoelectric and capacitive micro and nano systems for ultrasonic transducers and energy conversion)*.

[11] *http://web.mit.edu/sunjie/www/ (What does Silicon Nanophotonics Look Like?)*.

[12] V. Govindan and S. Ashkenazi. Bragg waveguide ultrasound detectors. *Ultrasonics, Ferroelectrics and Frequency Control, IEEE Transactions On 59(10),* 2012.

[13] J. Li, A. Taylor, I. Papakonstantinou, E. Zhang and P. Beard. Highly sensitive optical microresonator sensors for photoacoustic imaging. Presented at SPIE BiOS. 2014.

[14] R. Paschotta. *Encyclopedia of Laser Physics and Technology* 2008*1*.

[15] J. Thomson, H. Wickramasinghe and E. Ash. A fabry-perot acoustic surface vibration detector-application to acoustic holography. *J. Phys. D 6(6),* pp. 677. 1973.

[16] P. Beard and T. Mills. Miniature optical fibre ultrasonic hydrophone using a fabry-perot polymer film interferometer. *Electron. Lett. 33(9),* pp. 801-803. 1997.

[17] P. C. Beard, A. M. Hurrell and T. N. Mills. Characterization of a polymer film optical fiber hydrophone for use in the range 1 to 20 MHz: A comparison with PVDF needle and membrane hydrophones. *Ultrasonics, Ferroelectrics and Frequency Control, IEEE Transactions On 47(1),* pp. 256-264. 2000.

[18] C. Sheaff and S. Ashkenazi. A fiber optic optoacoustic ultrasound sensor for photoacoustic endoscopy. Presented at Ultrasonics Symposium (IUS), 2010 IEEE. 2010, .

[19] P. Beard and T. Mills. A 2D optical ultrasound array using a polymer film sensing interferometer. Presented at Ultrasonics Symposium, 2000 IEEE. 2000, .

[20] J. D. Hamilton, T. Buma, M. Spisar and M. O'Donnell. High frequency optoacoustic arrays using etalon detection. *Ultrasonics, Ferroelectrics and Frequency Control, IEEE Transactions On 47(1),* pp. 160-169. 2000.

[21] E. Zhang, J. Laufer, R. Pedley and P. Beard. In vivo high-resolution 3D photoacoustic imaging of superficial vascular anatomy. *Phys. Med. Biol. 54(4),* pp. 1035. 2009.

[22] S. Ashkenazi, C. Chao, L. J. Guo and M. O'donnell. Ultrasound detection using polymer microring optical resonator. *Appl. Phys. Lett. 85(22),* pp. 5418-5420. 2004.

[23] C. Chao, S. Ashkenazi, S. Huang, M. O'Donnell and L. J. Guo. High-frequency ultrasound sensors using polymer microring resonators. *Ultrasonics, Ferroelectrics and Frequency Control, IEEE Transactions On 54(5),* pp. 957-965. 2007.

[24] T. Ling, S. Chen and L. J. Guo. Fabrication and characterization of high Q polymer micro-ring resonator and its application as a sensitive ultrasonic detector. *Optics Express 19(2),* pp. 861-869. 2011.

[25] V. Govindan and S. Ashkenazi. Bragg waveguide ultrasound detectors. *Ultrasonics, Ferroelectrics and Frequency Control, IEEE Transactions On 59(10),* 2012.

[26] A. Rosenthal, V. Ntziachristos and D. Razansky. Acoustic inversion in optoacoustic tomography: A review. *Current Medical Imaging Reviews 9(4),* pp. 318. 2013.

[27] Y. Hou, J. Kim, S. Ashkenazi, S. Huang, L. J. Guo and M. O'Donnell. Broadband all-optical ultrasound transducers. *Appl. Phys. Lett. 91(7),* pp. 073507. 2007.

[28] C. Sheaff and S. Ashkenazi. A polyimide-etalon thin film structure for all-optical high-frequency ultrasound transduction. *Ultrasonics, Ferroelectrics and Frequency Control, IEEE Transactions On 59(10),* 2012.

[29] M. A. Tadayon, M. Baylor and S. Ashkenazi. High quality factor polymeric fabry-perot resonators utilizing a polymer waveguide. *Optics Express 22(5),* pp. 5904-5912. 2014.

[30] S. G. Ellis, V. Guetta, D. Miller, P. L. Whitlow and E. J. Topol. Relation between lesion characteristics and risk with percutaneous intervention in the stent and glycoprotein IIb/IIIa era: An analysis of results from 10,907 lesions and proposal for new classification scheme. *Circulation 100(19),* pp. 1971-1976. 1999.

[31] K. T. Stroupe, D. A. Morrison, M. A. Hlatky, P. G. Barnett, L. Cao, C. Lyttle, D. M. Hynes, W. G. Henderson and Investigators of Veterans Affairs Cooperative Studies Program #385 (AWESOME: Angina With Extremely Serious Operative Mortality Evaluation). Cost-effectiveness of coronary artery bypass grafts versus percutaneous

coronary intervention for revascularization of high-risk patients. *Circulation 114(12),* pp. 1251-1257. 2006.

[32] S. N. Hoffman, J. A. TenBrook, M. P. Wolf, S. G. Pauker, D. N. Salem and J. B. Wong. A meta-analysis of randomized controlled trials comparing coronary artery bypass graft with percutaneous transluminal coronary angioplasty: One-to eight-year outcomes. *J. Am. Coll. Cardiol. 41(8),* pp. 1293-1304. 2003.

[33] T. Nguyen, A. Colombo, D. Hu, C. L. Grines and S. Saito. *Practical Handbook of Advanced Interventional Cardiology* 2009.

[34] L. V. Wang. Multiscale photoacoustic microscopy and computed tomography. *Nature Photonics 3(9),* pp. 503-509. 2009.

[35] L. V. Wang and H. Wu. *Biomedical Optics: Principles and Imaging* 2012.

[36] H. F. Zhang, K. Maslov, G. Stoica and L. V. Wang. Functional photoacoustic microscopy for high-resolution and noninvasive in vivo imaging. *Nat. Biotechnol. 24(7),* pp. 848-851. 2006.

[37] L. V. Wang. Tutorial on photoacoustic microscopy and computed tomography. *Selected Topics in Quantum Electronics, IEEE Journal Of 14(1),* pp. 171-179. 2008.

[38] Y. Wang, X. Xie, X. Wang, G. Ku, K. L. Gill, D. P. O'Neal, G. Stoica and L. V. Wang. Photoacoustic tomography of a nanoshell contrast agent in the in vivo rat brain. *Nano Letters 4(9),* pp. 1689-1692. 2004.

[39] M. Born and E. Wolf. *Principles of Optics: Electromagnetic Theory of Propagation, Interference and Diffraction of Light* 1999.

[40] C. M. Harris, A. G. Piersol and T. L. Paez. *Harris' Shock and Vibration Handbook* 2002*5*.

[41] E. Ventsel and T. Krauthammer. *Thin Plates and Shells: Theory: Analysis, and Applications* 2001.

[42] H. Lamb. On the vibrations of an elastic plate in contact with water. *Proceedings of the Royal Society of London.Series A 98(690),* pp. 205-216. 1920.

[43] N. McLachlan. The accession to inertia of flexible discs vibrating in a fluid. *Proceedings of the Physical Society 44(5),* pp. 546. 1932.

[44] B. Bilenberg, T. Nielsen, B. Clausen and A. Kristensen. PMMA to SU-8 bonding for polymer based lab-on-a-chip systems with integrated optics. *J Micromech Microengineering 14(6),* pp. 814. 2004.

[45] G. Voskerician, M. S. Shive, R. S. Shawgo, H. v. Recum, J. M. Anderson, M. J. Cima and R. Langer. Biocompatibility and biofouling of MEMS drug delivery devices. *Biomaterials 24(11),* pp. 1959-1967. 2003.

[46] S. Cho, H. M. Lu, L. Cauller, M. I. Romero-Ortega, J. Lee and G. A. Hughes. Biocompatible SU-8-based microprobes for recording neural spike signals from regenerated peripheral nerve fibers. *Sensors Journal, IEEE 8(11),* pp. 1830-1836. 2008.

[47] R. J. Jackman, T. M. Floyd, R. Ghodssi, M. A. Schmidt and K. F. Jensen. Microfluidic systems with on-line UV detection fabricated in photodefinable epoxy. *J Micromech Microengineering 11(3),* pp. 263. 2001.

[48] X. Wang, J. Jin, X. Li, X. Li, Y. Ou, Q. Tang, S. Fu and F. Gao. Low-pressure thermal bonding. *Microelectronic Engineering 88(8),* pp. 2427-2430. 2011.

[49] S. Li, C. B. Freidhoff, R. M. Young and R. Ghodssi. Fabrication of micronozzles using low-temperature wafer-level bonding with SU-8. *J Micromech Microengineering 13(5),* pp. 732. 2003.

[50] A. Yariv and P. Yeh. *Photonics: Optical Electronics in Modern Communications (the Oxford Series in Electrical and Computer Engineering)* 2006.

[51] K. J. Vahala. Optical microcavities. *Nature 424(6950),* pp. 839-846. 2003.

[52] J. Gérard, B. Sermage, B. Gayral, B. Legrand, E. Costard and V. Thierry-Mieg. Enhanced spontaneous emission by quantum boxes in a monolithic optical microcavity. *Phys. Rev. Lett. 81(5),* pp. 1110. 1998.

[53] C. J. Hood, T. W. Lynn, A. C. Doherty, A. S. Parkins and H. J. Kimble. The atom-cavity microscope: Single atoms bound in orbit by single photons. *Science 287(5457),* pp. 1447-1453. 2000.

[54] M. W. Pruessner, T. H. Stievater, J. B. Khurgin and W. S. Rabinovich. Integrated waveguide-DBR microcavity opto-mechanical system. *Optics Express 19(22),* pp. 21904-21918. 2011.

[55] F. Ding, T. Stöferle, L. Mai, A. Knoll and R. F. Mahrt. Vertical microcavities with high Q and strong lateral mode confinement. *Physical Review B 87(16),* pp. 161116. 2013.

[56] P. Rabiei, W. H. Steier, C. Zhang and L. R. Dalton. Polymer micro-ring filters and modulators. *J. Lightwave Technol. 20(11),* pp. 1968. 2002.

[57] B. Little, H. Haus, J. Foresi, L. Kimerling, E. Ippen and D. Ripin. Wavelength switching and routing using absorption and resonance. *Photonics Technology Letters, IEEE 10(6),* pp. 816-818. 1998.

[58] D. Vernooy, V. S. Ilchenko, H. Mabuchi, E. Streed and H. Kimble. High-< i> Q measurements of fused-silica microspheres in the near infrared. *Opt. Lett. 23(4),* pp. 247-249. 1998.

[59] D. Armani, T. Kippenberg, S. Spillane and K. Vahala. Ultra-high-Q toroid microcavity on a chip. *Nature 421(6926),* pp. 925-928. 2003.

[60] K. Srinivasan and O. Painter. Momentum space design of high-Q photonic crystal optical cavities. *Optics Express 10(15),* pp. 670-684. 2002.

[61] M. Notomi, A. Shinya, S. Mitsugi, E. Kuramochi and H. Ryu. Waveguides, resonators and their coupled elements in photonic crystal slabs. *Optics Express 12(8),* pp. 1551-1561. 2004.

[62] B. Crowell. Light and matter. 2003.

[63] A. Yariv and P. Yeh. *Photonics: Optical Electronics in Modern Communications (the Oxford Series in Electrical and Computer Engineering)* 2006.

[64] D. I. Babic and S. W. Corzine. Analytic expressions for the reflection delay, penetration depth, and absorptance of quarter-wave dielectric mirrors. *Quantum Electronics, IEEE Journal Of 28(2),* pp. 514-524. 1992.

[65] N. Hodgson and H. Weber. *Optical Resonators: Fundamentals, Advanced Concepts, Applications* 2005*108*.

[66] M. Baylor, B. W. Cerjan, C. R. Pfiefer, R. W. Boyne, C. L. Couch, N. B. Cramer, C. N. Bowman and R. R. McLeod. Monolithic integration of optical waveguide and fluidic channel structures in a thiol-ene/methacrylate photopolymer. *Optical Materials Express 2(11),* pp. 1548-1555. 2012.

[67] J. R. DeVore. Refractive indices of rutile and sphalerite. *JOSA 41(6),* pp. 416-417. 1951.

[68] I. Malitson. Interspecimen comparison of the refractive index of fused silica. *JOSA 55(10),* pp. 1205-1208. 1965.

[69] C. Sheaff and S. Ashkenazi. Polyimide-etalon all-optical ultrasound transducer for high frequency applications. Presented at SPIE BiOS. 2014, .

[70] G. P. Agrawal. *Fiber-Optic Communication Systems* (Third Edition (Student Edition)) 2002.

[71] Resource2011, "Newport resource e-catalog, pages 1193-1196 (english)," Newport, 2011.

[72] NEP-Menlo-E-SPC-0002, "NEP « noise equivalent power » calculation," Menlo SystemsGmbH, Germany, Tech. Rep. NEP-Menlo-E-SPC-0002, 2010.

[73] 08168-91031, "User's guide HP 8167B/8D/8E/8F tunable laser source," Hewlett Packard, Germany, Tech. Rep. 08168-91031, 1998.

[74] M. A. Tadayon and S. Ashkenazi. Optical micromachined ultrasound transducers (OMUT)--a new approach for high-frequency transducers. *IEEE Trans. Ultrason. Ferroelectr. Freq. Control 60(9),* pp. 2021-2030. 2013.

Appendix A: Matlab code for wall-effect modeling

```
function Ata=propagation(Ata)
global r1 r2 r3 r4 a b lambda % ri:reflectivity of each side. a:cavity
width b:cavity depth

num=find(Ata(1,:)~=0);
% Ata=[A1 A2 A3 A4;                 The amplitude of the propagated
wave
%     theta1 theta2 theta3 theta4;  The incident angle of the wave
%     a1 a2 a3 a4]                  The incident point of the wave
k=2*pi/lambda;

%% beam recieving from side number 1 to other sides and reflecting
if num==1
    if Ata(2,1)~=0
        h1=heaviside(Ata(2,1));
        h2=heaviside(Ata(2,1)-atan((a-Ata(3,1))/b));
        h3=heaviside(-(Ata(2,1)-atan((a-Ata(3,1))/b)));
        h4=heaviside(-Ata(2,1));
        h5=heaviside(Ata(2,1)+atan(Ata(3,1)/b));
        h6=heaviside(-Ata(2,1)-atan(Ata(3,1)/b));

        Ata(2,2)=h1*h2*(pi/2-Ata(2,1));
        Ata(3,2)=h1*h2*Ata(3,1)*cot(Ata(2,1));
        delta2=h1*h2*Ata(3,2)*sec(Ata(2,1))*k;

        Ata(2,3)=(h1*h3+h4*h5)*-Ata(2,1);
        Ata(3,3)=(h1*h3+h4*h5)*(a-Ata(3,1)-b*tan(Ata(2,1)));
        delta3=(h1*h3+h4*h5)*b*sec(Ata(2,1))*k;

        Ata(2,4)=h4*h6*-(pi/2+Ata(2,1));
        Ata(3,4)=h4*h6*(b-Ata(3,1)*cot(-Ata(2,1)));
        delta4=h4*h6*Ata(3,1)*csc(-Ata(2,1))*k;

        Ata(1,2)=h1*h2*Ata(1,1)*r1*exp(-1i*delta2);
        Ata(1,3)=(h1*h3+h4*h5)*Ata(1,1)*r1*exp(-1i*delta3);
        Ata(1,4)=h4*h6*Ata(1,1)*r1*exp(-1i*delta4);
    else
        Ata(2,3)=0;
        Ata(3,3)=a-Ata(3,1);
        delta3=b*k;
        Ata(1,3)=Ata(1,1)*r1*exp(-1i*delta3);
    end
    Ata(:,num)=0;
end
%% beam recieving from side number 2 to the other sides and reflecting
if num==2
    if Ata(2,2)~=0
        h1=heaviside(Ata(2,2));
        h2=heaviside(Ata(2,2)-atan((b-Ata(3,2))/a));
        h3=heaviside(-(Ata(2,2)-atan((b-Ata(3,2))/a)));
        h4=heaviside(-Ata(2,2));
```

```
        h5=heaviside(Ata(2,2)+atan(Ata(3,2)/a));
        h6=heaviside(-Ata(2,2)-atan((Ata(3,2))/a));

        Ata(2,3)=h1*h2*(pi/2-Ata(2,2));
        Ata(3,3)=h1*h2*Ata(3,2)*cot(Ata(2,2));
        delta3=h1*h2*Ata(3,3)*sec(Ata(2,2))*k;

        Ata(2,4)=(h1*h3+h4*h5)*-Ata(2,2);
        Ata(3,4)=(h1*h3+h4*h5)*(b-Ata(3,2)-a*tan(Ata(2,2)));
        delta4=(h1*h3+h4*h5)*sec(Ata(2,2))*a*k;

        Ata(2,1)=h4*h6*-(pi/2+Ata(2,2));
        Ata(3,1)=h4*h6*(a-Ata(3,2)*cot(-Ata(2,2)));
        delta1=h4*h6*Ata(3,2)*csc(-Ata(2,2))*k;

        Ata(1,3)=h1*h2*Ata(1,2)*r2*exp(-1i*delta3);
        Ata(1,4)=(h1*h3+h4*h5)*Ata(1,2)*r2*exp(-1i*delta4);
        Ata(1,1)=h4*h6*Ata(1,2)*r2*exp(-1i*delta1);
    else
        Ata(2,4)=0;
        Ata(3,4)=b-Ata(3,2);
        delta4=a*k;
        Ata(1,3)=Ata(1,2)*r2*exp(-1i*delta4);
    end
    Ata(:,num)=0;
end
%% beam recieving from side number 3 to the other sides and reflecting
if num==3
    if Ata(2,3)~=0
        h1=heaviside(Ata(2,3));
        h2=heaviside(Ata(2,3)-atan((a-Ata(3,3))/b));
        h3=heaviside(-(Ata(2,3)-atan((a-Ata(3,3))/b)));
        h4=heaviside(-Ata(2,3));
        h5=heaviside(Ata(2,3)+atan(Ata(3,3)/b));
        h6=heaviside(-Ata(2,3)-atan(Ata(3,3)/b));

        Ata(2,4)=h1*h2*(pi/2-Ata(2,3));
        Ata(3,4)=h1*h2*Ata(3,3)*cot(Ata(2,3));
        delta4=h1*h2*Ata(3,4)*sec(Ata(2,3))*k;

        Ata(2,1)=(h1*h3+h4*h5)*-Ata(2,3);
        Ata(3,1)=(h1*h3+h4*h5)*(a-Ata(3,3)-b*tan(Ata(2,3)));
        delta1=(h1*h3+h4*h5)*sec(Ata(2,3))*b*k;

        Ata(2,2)=h4*h6*-(pi/2+Ata(2,3));
        Ata(3,2)=h4*h6*(b-Ata(3,3)*cot(-Ata(2,3)));
        delta2=h4*h6*Ata(3,3)*csc(-Ata(2,3))*k;

        Ata(1,4)=h1*h2*Ata(1,3)*r3*exp(-1i*delta4);
        Ata(1,1)=(h1*h3+h4*h5)*Ata(1,3)*r3*exp(-1i*delta1);
```

```
        Ata(1,2)=h4*h6*Ata(1,3)*r3*exp(-1i*delta2);
    else
        Ata(2,1)=0;
        Ata(3,1)=a-Ata(3,3);
        delta1=b*k;
        Ata(1,1)=Ata(1,3)*r3*exp(-1i*delta1);
    end
    Ata(:,num)=0;
end
%% beam recieving from side number 4 to the other side and reflecting
if num==4
    if Ata(2,4)~=0
        h1=heaviside(Ata(2,4));
        h2=heaviside(Ata(2,4)-atan((b-Ata(3,4))/a));
        h3=heaviside(-(Ata(2,4)-atan((b-Ata(3,4))/a)));
        h4=heaviside(-Ata(2,4));
        h5=heaviside(Ata(2,4)+atan(Ata(3,4)/a));
        h6=heaviside(-Ata(2,4)-atan(Ata(3,4)/a));

        Ata(2,1)=h1*h2*(pi/2-Ata(2,4));
        Ata(3,1)=h1*h2*Ata(3,4)*cot(Ata(2,4));
        delta1=h1*h2*Ata(3,1)*sec(Ata(2,4))*k;

        Ata(2,2)=(h1*h3+h4*h5)*-Ata(2,4);
        Ata(3,2)=(h1*h3+h4*h5)*(b-Ata(3,4)-a*cot(Ata(2,4)));
        delta2=(h1*h3+h4*h5)*sec(Ata(2,4))*a*k;

        Ata(2,3)=h4*h6*-(pi/2+Ata(2,4));
        Ata(3,3)=h4*h6*(a-Ata(3,4)*cot(-Ata(2,4)));
        delta3=h4*h6*Ata(3,4)*csc(-Ata(2,4))*k;

        Ata(1,1)=h1*h2*Ata(1,4)*r4*exp(-1i*delta1);
        Ata(1,2)=(h1*h3+h4*h5)*Ata(1,4)*r4*exp(-1i*delta2);
        Ata(1,3)=h4*h6*Ata(1,4)*r4*exp(-1i*delta3);
    else
        Ata(2,2)=0;
        Ata(3,2)=b-Ata(3,4);
        delta2=a*k;
        Ata(1,2)=Ata(1,4)*r4*exp(-1i*delta2);
    end
    Ata(:,num)=0;
end
```

```
%clc
clear all

% close all
global r1 r2 r3 r4 a b lambda % ri:reflectivity of each side. a:cavity
width b:cavity depth. lambda:incident beam wavelength
% Ata=[A1 A2 A3 A4;                 The amplitude of the propagated
wave
%     theta1 theta2 theta3 theta4;  The incident angle of the wave
%     a1 a2 a3 a4]                  The incident point of the wave

r1=.9;r2=.3;r3=.9;r4=.3;

lambda=1500e-9;
a=20e-6;%depth of the cavity
b=20e-6;%depth of the cavity

item=2;% selct which cell we want to run


%% the beam split to multiple photons with different directions
if item==2
    itnum=200;% iteration numbers

    lpvmin=1.5e-6;% minimum loop parameter varaition
    lpvstep=.05e-9;% loop parameter varaition steps
    lpvmax=1.58e-6;% maximum loop parameter varaition
    lpvnum=floor((lpvmax-lpvmin)/lpvstep+1.1);% number of loops

    out=zeros(lpvnum,1);%output beam on the 3rd mirror
    var=zeros(lpvnum,1);%variable (x axis)
    full=zeros(itnum,4);

    ebnummin=1;
    ebnumstep=1;
    ebnummax=299;
    %beampower=zeros(1,ebnummax);
    empoint=linspace(a/ebnummax,a-a/ebnummax,ebnummax);%emission points
    temp=empoint-a/2;
    beampower=exp(-4*temp.^2/a^2);%beam power for different points
    %beamangle=linspace(-lambda/pi/a,+lambda/pi/a,ebnummax);%beam angle
in different points
    beamangle=linspace(-30*pi/180,+30*pi/180,ebnummax);

    %emitted beam number
    lpn=0;%loop number
    h = waitbar(0,'Please wait...');
    for lpv=lpvmin:lpvstep:lpvmax
        lpn=lpn+1;
```

```
        if lpn==1
            waitbar((lpv-lpvmin)/(lpvmax-lpvmin),h,'Please wait...');
            tic
        else
            timing=['Remaining time=',num2str(floor(toc*(1-(lpv-
lpvmin)/(lpvmax-lpvmin))/((lpv-lpvmin)/(lpvmax-lpvmin))/3600)),':',...
                num2str(floor(mod(toc*(1-(lpv-lpvmin)/(lpvmax-
lpvmin))/((lpv-lpvmin)/(lpvmax-lpvmin))/60,60))),':'...
                ,num2str(floor(mod(toc*(1-(lpv-lpvmin)/(lpvmax-
lpvmin))/((lpv-lpvmin)/(lpvmax-lpvmin)/3600),60)))];
            waitbar((lpv-lpvmin)/(lpvmax-lpvmin),h,timing);
        end

        lambda=lpv;%wavelength
        for ebnum =ebnummin:ebnumstep:ebnummax

            full=zeros(itnum,4);%whole of output data
            Ata=zeros(3,4);
            %initiliazation

Ata(:,1)=[beampower(ebnum);beamangle(ebnum);empoint(ebnum)];
            Ata=propagation(Ata);
            num=find(Ata(1,:)~=0);
            Ata(1,num)=1*sqrt(1-
r1^2)*beampower(ebnum)*exp(1i*angle(Ata(1,num)));
            full(1,:)=[Ata(:,num);num];%just for starting the loop with
while it doesn't affect anything
            j=1;

            while j<itnum&&abs(full(j,1))>.001
                j=j+1;
                Ata=propagation(Ata);
                num=find(Ata(1,:)~=0);
                full(j,:)=[Ata(:,num);num];
            end

            if ebnum==1
                var(lpn)=lpv;
            end
            outnum=full(:,4)==3;
            outs=full(outnum,1);
            out(lpn)=(1-r3^2)*sum(outs)*conj(sum(outs))+out(lpn);
        end
    end
    hold on
    plot(var,real(out)/sum(beampower));
    axis tight
    xlabel('\lambda');
    ylabel('Output from one of the mirrors');

    %finding the FWHM and the Finness
```

```
    midval=(max(real(out))+min(real(out)))/2;
    temp=find(real(out)>midval);
    fwhm=var(temp(end))-var(temp(1));
    %moving average to calculate Finness
    filtden = 1;%filter denomenator
    filtnum = 1/3*ones(3,1);%filter numerator
    smout=filter(filtnum,filtden,real(out(temp)));%smoothed output
    didlambda=max(abs(diff(smout))./diff(var(temp)));%didlambda


end
```

Appendix B: Matlab code for waveguide Fabry-Perot resonator

```
R1=.985;R2=.985;

lambda0=1508.544e-9;
lambdaf=1508.544e-9;
lambdastep=.005e-9;

L=25e-6;%cavity length
w0=9.4e-6;%Gaussian Beam size
a=10e-6;% core radius
lmax=3;% maximum number for mode number l
n1=1.6;% core refractive index
n2=1.53;% cladding refractive index
x0=1e-6;% beam misalignment amplitude

Ptotal=1/2*pi*1*w0^2*1;%did not involve /2/376
seg=2000;%number of segment on r axis

Lambda=lambda0:lambdastep:lambdaf;

Xdisp=0e-6:1e-6:10e-6;
PANE=cell(size(Xdisp,2),4);

for j=1:size(Xdisp,2)

    x0=Xdisp(j);

    %[X,Y]=meshgrid(-2*a+x0*heaviside(-
x0):8*a/seg:2*a+x0*heaviside(x0),-1*a:8*a/seg:1*a);
    [X,Y]=meshgrid(-2*a:8*a/seg:2*a,-1*a:8*a/seg:1*a);

[P,Alm,Nlm,Emode]=P_Alm_Nlm_E(R1,R2,L,w0,a,lmax,n1,n2,Lambda,X,Y,x0);


    PANE(j,1)={P};
    PANE(j,2)={Alm};
    PANE(j,3)={Nlm};
    PANE(j,4)={Emode};

    figure(100)
    hold on
    plot(Lambda*1e9,P/9.0436e-11,'.-')

end
```

```
function
[P,Alm,Nlm,Emode]=P_Alm_Nlm_E(R1,R2,L,w0,a,lmax,n1,n2,Lambda,X,Y,x0)

% R1=.985;R2=.985;
%
% lambda0=1508e-9;
% lambdaf=15450e-9;
% lambdastep=.1e-9;
%
% L=25e-6;%cavity length
% w0=9.4e-6;%Gaussian Beam size
% a=10e-6;% core radius
% lmax=3;% maximum number for mode number l
% n1=1.6;% core refractive index
% n2=1.53;% cladding refractive index
% x0=1e-6;% beam misalignment amplitude

% Ptotal=1/2*pi*1*w0^2;
% seg=500;%number of segment on r axis
%
% [X,Y]=meshgrid(-1*a+x0*heaviside(-x0):8*a/seg:1*a+x0*heaviside(x0),-
1*a:8*a/seg:1*a);
% Lambda=lambda0:lambdastep:lambdaf;

Q=2*pi/log(1/(R1*R2));
num=floor(Q)+1;

Z=L*1e-28:2*L:num*2*L;

Ai=1;
A=Ai*sqrt(1-R1)*sqrt(1-R1)*sqrt(R2)*sqrt(R1*R2).^(-1:num-1);
A(1)=Ai*sqrt(R1)*exp(1i*1*pi);


P=zeros(size(Lambda));

Exmode=zeros(size(X));
Eymode=zeros(size(X));
Ezmode=zeros(size(X));

for j=1:size(Lambda,2)
    lambda=Lambda(j);
%
[Beta,H,Q,Al]=EigenModeValues(a,n1,n2,lambda,w0,modenum,X,Y);%[Beta,H,Q
,Al]=EigenModeValues(a,n1,n2,lambda0,w0,modenum,X,Y)
%         if j==1
%
[Alm,Betalm0,Hlm0,Qlm0]=Betalm_Alm(lmax,a,n1,n2,(Lambda(1)+Lambda(end))
```

```
/2,w0,X,Y);%[Alm,Betalm,Hlm,Qlm]=Betalm_Alm(lmax,a,n1,n2,lambda0,w0,X,Y
);
%               kmean=2*pi/((Lambda(1)+Lambda(end))/2);
%               Nlm=Betalm0/kmean;
%               neff=Betalm0(1)/kmean;
%           end

%           k0=2*pi/lambda;
%           Betalm=k0/kmean*Betalm0;
%           Hlm=k0/kmean*Hlm0;
%           Qlm=k0/kmean*Qlm0;

    k0=2*pi/lambda;

[Alm,Betalm,Hlm,Qlm]=Betalm_Alm(lmax,a,n1,n2,Lambda(j),w0,X,Y,x0);%[Alm
,Betalm,Hlm,Qlm]=Betalm_Alm(lmax,a,n1,n2,lambda0,w0,X,Y);
    Nlm=Betalm/k0;
%     if j==1
%         Alm0=Alm;
%     else
%         Alm=Alm0;
%     end

    %Alm(:)=1;
    Ext=zeros(size(X));
    Eyt=zeros(size(X));
    Ezt=zeros(size(X));

    for l=0:lmax
        for m=1:size(Betalm,2)
            if Betalm(l+1,m)~=0&&abs(Alm(l+1,m))>1/num/exp(pi)


[Ex,Ey,Ez]=Efield(a,l,Alm(l+1,m),Betalm(l+1,m),Hlm(l+1,m),Qlm(l+1,m),X,
Y);%calculation of Efield for each mode

                AlZ=sum(exp(-1i*Betalm(l+1,m)*Z).*A);

                if l==0&&m==1
                    figure(500)

temper=sum(sum(((abs(Ex).^2+abs(Ey).^2+abs(Ez).^2)*(X(1,2)-
X(1,1))*(Y(2,1)-Y(1,1)))));
                    plot(Lambda(j),temper,'*')
                    hold on
                end
                Ext=Ext+Ex*AlZ;
                Eyt=Eyt+Ey*AlZ;
                Ezt=Ezt+Ez*AlZ;
                if j==1
```

```
%
Plm=4*sqrt(R1*R2)*sin(4*pi*Nlm(l+1,m)*L./Lambda/2).^2./((1-
sqrt(R1*R2))^2+4*sqrt(R1*R2)*sin(4*pi*Nlm(l+1,m)*L./Lambda/2).^2);
%                       [minval,minnum]=min(Plm);
%                       figure(l*size(Betalm,2)+m)
%                       imagesc(X(1,:)*1e6,Y(:,1)*1e6,real(Ey))
%                       xlabel('X(\mum)','FontSize',18)
%                       ylabel('Y(\mum)','FontSize',18)
%
title(['LP_',num2str(l,'%.0f'),'_',num2str(m,'%.0f'),...
%
'(\lambda=',num2str(Lambda(minnum)*1e9,'%.1f'),'nm',...
%
',A_',num2str(l,'%.0f'),'_',num2str(m,'%.0f'),'=',num2str(Alm(l+1,m),'%
.3f'),')'],'FontSize',18)
%                       set(gca,'FontSize',18)
%                       axis square
                    Exmode=Exmode+Ext;
                    Eymode=Eymode+Eyt;
                    Ezmode=Ezmode+Ezt;
                end
            end
        end
    end

    Pxy=(abs(Ext).^2+abs(Eyt).^2+abs(Ezt).^2)*(X(1,2)-X(1,1))*(Y(2,1)-
Y(1,1));% did not invloved /2/376.6
    P(j)=sum(sum(Pxy));
end
Emode=sqrt(abs(Exmode).^2+abs(Eymode).^2+abs(Ezmode).^2);
```

```
function
[Alm,Betalm,Hlm,Qlm]=Betalm_Alm(lmax,a,n1,n2,lambda0,w0,X,Y,x0)
% lmax=5; %maximum l value
% n1=1.53;%core refractive index
% n2=1.5;%caldding refractive index
% a=15e-6;%radius of core
% lambda0=1550e-9;%wavelength
% w0=9.4e-6; %beam waist
%
% seg=100;%number of segment on r axis
%
% [X,Y]=meshgrid(-2*a:8*a/seg:2*a,-2*a:8*a/seg:2*a);
%r0=0e-6;% misalignment

Phi=atan2(Y,X);
R=sqrt(X.^2+Y.^2)+eps;
E0=exp(-((X-x0).^2+Y.^2)/w0^2);
E0=E0./sqrt(sum(sum(exp(-(X.^2+Y.^2)/w0^2).^2)));

%% finding Betalm

k0=2*pi/lambda0;%wave number

V0=k0*a*sqrt(n1^2-n2^2);
%V=k0*a*sqrt(n1^2-n2^2);%normalized frequency (V number)
[V,Beta]=meshgrid(V0:.05:V0,n2*k0:(n1*k0-n2*k0)/50000:n1*k0);
Beta=flipdim(Beta,1);
H=abs(sqrt(n1^2*k0^2-Beta.^2));

HA=H*a;

criteria=2;
for l=0:lmax

    error=zeros(size(HA));
    temp=zeros(size(HA));

    error(V>HA)=HA(V>HA).*besselj(l+1,HA(V>HA))./besselj(l,HA(V>HA))-
sqrt(V(V>HA).^2-HA(V>HA).^2).*besselk(l+1,sqrt(V(V>HA).^2-
HA(V>HA).^2))./besselk(l,sqrt(V(V>HA).^2-HA(V>HA).^2));
    temp(abs(error)<criteria)=1;
    %imagesc(temp)
    tempnum=find(temp==1);
    tempnum1=[0;tempnum];
    if size(tempnum,1)>1
    tempnum2=tempnum-tempnum1(1:end-1)-1;
    tempnum2(1)=1;
    tempnum3=find(tempnum2~=0);

    if l==0
```

```
        Betalm=zeros(lmax+1,size(tempnum3,1)-1);
    end

    for j=1:size(tempnum3)-1
        betanum=tempnum(floor((tempnum3(j)+tempnum3(j+1))/2)+1);
        Betalm(l+1,j)=Beta(betanum);
    end
    end
end

%% Calculation of Hlm &Qlm

Hlm=sqrt(n1^2*k0^2-Betalm.^2);
Qlm=sqrt(Betalm.^2-n2*k0^2);
Hlm(Betalm==0)=0;
Qlm(Betalm==0)=0;

%% Alm calculation
Alm=zeros(size(Betalm));

for l=0:size(Betalm,1)-1
    for m=1:size(Betalm,2)
        if Betalm(l+1,m)~=0
            h=Hlm(l+1,m);
            q=Qlm(l+1,m);
            Normlm=((besselj(l,h*R).*cos(l*Phi).*(heaviside(R)-
heaviside(R-a))+...

besselj(l,h*a)/besselk(l,q*a)*besselk(l,q*R).*cos(l*Phi).*heaviside(R-
a)));
            Normlm=Normlm./sqrt(sum(sum(Normlm.^2)));
            Alm(l+1,m)=sum(sum((E0.*Normlm)));
        end
    end
end
%Alm=Alm/sqrt(sum(sum(Alm.^2)));
%Alm=Alm/sqrt();
```

```
function [Ex,Ey,Ez]=Efield(a,l,Al,beta,h,q,X,Y)
% a=5e-6;%radius of core
% l=0;%mode number
% h=8.7135e+05;%transverse wavenumber core
% q=8.5700e+05;% transverse wavenumber clad
% beta=6.1406e+06; % wave propagation constant
% Al=1;% amplitude

Phi=atan2(Y,X);
R=sqrt(X.^2+Y.^2)+eps;
Bl=Al*besselj(l,h*a)/besselk(l,q*a);

Excore=zeros(size(R));
Eycore=Al*besselj(l,h*R).*exp(1i*l*Phi);
Ezcore=Al/2*h/beta*(besselj(l+1,h*R).*exp(1i*(l+1)*Phi)+besselj(l-
1,h*R).*exp(1i*(l-1)*Phi));

Exclad=zeros(size(R));
Eyclad=Bl*besselk(l,q*a).*exp(1i*l*Phi);
Ezclad=q/beta*Bl/2*(besselk(l+1,q*R).*exp(1i*(l+1)*Phi)+besselk(l-
1,q*R).*exp(1i*(l-1)*Phi));

Ex=Excore.*(heaviside(R)-heaviside(R-a))+Exclad.*heaviside(R-a);
Ey=Eycore.*(heaviside(R)-heaviside(R-a))+Eyclad.*heaviside(R-a);
Ez=Ezcore.*(heaviside(R)-heaviside(R-a))+Ezclad.*heaviside(R-a);
```